2010

Thermally-induced Motion Of Droplets On A Thin Liquid Layer And Its Application To Droplet Manipulation Platforms

Ehsan Yakhshi-Tafti
University of Central Florida, ehsan.yt@gmail.com

THERMALLY – INDUCED MOTION OF DROPLETS ON A THIN LIQUID LAYER AND ITS APPLICATION TO DROPLET MANIPULATION PLATFORMS

by

EHSAN YAKHSHI-TAFTI
M.S. University of Central Florida, 2009

A thesis submitted in partial fulfillment of the requirements
for the degree of Doctor of Philosophy
in the Department of Mechanical, Materials and Aerospace Engineering
in the College of Engineering and Computer Science
at the University of Central Florida
Orlando, Florida

Fall Term
2010

Major Professors: Ranganathan Kumar and Hyoung Jin Cho

ABSTRACT

In the recent years, there has been a growing interest in droplet-based (digital) microfluidic systems due to their ability to handle multiple discrete samples in a self-contained configuration compared to continuous flow systems. Various methods for droplet manipulation are currently available based on hydrodynamic, electrostatic, chemical, photonic and thermal interactions. High speed, controlled response and minimal thermal loading with least contamination are required in practical applications, especially in chemistry and biology. Although, thermal actuation of droplets has been recognized as an attractive choice due to a wide range of thermomechanical properties that can be exploited, the previous studies yielded limited success in addressing issues such as droplet evaporation, contamination, pinning, hysteresis and irreversibility that are associated with using solid substrate platforms In order to overcome shortcomings of traditional approaches, a novel thermally-actuated droplet manipulation platform based on using an inert liquid film was proposed and its working mechanisms were studied.

Droplets at the air-liquid interface of immiscible liquids usually form partially-submerged lens shapes (e.g. water on oil). In the thermally-induced motion of droplets on the free surface of immiscible liquid films, lens-shaped droplets move from warm toward cooler regions. In addition to this structure, we showed that droplets released from critical heights above the target liquid can sustain the impact

and at the end maintain a spherical ball-shape configuration above the surface, despite undergoing large deformation. It was discovered in this study that such spherical droplets migrate in the opposite direction to lens droplets when subject to a thermal gradient; i.e. direction of increasing temperatures. The existence of this metastable spherical state above the free surface and its transition into more stable lens configuration was investigated using optical diagnostic tools and theoretical analysis.

Opposite direction of motion observed for droplets at the free surface of immiscible liquids was explained based on droplet shape at the interface and the dynamics of thin liquid films subject to lateral thermal gradients: mainly 1) deformation of the free surface and 2) development of an outward moving flow (hot to cold) at the free surface due to surface tension gradients caused by thermal gradients. A lens droplet moves due to the free surface flow caused by Marangoni convection which is from hot to cold. On the other hand, the spherical droplet moves towards the maximum depression on the free surface, occurring at the hottest region as a result of the balance between gravity and drag forces from the opposing free surface flow. The proposed theoretical models predict experimental observations of droplet motion due to thermal gradients satisfactorily.

Opposite responses of thermally-induced motion of lens and spherical droplets on a thin liquid layer, were characterized experimentally and compared to theory by

studying droplet motion in an exponentially-decaying temperature field maintained across the length of a shallow liquid layer. The effect of droplet size and magnitude of thermal gradient (slope) on drop velocity were investigated. The down-scaling effect is prominent, which shows that the proposed concept of droplet manipulation could be used favorably in miniaturized platforms.

Based on the theoretical development and measurements obtained from meso-scale experiments, a silicon-based droplet transportation platform with embedded metal film micro heaters was developed. A thin layer of a chemically-inert and thermally stable liquid was chosen as the carrier liquid. Heaters were interfaced with control electronics and driven through a computer graphical user interface. By creating appropriate spatio-temporal thermal gradient maps, transport of droplets on predetermined pathways was demonstrated with a high level of controllability and speed.

To my spouse *Ghazal* and my little girl *Nili,*

To my mother *Mahnaz* and father *Jafar* and brothers *Mohsen* and *Sina*

To my friend *Omid Amili*

ACKNOWLEDGMENTS

I wish to express my appreciation to my advisers, Professors Ranganathan. Kumar and Hyoung J. Cho for their teaching, advice, financial support and also for the trust and confidence they showed in me. I have learned many lasting lessons beyond the academic life from interacting with them.

I say thanks to the faculty and staff of UCF who were always supportive and helpful throughout my graduate work. Among them, outstanding teachers like Professors Kassab and Kapat for generously giving of their time and expertise to teach me Mathematics, Fluid Mechanics and Heat Transfer and Professor Malocha for teaching me about semiconductor devices and microfabrication. I appreciate the help of Jim Straiter for his assistance in the laboratory. I thank Dr. Sungmin Kim for helping me with electronics and programming. A special note of thanks goes to all the graduate students, postdocs and my lab mates for their friendship and helpful discussions and contributions.

I thank Dr. Hashem Akhavan-Tafti for showing me the importance of self reliance and independent thinking.

TABLE OF CONTENTS

LIST OF FIGURES

LIST OF TABLES

LIST OF MULTIMEDIA

CHAPTER 1: INTRODUCTION

Background

A gradient in surface tension, resulting from non-uniformity in chemical composition, thermal gradients or electrical fields causes an imbalance of tangential stresses at fluidic interfaces resulting in local or bulk flow. A general class of phenomena which are all characterized by the bulk motion under the effect of surface tension gradients are termed as *Marangoni* flows after the observations made by Carlo Marangoni who studied spreading of oil on the surface of water [1].

Wine tears having a back and forth motion on the inner rim of a glass containing wine is a familiar observation, which is caused by surface tension gradients due to varying chemical composition of liquids. Swirling the wine in the glass leaves a thin film on the glass surface. Evaporation of the alcohol content causes the thin film to have higher content of water and hence a higher surface tension compared to that of the bulk mixture at the bottom of the glass. The thin film will roll upward towards higher tension regions and accumulate in form of drops. As drops get larger, gravity would pull them down again (Figure 1). Thermal gradients can cause similar effects by variation of surface/interfacial tension. Vapor bubbles formed on a heating wire immersed in a liquid swim towards hotter regions at the center of the wire before detaching and rising up [2]. Locally heating or cooling a thin sheet of liquid that rests upon a solid surface will cause depression or humps on the surface of the liquid, respectively. The humps and hollows on the thin liquid sheet are due to the higher surface tension of colder liquid which pulls the warmer surrounding fluid with lower surface tension.

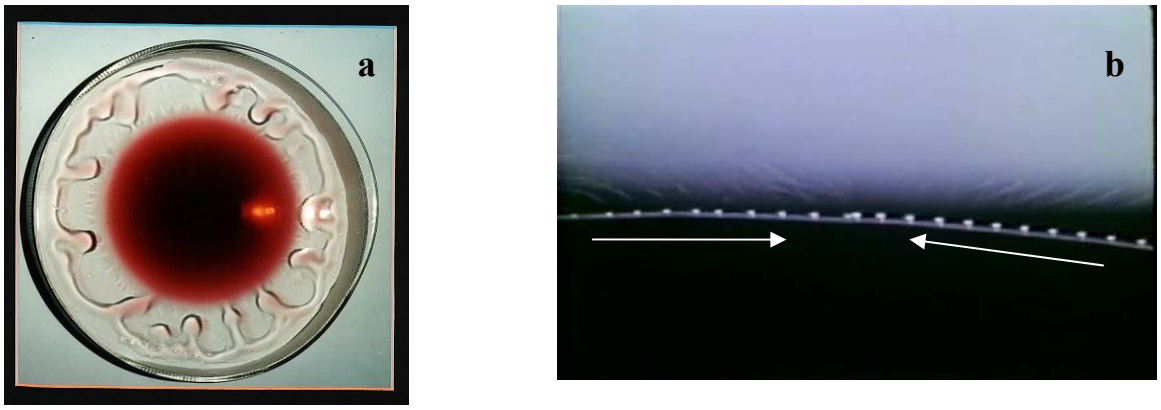

Figure 1 a) Top view of wine glass and wine tears (chemical variation of surface tension)[1] b) Vapor bubbles move toward hotter region in the center of the heater wire (thermal variation of surface tension)[2]

It has been pointed out by Ostrach [3] that there are essentially two basic modes of flow generated by surface-tension gradients. Gradients that are perpendicular to the interfaces cause the so called "Marangoni instability" which leads to cellular flows. Marangoni instability flows have received wide attention and the subject is well established [4]. Surface tension gradients applied parallel to the fluidic interfaces give rise to tangential stresses acting similar to viscous shear stresses and can cause local or bulk flow across the interfaces. Specifically, in multiphase fluid systems, the dispersed (e.g. bubbles and immiscible droplets) and the continuous phases can be set in motion by differentials of various parameters that affect the surface (interfacial) tension of fluids. For example, temperature and chemical gradients alter the cohesion among molecules within the bulk of a fluid as well as the tension at the surface (interface) with other adjacent phases (vapor or other fluid). In majority of fluids, local increases in temperature results in a decrease of the local surface energy (tension), giving rise to a non-uniform tangential stress

[1] Image courtesy of John Bush and Peko Hosoi, MIT

[2] http://web.mit.edu/hml/ncfmf.html

along the surface (interface). Thermally or chemically induced tangential stresses at the interface result in a flow in either of the fluid phases across the interface. In this thesis, motion of droplets on the free surface of a thin liquid (immiscible) film due to lateral thermal gradients has been investigated.

Thermally-induced Motion of Droplets in Interfacial Systems

The literature addressing thermocapillary motion of droplets and bubbles in interfacial systems can be categorized in two major sets: first, droplets (bubbles) dispersed in a second liquid phase and second are droplets on free surfaces which have usually been limited to the study of sessile droplets on chemically or thermally patterned solid surfaces.

Dispersed Droplets

The motion of droplets (liquid in liquid) and bubbles (vapor/gas in liquid) has been studied extensively by means of theoretical and experimental tools. In almost all earth-bound experiments, there exists a density difference between the fluid phases that would cause the droplets (bubbles) to rise due to buoyancy or pulled down because of the gravitation force. It turns out that the buoyancy (gravity) forces are typically larger in magnitude than the thermocapillary forces resulting from thermally induced surface tension gradients; hence the effect of interfacial forces in causing droplet motion can easily be diminished in comparison to the larger forces.

In one of the earliest investigations, Young et al. designed an experiment to determine the relationship between the critical bubble radii and the negative vertical temperature gradient necessary to keep the bubbles motionless with respect to the liquid or make the bubbles to migrate downward, opposite the direction of buoyancy force [5]. The experiment consisted of a

small cylindrical liquid sample held between copper blocks which were fastened between the anvils of a Machinist micrometer. The bottom copper block was heated accordingly, to adjust the vertical temperature gradient (hot to cold from bottom to top) and convection flow was avoided. Bubbles were in the micrometer range and the observed velocities were in the range of μm/sec. The critical temperature gradient required to keep bubbles motionless was found to be proportional to the bubble radius but was not affected by the viscosity of surrounding liquid. In another experiment conducted by Bratukhin et. al, bubbles were release from the bottom of a liquid container subject to a horizontal thermal gradient [6]; one millimeter transverse drift was observed for every 24 millimeters of vertical rise of the bubble from the bottom to top of the test chamber due to a lateral thermal gradient.

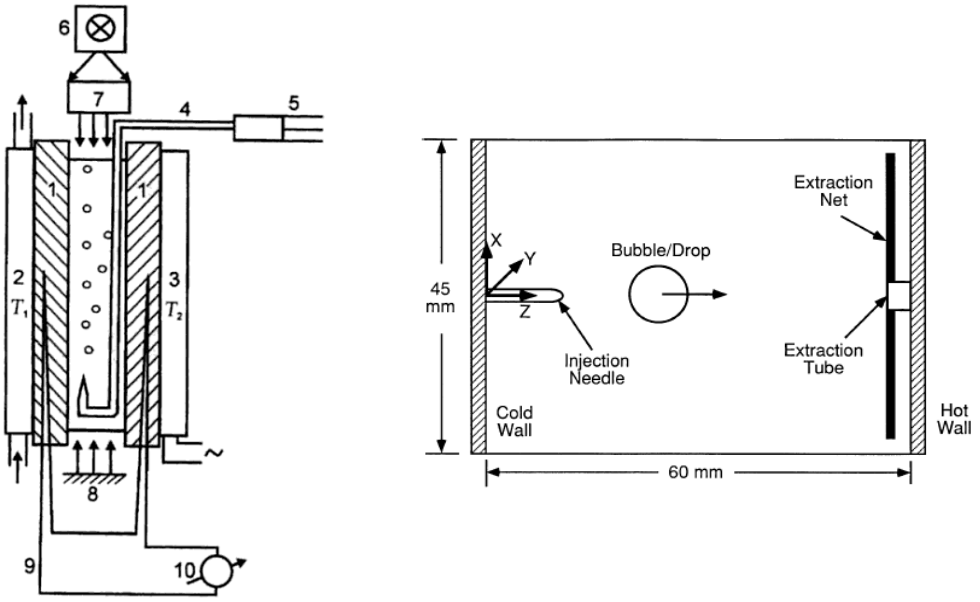

Figure 2 Left) Transverse drift due to thermal gradients in vertically rising bubbles taken from [6] Right) Thermocapillary drift of bubbles/drops in reduced gravity conditions taken from [7]

Buoyant velocity of a bubble is proportional to the square of its radius, whereas the thermocapillary velocity is proportional to the first power of the radius [6]. Therefore, one can eliminate/reduce the effect of gravity/buoyancy by making the dimensions small enough (10 fold reduction in characteristic length of a setup will reduce the effect of gravity 100 times while thermocapillary motive force is lessened by a factor of 10 and the overall ratio of thermocapillary to gravitation forces would increase by a factor of 10). By taking such measures, experiments and theoretical models have been devised in horizontal setups as well, to study thermocapillary drift of bubbles and drops in two-phase systems. A liquid layer (2mm thick, 35x35mm^2 in area), sandwiched between glass plates forms a Hele-Shaw cell. Generating a horizontal temperature gradient across the cell causes bubbles to migrate from colder to warmer regions of the liquid layer [8].

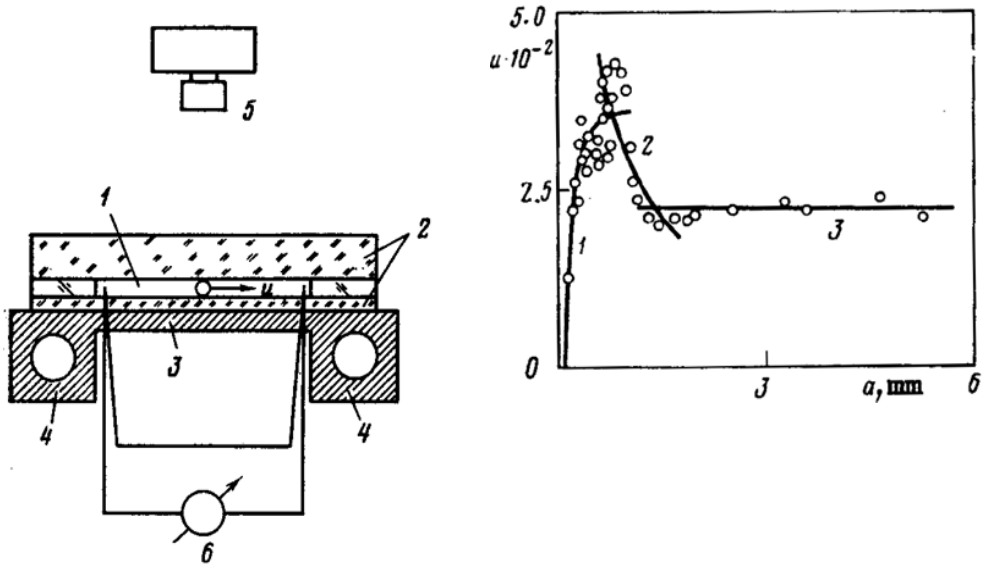

Figure 3 Thermocapillary drift of an air bubble in a horizontal Hele-Shaw cell. Drift velocity is dependent on the bubble radius corresponding to three curves (o: experimental data, solid line: theory) [8]

Some theoretical work has been conducted to construct models for explaining and predicting thermocapillary drift of bubbles and drops in two phase systems. A common assumption made in such studies is that of all fluid properties, only surface tension varies with temperature and that the surface (interfacial tension) is a linear function of temperature (dS/dT = constant < 0). Existing theoretical studies further simplify the solution of the problem by making a pre-assumption that the droplet shape is a sphere which moves in an infinite medium with a fixed velocity. The temperature, pressure and velocity field in the two phases are then found by solving the energy conservation, continuity and momentum equation (Navier Stokes equations) by attaching the reference frame to the center of the moving drop. The surface tension gradient is not treated as a motive term in the equations and the problems are solved assuming that there already exists a bulk flow with a preset velocity in the far field [9].

A general finding in most experimental and theoretical studies is that drops and bubbles migrate toward the hotter regions. However, in this study, droplets were observed to move in either direction of the thermal gradient depending on their shape.

Drops at Free Surfaces

Most studies available on the subject of liquid droplets on free surfaces have been done on solid surfaces. According to Brochard [10], non-uniform spreading coefficient values across a droplet cause motion of the droplet($S = \sigma_s - \sigma_{sl} - \sigma_l$ where σ is surface/interfacial tension and *s*, *sl* and *l* refer to solid, solid-liquid and liquid phases, respectively). The approach to predicting and modeling thermocapillary drift is based on a driving force found by considering the virtual work principle. The drift velocity would then be chosen such that the resulting viscous drag balances

out the driving force and allows for a constant-speed drift. Non-uniformity of spreading coefficients could be due to chemical agents on the solid surface, thermal gradients or electrical charge (potential). Brzoska et al. [11] studied droplet motion on non wettable surfaces (silanized silicon wafers) with horizontal temperature gradients. They found that the droplets only moved if their size was above a certain critical limit and that motion is in the direction of decreasing temperatures; otherwise they would remain pinned to the surface. This critical radius was dependent on the contact angle hysteresis of the surface and was found to be inversely proportional to the imposed temperature gradient. Unlike results of Young and Goldstein [5] where the thermocapilary drift of bubbles were not affected by viscosity, it was observed in this study that the more viscous liquid drops migrated at a relatively lower speed compared to droplets of less viscous liquids. It should be noted that the maximum velocities reported are limited to 2.5 mm/min (~40 μm/sec) due to a temperature gradient equal to 0.56°C/mm.

Recently, there have attempts to take advantage of the thermocapillary drift to manipulate bubbles and droplets for lab on chip applications. Common shortcomings of the proposed methods were low speed (in the range of tens of micrometers per second), relatively high temperatures (70°C), surface contamination, contact angle hysteresis and sample loss in form of evaporation or trailing streaks on the solid substrate. In addition, droplets usually get pinned to the surface, where assist mechanisms are required to jump-start droplets in to motion. Clearly, these conditions are not compatible with biological and fine chemical compounds that are highly sensitive to temperature fluctuations and contaminants. For example, a thermocapillary pumping mechanism has been proposed for pumping nano-liter and pico-liter sized drops in microfabricated flow channels created in glass [12]. One end of a single drop is heated to create a

surface tension difference between the two ends of the droplet. The resulting capillary pressure sets the drop into motion. Contact angle hysteresis was recognized as the major limiting factor which was compensated for, by using tapered channels and external pumping assist mechanisms. Recently, another thermocapillary actuation mechanism was proposed for droplets that were dispensed on chemically patterned surfaces [13]. This microfluidic device was designed for actuation of droplets or continuous streams of fluid on solid surfaces by means of integrated micro-heaters arrays. Results showed that droplets moved away from the heat sources. Using liquo-phobic and liquo-philic chemical surface patterning, droplet motion was limited to predefined paths under the influence of thermal gradients (Figure 4).

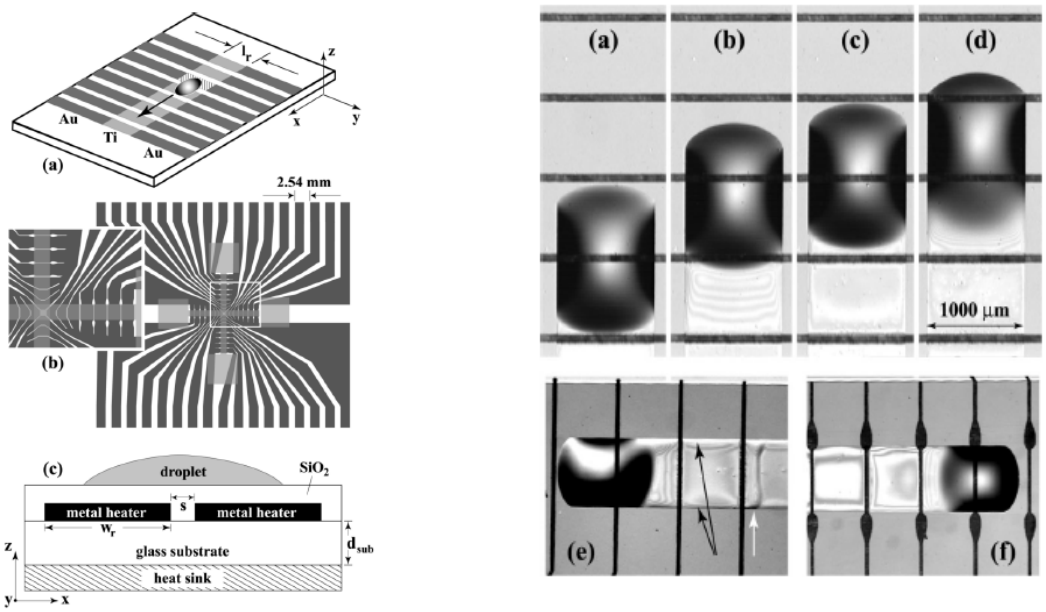

Figure 4 Left) The array of micro-heater under liquo-philic stripes are used to move liquid droplets via thermal gradients while keeping droplets on predefined pathways Right) Snapshots of the motion of a PDMS droplet at 44 seconds time interval taken from [13]

As mentioned earlier, theoretical and experimental studies available for droplet motion at free surfaces are mostly focused on sessile droplets on solid surfaces. A common result found in the

reviewed publications is that droplets dispensed on solid surfaces migrate toward colder regions of the thermal gradient.

Problem Statement - Thesis Outline

In this thesis, we deal with the thermally-induced motion of droplets (water) at the air-liquid interface of a thin liquid layer (Perfluorotributylamine, FC43). This problem is of importance both from a fundamental science point of view as well as from an applied perspective. Droplet manipulation using thermal gradients has been mostly studied and reported for chemically patterned solid substrates; in this study drop motion is investigated on liquid buffer layers where we find that the direction of motion is dependent on the droplet configuration at the interface (lens vs. sphere). Motion of normally occurring lens droplets on liquid surfaces was recently studied[14-16]; however the dependency of the direction of thermal motion on droplet shape at the free surface has not been observed or described in the past[17]. We observed that lens drops move in the direction of decreasing temperatures, consistent with the observations reported in existing studies. However, we discovered that droplets released from a critical height above the target liquid can sustain the impact and maintain a spherical ball shape above the surface. We observed that such spherical droplets move in the opposite direction of lens droplets; i.e. towards increasing temperatures.

The observations for droplet motion on free liquid interfaces are mainly explained based on the physics of thin liquid layers subject to lateral thermal gradients and the shape of droplets at the air liquid interface. Droplets can acquire a lens shape or a spherical configuration at the air-liquid interface. The requirements for droplets impacting on target liquid surfaces to maintain a spherical shape are found by experiment and investigated theoretically in chapter 2. The effect of

temperature gradients on interfacial tensions has been demonstrated in an experimental setup designed for measuring the temperature dependency of surface (interfacial) tension among various fluid pairs. In chapter 3, the theoretical framework for the dynamics of thin liquid films under the influence of an imposed thermal gradient has been developed, which together with the details of droplet shape at the interface is used to explain the opposite direction of motion observed for interfacial droplets. Experimental results of uni-direcitonal thermally-actuated motion of lens and spherical droplets on the surface of fluorocarbon liquid have been provided in chapter 4 where the effect of droplet size and magnitude of temperature gradient on the drift velocity has been investigated. In chapter 5, experimental results are compared to the theoretical models.

The last portion of the thesis is concerned with the design, fabrication and testing of a droplet manipulation platform based on the physical understanding of this phenomena. With the recent advent of novel Microsystems (microfluidics) and Lab on Chip applications, droplet-based systems have received widespread attention. Droplets offer a self-contained and contamination-free microreactor environment, which also serve as vehicles for material transport. Large surface to volume ratio in droplets offers superior control over process parameters such as temperature within the droplet. One of the major challenges however, is the transportation and manipulation of droplets in a robust and predictable manner. A prototype of a droplet manipulation platform is presented in chapter 6. In this method, droplets are dispensed on the free surface of a two dimensional liquid pool that is formed on a silicon wafer with embedded microheaters. Microheater elements generate the desired thermal maps necessary for droplet motion on a preset pathway. Experiments show that switching to a liquid platform yields significant increase in

migration speed and also eliminates the need for the direct application of heat to the droplet which may be carrying temperature-sensitive materials.

In this study, high speed droplet transport has been achieved by replacing the solid substrate with a chemically-inert and thermally-stable liquid film. Spherical drops offer superior control on droplet location and motion. Lens droplets can take on any arbitrary path away from a hot spot, while spherical droplets always get pulled to known locations (hot spots). Through a computer interface, the user can control the droplet position and transport it on the platform using spatio-temporal thermal gradient maps.

CHAPTER 2: DROPLETS AT INTERFACES

Introduction

The study of droplet impingement on solid and liquid surfaces is of importance in the fundamental understanding of the underlying physics and the applied aspects of the subject for example spray cooling [18, 19], inkjet printing [20], soil erosion due to rain [21] and understanding and quantifying rainfall [22]. Phenomena that occur following the impact of droplets on solid and liquid surfaces are fascinating observations; yet their physical and mathematical description often lead to complex formulations [22-26]. A thorough review on the topic has been carried out by Rein [27] and Yarin [28].

Droplets impinging on the surface of a liquid can splash [23, 29], coalesce with or bounce off the target surface [27] depending on various factors including impact velocity of the droplet, the depth of the target liquid and the physical properties of the fluids. Typically, when a droplet collides with the liquid surface at a relatively high speed, a crater is formed. Due to instability of the rising liquid sheet on the rim, smaller jets are ejected and the resulting structure resembles a crown; these jets further breakup into spray droplets. As the walls of the crater rim subside, the receding flow towards the center shoots up in form of a column of fluid which also breaks up and secondary droplets are ejected in the vertical direction [22, 24, 28]. In addition to the impact velocity, experimental results show the dependency of splashing, deposition and crown formation of impinging droplets on liquid films on the fluids' viscosity and film thickness [30, 31]. It has been found that in the limit of extremely thin target films, the critical splashing following impact of droplets is insensitive to the film thickness for given underlying solid surfaces [32].

Generally, droplets impinging on the surface of self similar liquids eventually coalesce with the target pool, or form a lens-shaped structure on the free surface if liquids are immiscible. However, spherical ball-shaped droplets have also been observed that exist at the air-liquid interface. Such isolated droplets on the surface of similar liquids have been attributed mainly to the existence of a cushion of trapped air which serves as a lubricating film, preventing it from coalescing with the bulk liquid [33, 34]. The non-coalescence effect requires continuous drainage of the air cushion; for example when the target liquid pool is set to vibrate in the normal direction [35, 36]. A similar bouncing/anti wetting effect is observed for droplets impinging upon superhydrophobic solid substrates [37].

In this study, it is shown that droplets impinging upon the surface of an immiscible liquid can retain a metastable spherical configuration above the surface following the impact, without collapsing into the target liquid to form partially submerged lenses that are commonly observed for droplets resting at the air-liquid interface of immiscible liquids. We found that under certain conditions, the spherical droplets can retain their shape for relatively long periods (without external stimuli) unless the system is disturbed causing them to collapse into the stable lens structures.

Droplet Impact

A set of precision dispensing needles with various tip diameter sizes were used to release pendant droplets of deionized water on the surface of FC-43. Droplet impact was recorded by a high speed camera at a rate of 2000 frames per second.

Figure 5 (Droplet Impact Video) shows the time progression of the droplet impact and one cycle of oscillation of the droplet on the surface. It is seen that both the target liquid and the droplet undergo large deformations during the impact; however, the droplet is able to maintain its spheroid structural integrity after the impact. The deformations are similar to the morphologies reported for droplets impacting upon soft solids [38] but they are not large enough to result in the splitting of the original droplet. The amplitude of deformation dies out quickly within the first few oscillation cycles to viscous effects.

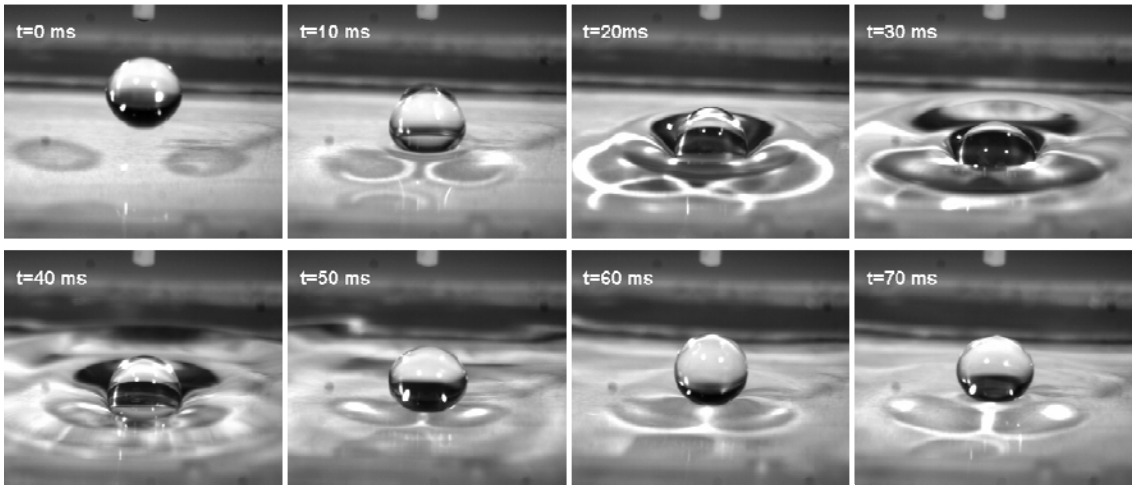

Figure 5 Impact and oscillation of a drop of water on the surface of fluorocarbon liquid FC-43

In another experiment, the imaging was done from the liquid side below the free surface (Figure 6). It is seen that the maximum penetration of the drop is almost two times the static deflection. In order for pendant water droplets to sustain the impact and retain a spherical configuration at the air-liquid interface of the target liquid pool, it is required that they be of a critical size and be released from a certain height range. Figure 7 provides the range of the critical release heights for which various size droplets are able to sustain the impact and retain a spherical shape while the underlying liquid sheet stretches to accommodate the impact.

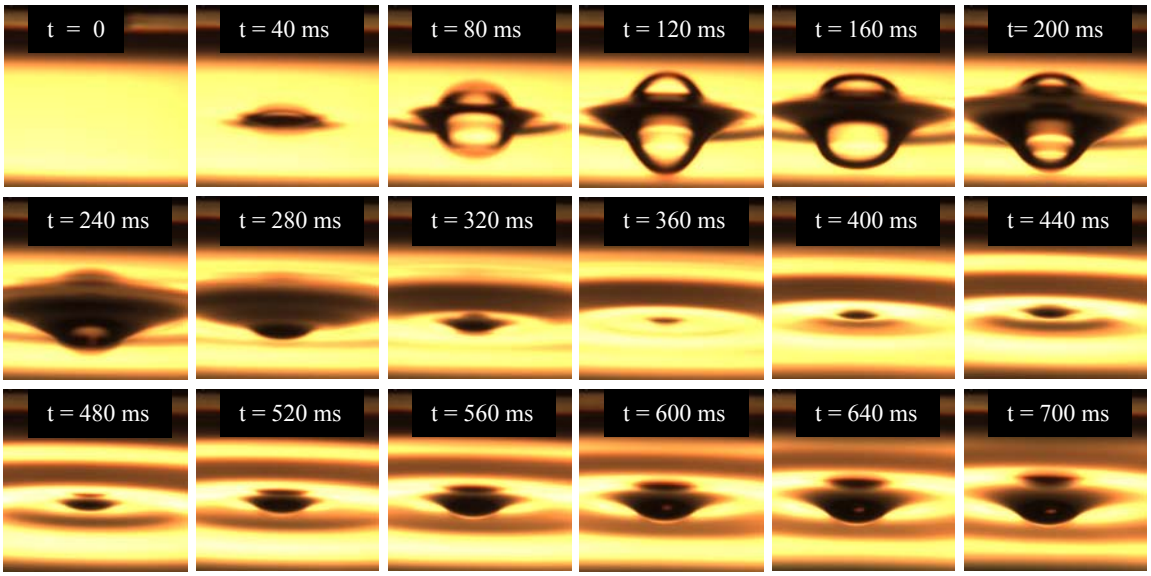

Figure 6 Sequence of drop impact; free surface has been illuminated and imaged from below (liquid side)

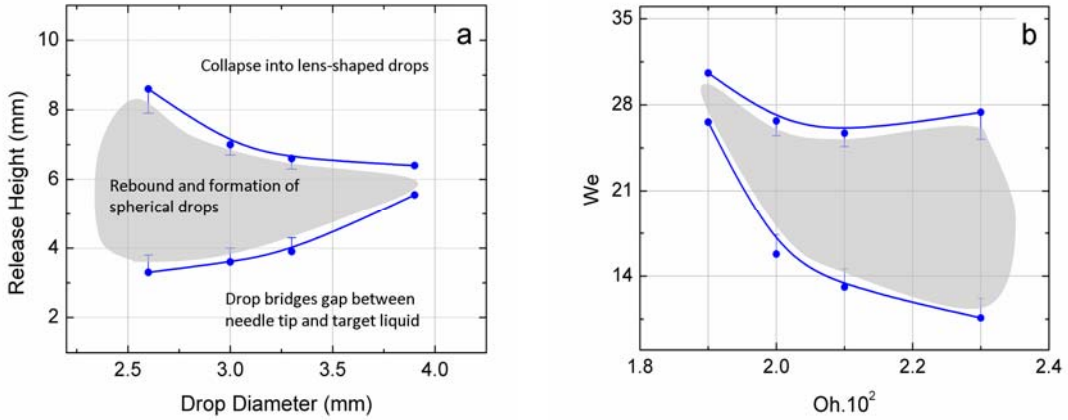

Figure 7 Characterization map for drop impact as function of release height and drop diameter; b) Representation of the characterization map in terms of non dimensional parameters (We, Oh). In the gray region, drops sustain the impact and assume a spherical ball shape above the surface of the target liquid; in the region above the upper bound of the gray area, impacting drops collapse into lens-shaped drops; whereas below the lower bound, free-falling pendant drops cannot be formed since drops bridge the gap between the dispensing tip and the liquid interface.

The gray area on the graph represents a collection of release-heights for which droplets rebound on the surface and form a spherical structure above the interface. Similar spherical droplets on liquid surfaces have been shown by isolating the two fluids for example by coating the exterior of the droplets by super-hydrophobic powders [39]. The critical release height for droplets released from a 27G (resulting droplet diameter is 2.6 mm) needle ranges from about 1.5 to 3 times the drop diameter and gets narrower for smaller gauged needles (larger drops). A cubic relationship was found between the diameter of the needle tip and the pendant drops that pinched off the tip due to their own weight.

Weber number ($We = \rho U^2 D / \sigma$), Ohnesorge number ($Oh = \mu / \sqrt{\rho \sigma D}$), normalized film thickness (th*=th/D) and the Bond number ($Bo = \rho g h^2 / \sigma$) are commonly used in analysis of such systems (σ is the target liquid's surface tension with air, ρ, the density of the drop, D is the drop diameter and U is the impact speed which is a function of release height given as $U = \sqrt{2gH}$). The Ohnesorge number relates the viscous forces to inertial and surface tension forces, Weber number is used for evaluating the relative importance of inertia and surface tension and the Bond number compares the gravitational force to surface tension effects. Using the physical properties of water and FC-43, the conditions of the experiment are characterized by $Oh \approx 0.02$, $We \approx 20$ ($Bo \approx 10$) for th*≈ 4. It is seen that for larger droplets, the critical height range for successful rebound is narrower. Larger droplets and those released from higher than critical heights were found to collapse immediately into a lens-shaped structure in the process of impact as commonly observed. The lower bound of release heights in experiments resulted from the minimum distance between the needle tip and the interface such that pendant droplets could

be formed; for shorter distances droplets formed a bridge between the tip and the target liquid and could not get released into a free fall.

The spherical droplets can remain intact on the surface; however, they are usually short lived and unstable; they have a tendency to collapse into the submerged configuration if there are any perturbations or vibrations. Figure 8 (Droplet Breakup Video) shows the breakup and transformation of a spherical droplet into a lens structure at the air-liquid interface in slow motion; a process which completes in less than a tenth of a second. It is seen that the droplet undergoes rapid and asymmetric deformations from the bottom and the sides until it eventually settles into a symmetric shape in form of a partially submerged lens. Static conditions for the droplet can be determined by carrying out a force balance or by evaluating the total energy of the system.

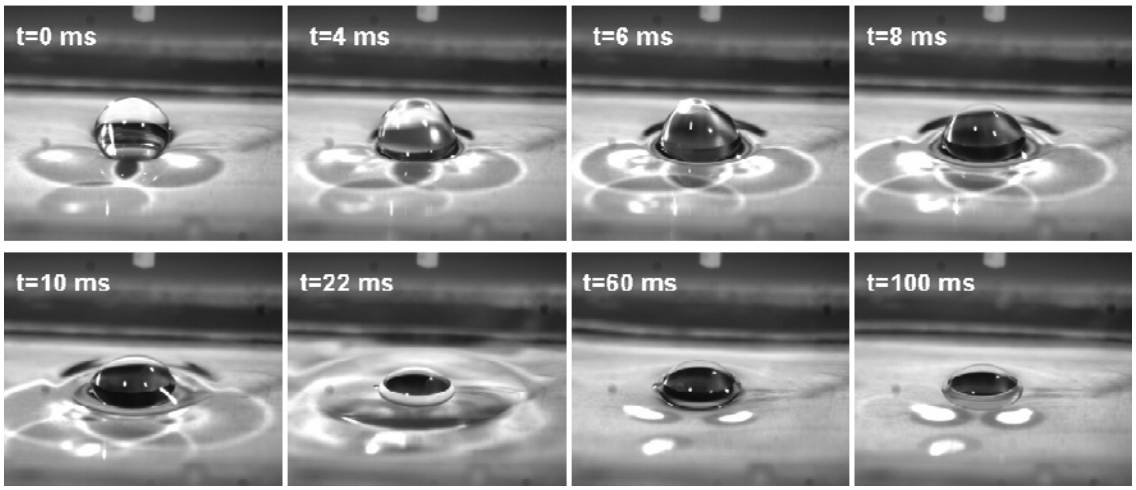

Figure 8 Collapse of a spherical drop into partially-submerged lens configuration

Equilibrium Static Configuration of a Droplet at an Air-Liquid Interface

A balance of forces in the vertical direction can be used to find the equilibrium static states of a droplet resting at the air-liquid interface. Similarly, extrema of the system's energy (surface energy and work of the external forces acting on the system) can also provide equilibrium states (droplet configuration at the interface) that determine the stability of a given static configuration [40]. Considering Figure 9, there are three forces that act on the drop in the vertical direction [41]:

Gravity force (drop weight):

$$F_G = \tfrac{4}{3}\pi g \rho_w r^3 \tag{1}$$

Surface tension force exerted on the drop by the target liquid:

$$F_S = 2\pi\sigma_f r \sin(\varphi)\sin(\varphi+\theta) \tag{2}$$

and finally the *Buoyancy* force which is found by integrating the vertical component of the hydrostatic pressure around the surface of the drop:

$$F_B = \pi g \rho_f \left[h_0 r^2 \sin^2(\varphi) + r^3 \sin^2(\varphi)\cos(\varphi) + \tfrac{2}{3} r^3 (\cos^3(\varphi) - 1) \right] \tag{3}$$

The net force is the algebraic sum of three forces.

In these expressions, *r* is the equivalent radius of a sphere that has a volume equal to the drop, ρ_f = 1880kg/m^3, ρ_w = 998kg/m^3 are the density of the base liquid and the water droplet and the density of the surrounding air is neglected. σ_f=16 dyne/cm, σ_w=71dyne/cm and σ_{fw}=52dyne/cm are the surface (interfacial) tensions of the target liquid (FC-43) – air, drop (water) – air and drop – target liquid pairs respectively, measured by the pendant drop method implemented in this study.

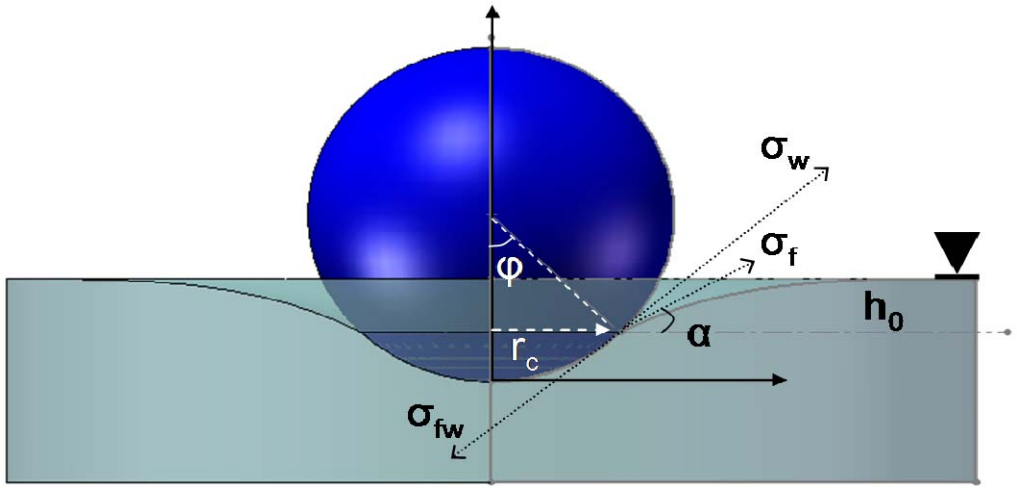

Figure 9 Schematic of a spherical drop resting at the liquid-air interface

The angle φ represents the extent of submergence of the droplet in the target liquid; by varying φ from 0 (droplet above the surface and touching) to 180º (fully submerged), the normalized net force f_{NET} (normalized by $r\sigma_f$) acting on the droplet can be plotted as a function of φ using the equilibrium contact angle as a parameter.

$$f_{NET} = \frac{F_{NET}}{r\sigma_f} = \frac{4}{3}\pi\left(\frac{g\rho_f}{\sigma_f}r^2\right)\left(\frac{\rho_w}{\rho_f}\right) + 2\pi\sin\varphi\cos\varphi + 2\pi\left(\frac{h_0}{r}\right)\left(\frac{g\rho_f}{\sigma_f}r^2\right)\sin^2\varphi + ...$$

$$...\pi\left(\frac{g\rho_f}{\sigma_f}r^2\right)\left[\sin^2\varphi\cos\varphi + \frac{2}{3}\left(\cos^3\varphi - 1\right)\right]$$

(4)

$C_1 = \frac{g\rho_f}{\sigma_f}$ and $C_2 = \frac{\rho_w}{\rho_f}$ are constants based on the droplet size and physical properties of fluids; for water droplets at the air-interface of a fluorocarbon liquid pool: $C_1 = 1.152\frac{1}{mm^2}$ and C_2=*0.53*. Considering equation 4, submergence angles, which correspond to $f_{NET} = 0$ would be the equilibrium static conditions for droplets resting at the interface.

It is noted that in order to evaluate the buoyancy force term (equation 3), the capillary rise (fall) of the target liquid on the drop, h_0, is needed (h_0, is measured from the free surface to three phase contact line, $h_0 = z_{x=r_c} - z_{x\to\infty}$). For the case of spherical drops, h_0 is not readily available [42] and is found by numerically solving the Young-Laplace equation governing the free surface profile in the vicinity of the drop-liquid-air contact line:

$$\left[\frac{d^2z/dr^2}{\left[1+(dz/dr)^2\right]^{3/2}} + \frac{dz/dr}{r\left[1+(dz/dr)^2\right]^{1/2}}\right] - \frac{\rho_f g z}{\sigma_f} = 0$$

(5)

The governing equation for the capillary profile is normalized by letting $z^* = C_1^{1/2} z$ and $x^* = C_1^{1/2} r$:

$$\left[\frac{d^2 z^* / dx^{*2}}{\left[1 + (dz^* / dx^*)^2\right]^{3/2}} + \frac{dz^* / dx^*}{x^* \left[1 + (dz^* / dx^*)^2\right]^{1/2}} \right] - z^* = 0 \qquad \textbf{(6)}$$

Equation 6 was numerically solved with boundary conditions as: $dz/dr = dz^*/dx^* = \tan(\alpha)$ at $r=r_c$ (r_c is contact line radius) and $dz^*/dx^* = 0$ as $x^* \to \infty$ (∞ found to be around 3 times the drop diameter by extending the solution for larger x). $\alpha = \theta + \varphi - \pi$, and θ is the equilibrium contact angle measured counterclock wise from σ_{fw} to σ_f.

In Figure 10, the balance of forces resulting from equation 4 and numerical solution of the meniscus profile (equation 6) for an interfacial drop *(R=1.25mm)* using corresponding values of C_1 and C_2 of water and FC43. Equilibrium contact angle θ_e.is chosen as a variable.

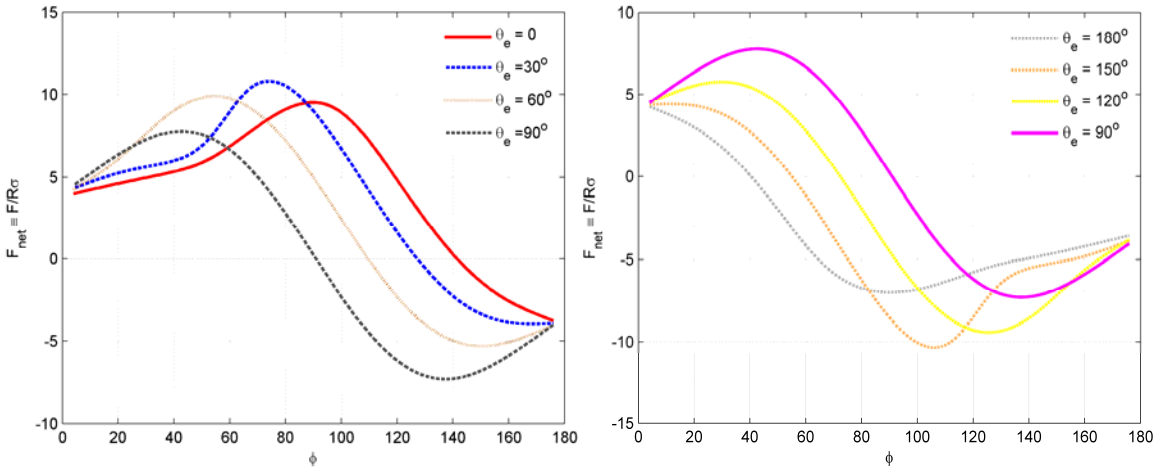

Figure 10 Equilibrium balance of forces (normalized by $R\sigma_f \approx 20\mu N$) is plotted as a function of the level of immersion of the drop in the underlying liquid pool.

Based on experiments, the equilibrium contact angle at the triple contact line was found to be $\theta_e=15^o\pm3^o$ (error is due to the misalignment of the imaging camera with the horizontal line). Solving equation 4 for a water droplet with *r=1.25mm*, the normalized net vertical force becomes zero at $\varphi \approx 135^o$ (Figure 11a) which shows that the partially submerged lens configuration is the only static equilibrium condition. This calculated angle is in good agreement with the observed extent of immersion of the droplet in the lens configuration ($\varphi_s=140^o$) (Figure 12b). Figure 11b shows the capillary rise and the meniscus profile of the free liquid surface.

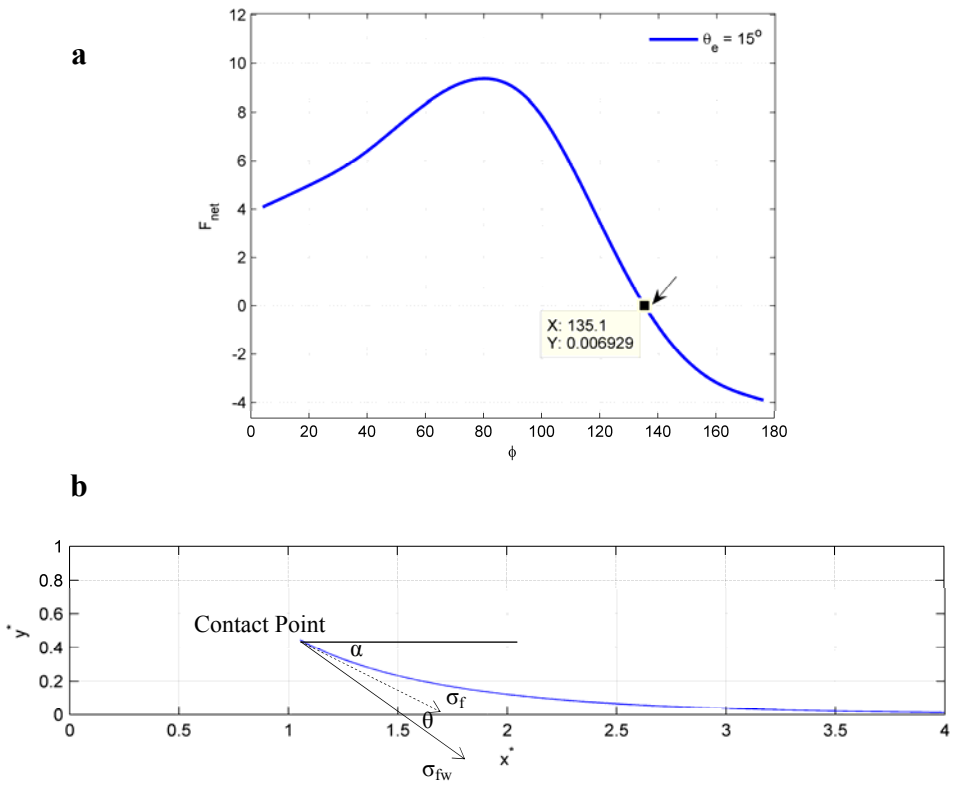

Figure 11 a) Net vertical force as a function of the extent of drop submergence in the target liquid (θ_e=15˚); b) Free surface profile of the liquid film in vicinity of the contact line C, (angle between the horizon and the free surface tension σ_f, $\alpha \approx -30^{\circ}$, equilibrium contact angle θ_e =15˚)

It is noted that the force analysis is performed by approximating the droplet as a perfect spherical volume, while this not exactly true for lens shaped drops at the interface. The exact shape of a droplet residing at the interface of two fluids has been described in detail [14].

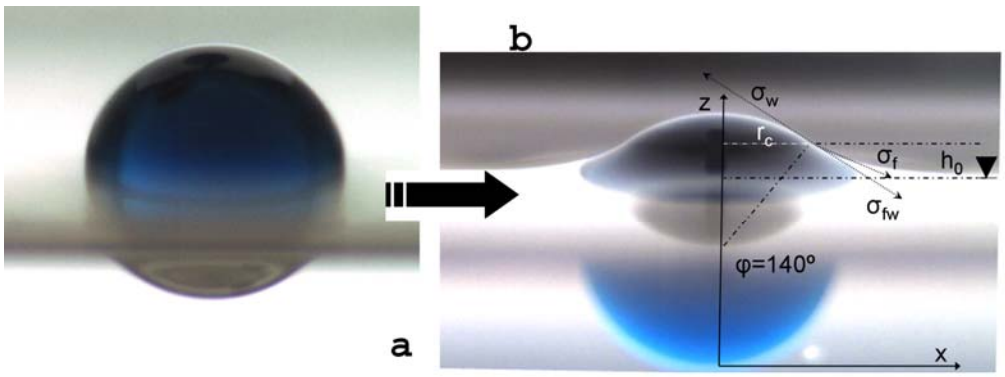

Figure 12 Spherical drop (a) converts into the stable partially submerged lens shape configuration (b)

While we observe two distinct static configurations for the droplets at the interface, only the lens configuration is predicted by the force balance model (f_{NET} plotted against φ has a single zero, Figure 11a). The net force (sinking) has a negative slope when passing the equilibrium, which physically translates to the following: the sinking force decreases (changes signs and becomes upward) if the droplet were to be further immersed in the base liquid and since the droplet would not accelerate against the direction of gravity, it has to eventually rest at this state. The force balance provides only the *equilibrium* static states because the thermodynamic equilibrium contact angle θ_e is used; in addition it is assumed that the Young Laplace equation is satisfied at the drop – liquid interface profile. Static conditions other than the equilibrium, for example the spherical configuration observed here, are known as *mechanically enforced stationary* states [40, 43] that are achieved with the aid of some external agents present in the system that compensate for the imbalanced *equilibrium* forces. The spherical droplet in our case is predicted not to be at static equilibrium due (nonzero equilibrium force balance); however it does exist in a static state in our experiments. Existence of a fine interfacial air film has been confirmed for non-coalescent drops impinging on the surface of self-similar liquid films [33, 34].

It is likely that an extremely thin cushion of air balances the net vertical force and allows the existence of the isolated spherical drop on the free surface. The lower bound of the thickness of such an air film has been estimated to be on the order of *10nm* (Van der Waals attraction) and upper bound of *1 - 10μm* considering the continuously-drained air film due to relative motion of the fluid interfaces which is explained in subsequent sections. Based on calculations carried out in the work, the air gap was found to have a thickness of around 7μm.

Effect of Temperature on Fluid Interfaces

In order to describe and formulate the problem of thermally induced motion of water droplets on the surface of FC43, interfacial tension among all fluid pairs (water – air, FC43 – air and water – FC43) is needed. In addition, temperature dependency of the tension values is required. For most fluids, surface tension decreases with increase of temperature. Surface tension is defined as the energy per unit area of the *surface* of a liquid with its vapor (gas). At the critical temperature the surface tension approaches zero since there is no distinction between the liquid and gaseous phases and a definite interface cannot be defined among the two phases. A comprehensive theory capable of predicting surface tension and its dependency on temperature does not exist and semi empirical methods are used [44].

An in-house experimental setup based on the *pendant drop method* was developed to measure surface (interfacial tension). A pendant drop is formed in air or within the other immiscible medium. The profile of the droplet is captured by imaging the droplet and using backlighting. Based on the *Young-Laplace* equations, the shape of a pendant droplet can be found theoretically. By comparing the actual droplet curvature and the theoretically-predicted shape, the appropriate value for surface (interface) tension can be determined.

Bashforth and Adams first developed the drop-shape method by numerically solving the theoretical equations describing the shape of a static droplet in a gravitation field [45]. The equations are derived in the following manner. Consider R_1 and R_2 to be the principal radii of curvature at point P on the surface (Figure 13).

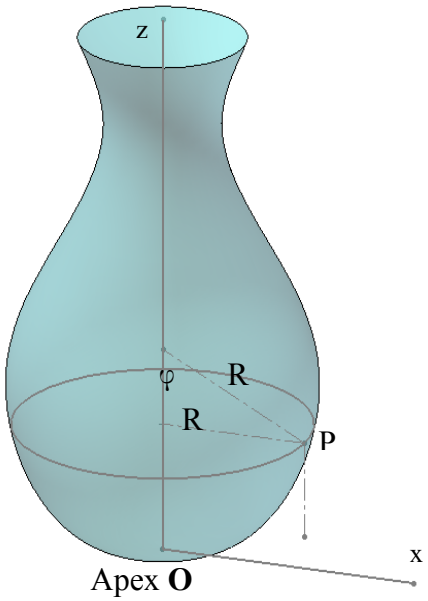

Figure 13 Drop shape, R_1 (vertical plane, xz) and R_2 (horizontal plane) are the principal radii of curvature at P on the surface. φ is the angle radius R_1 makes with the z

Hydrostatic pressure, $P = \rho g z + C$, were ρ and g are the density and the gravitational constant and C is a constant dependent upon where the reference is chosen. The pressure difference across a curved interface is governed by the *Young-Laplace* relationship.

$$\frac{1}{R_1} + \frac{1}{R_2} = \frac{\Delta P}{\sigma} = \frac{\Delta \rho g z + C}{\sigma} \qquad \textbf{(7)}$$

At the droplet apex *(z=0), R_1=R_2=b* therefore $C = 2\sigma/b$ and since $R_2 = x/\sin\varphi$:

$$\frac{1}{R_1} + \frac{\sin\varphi}{x} = \frac{\Delta\rho g z}{\sigma} + \frac{2}{b}$$

(8)

Using $x^* = x/b$, $z^* = z/b$, $R_1^* = R_1/b$ and grouping physical properties and constants in the gravitational parameter, $\beta \equiv \frac{\Delta\rho g b^2}{\sigma}$ the dimensionless differential equation is found as follows

$$\frac{1}{R^*_1} + \frac{\sin\varphi}{x^*} = \beta z^* + 2$$

(9)

R_1 and *sinφ* can be replaced in the following manner to achieve a differential equation that describes the curve in the form *z=f(x)*.

$$\frac{1}{R_1} = \frac{d^2z/dx^2}{\left[1+\left(\frac{dz}{dx}\right)^2\right]^{3/2}}$$

$$\sin\varphi = \frac{dz/dx}{\left[1+\left(\frac{dz}{dx}\right)^2\right]^{1/2}}$$

$$\frac{d^2z}{dx^2}+\left[1+\left(\frac{dz}{dx}\right)^2\right]\frac{1}{x}\frac{dz}{dx}=(2+\beta z)\left[1+\left(\frac{dz}{dx}\right)^2\right]^{3/2}$$

(10)

It is noted that the form of the curve (droplet shape) only depends on the magnitude of the gravitational parameter β (superscript * has been dropped). First boundary condition is: $x=0:z=0$. The other boundary condition is not apparent and results from examining equation 9 at the apex of the drop *($z^*=0$, $x^*=0$)*, $R^*_1=1$ ($R_1=b$), therefore the term, $\lim\left(\frac{\sin\varphi}{x^*}\right)_{x^*\to 0}=1$. This formulation is not suitable for solving the second order differential equation using a numerical solver. Another approach is to form a set of first order differential equations (for *x, z* and *φ*) as function of the curve length, *s*, starting from the apex (origin). In this way boundary conditions can be set explicitly.

From the definition of *sinφ* it can be seen that $\frac{1}{R_1}=\frac{d}{dx}(\sin\varphi)=\frac{d\varphi}{ds}$ since the differential curve length is written as: $ds=R_1 d\varphi$; similarly $\frac{dx}{ds}=\cos\varphi$ and $\frac{dz}{ds}=\sin\varphi$.

Considering equation 9, and the auxiliary equations for the coordinates, the set of first order differential equations that are solved simultaneously to give the drop shape is as follows:

$$\frac{d\alpha}{ds} = 2 - \beta z - \frac{\sin\varphi}{x}$$
$$\frac{dx}{ds} = \cos\varphi$$
$$\frac{dz}{ds} = \sin\varphi$$
$$s = 0 : x = 0, z = 0, \varphi = 0$$

(11)

Fourth order Runge Kutta solver is used to solve the set of differential equations.

The experimental setup shown in (Figure 14) is used to take images of pendant drops of each liquid formed in air (vapor) and other immiscible liquids.

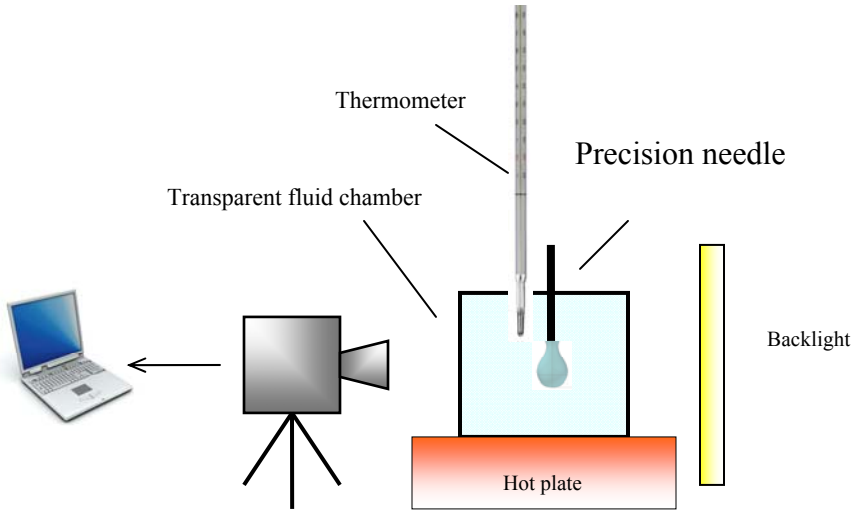

Figure 14 Experimental setup; images of pendant drops formed in a fluidic chamber are transferred to a processing unit

A computer code was written that could read the image files and find the boundaries; the drop was then rescaled for plotting. By considering a least square method, surface tension that is

incorporated in the β parameter is found, such that the closest overlap of the two profiles is achieved. Consistency, accuracy and reproducibility of results based on this method was verified by comparing the measurements with data for water available in references, as well as measurements made by a commercially-available tensiometer (SITA bubble pressure tensiometer) (Figure 15).

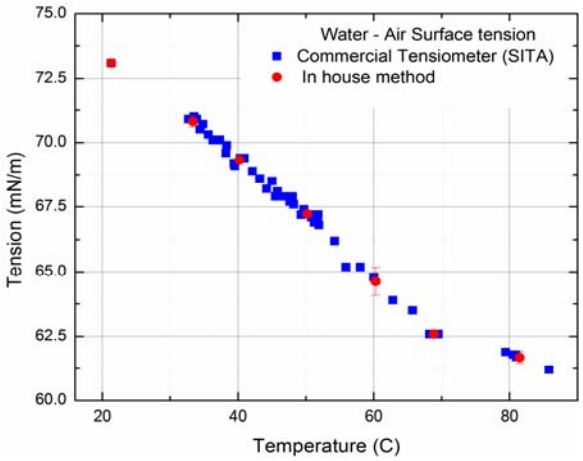

Figure 15 Surface tension of water as a function of temperature measured by commercially available tensiometer (SITA bubble pressure tensiometer) and the in-house graphical method.

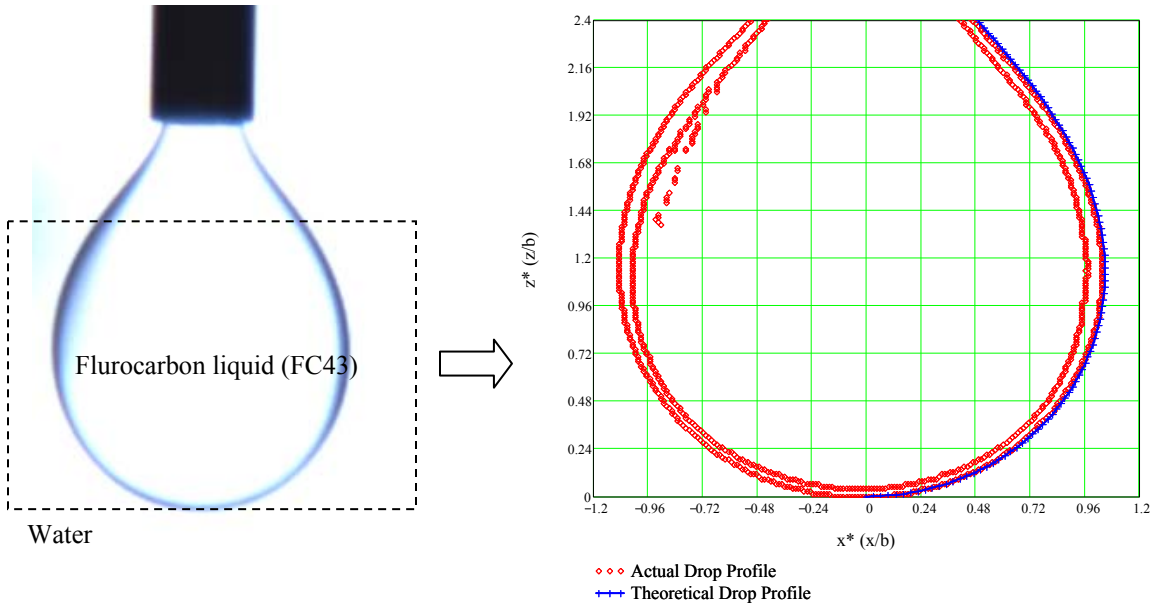

Figure 16 Left) Actual imaged pendant oil drop immersed in water (transparent); Right) By choosing an appropriate value of interfacial tension, s, the theoretical and actual drop profile overlap. The interfacial tension calculated for oil in water drops was found to be 52dyne/cm.

The unknown interfacial tension between the oil (FC43) and water at room temperature was extracted in multiple runs at identical conditions which yielded the result with less than 5% in repeatability error. It should be noted that the performance of the developed system matches with that of commercially available products and is far less expensive. A hotplate is used to maintain temperature inside the fluid chamber. Images were taken when steady temperatures were reached. Temperature was increased in increments from room temperature up to 85˚C.

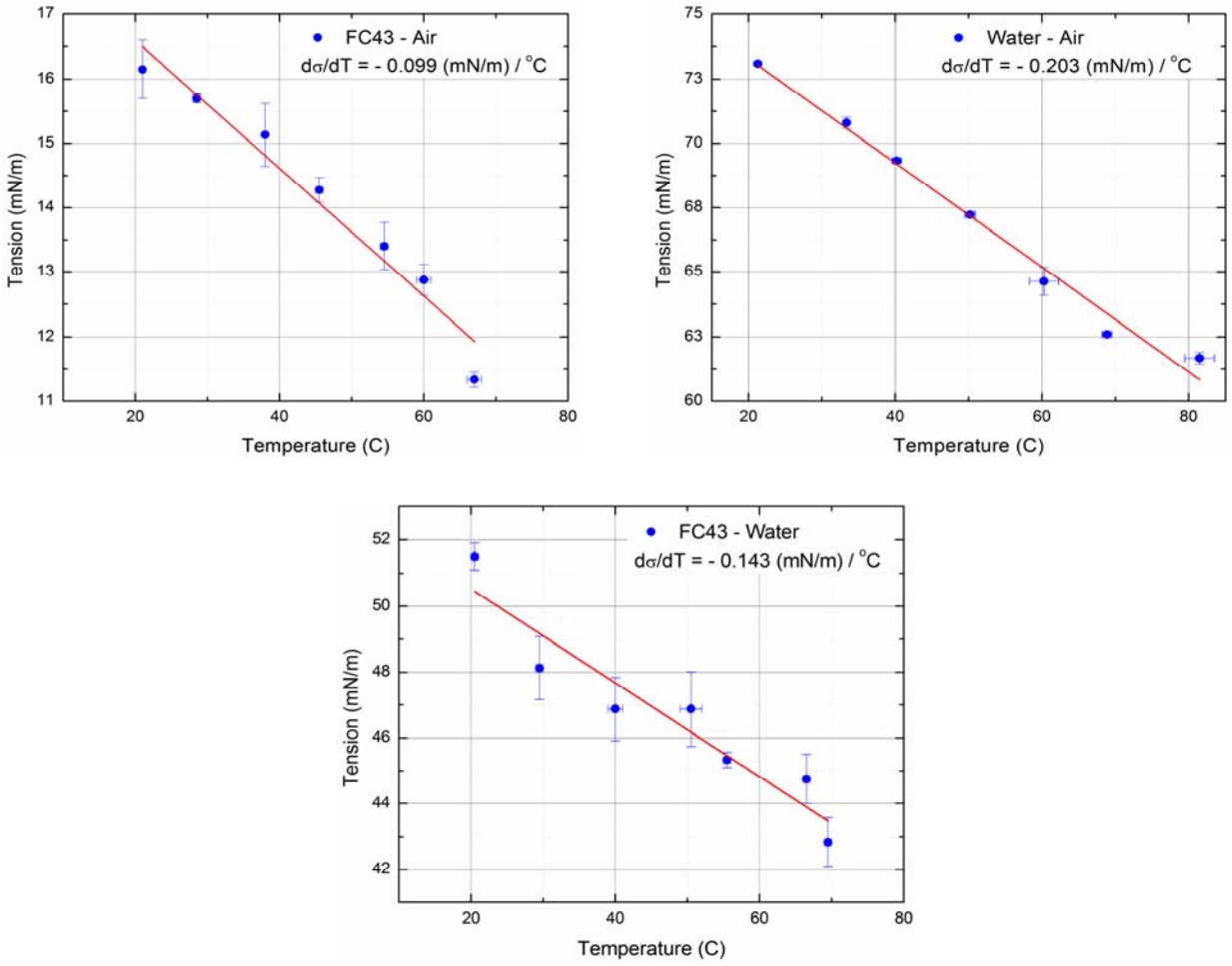

Figure 17 Variation of surface tension with temperature of fluid pairs (FC43-air, water-air, FC43-water).

For liquids (FC43 droplets in water), at higher temperatures, convective currents inside the fluid chamber caused refractive index changes resulting in blurred edges. At such high temperatures, the graphical method looses accuracy.

In summary, we studied the impact of droplets onto the surface of an immiscible liquid and demonstrated the possibility of creating isolated spherical droplets above at a liquid interface without external stimuli such as induced vibration on the surface [37] or hydrophobic coatings [39] or temperature difference between drop and target liquid [46]. Released from a controlled height and depending on their size, liquid droplets colliding on the air-liquid interface of immiscible liquids can sustain the impact and maintain their spherical integrity over the air-liquid interface. The target liquid deforms similar to an elastic membrane and causes the droplet to rebound and oscillate on the surface. The impact and the oscillation process are completed in less than 70ms due to relatively large viscous damping. Spherical droplets collapse and transform into the more stable and commonly-observed partially submerged lens-shaped configuration if any perturbations exist. The equilibrium force balance predicts only the lens-shape as the stable configuration and the extent of submergence found is in good agreement with our observations from imaging. Liquid drops resting on the free surfaces of inert liquid platforms exhibit interesting features and show promise for various applications such as material transport vehicles for lab on chips [47].

CHAPTER 3: EFFECT OF THERMAL GRADIENTS ON THIN LIQUID LAYERS

Introduction

This thesis is primarily concerned with explaining the motion of droplets at the free surface of a thin liquid layer due to a lateral thermal gradient. Partially submerged lens shaped droplets move in the direction of decreasing temperature while in this study it was discovered that spherical droplets, which form under special conditions at the interface, move in the opposite direction; i.e. direction of increasing temperatures. The primary objective of this work is to explain this dual behavior (Figure 18).

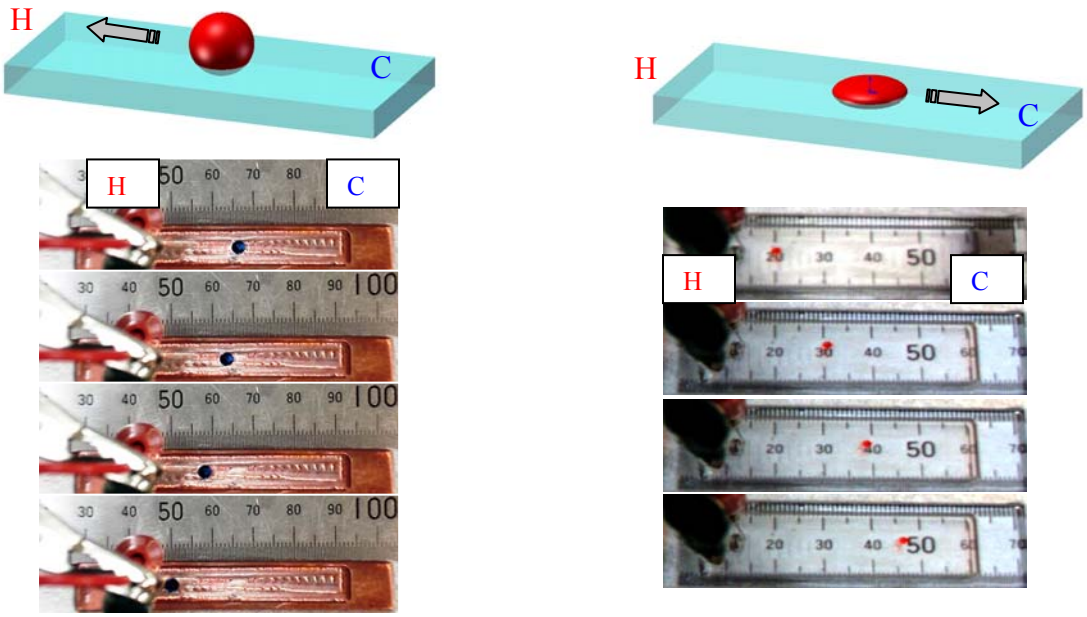

Figure 18 Snapshot images taken at Δt=0.5sec (left) an Dt=2sec (right) from the actual motion of drops showing attraction/repulsion thermocapillary motion. Spherical droplets (left) get attracted to heat source while sessile droplets (right) get repelled down the thermal gradient

The experimental setup consists of a thin liquid layer (2mm deep, 10mm wide and 55mm long) formed in a rectangular pocket. Since surface tension of most fluids varies with temperature,

thermal gradients imposed on the free surface cause surface tension gradients which in turn cause changes in the free surface profile and flow in the thin layer. Mainly, the free surface deforms such that the maximum depression occurs at the maximum temperature and an outward moving flow develops on the free surface that carries fluid from the hot end to the cold extreme of the thermal gradient. The essentials of the problem were first discussed by Levich [48-50] and later by Yih [51] and Pimputkar and Ostrach [52].

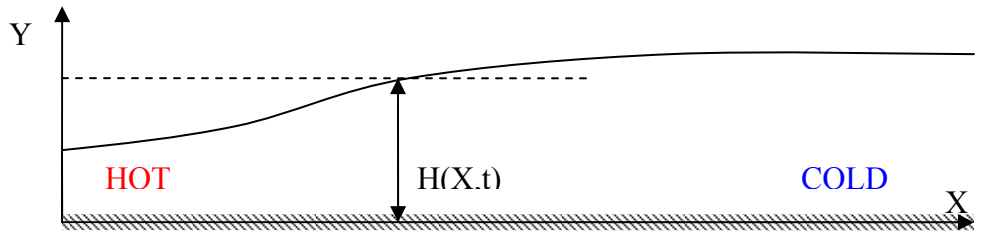

Figure 19 Schematic of the thin liquid layer subject to a thermal gradient; the thickness H and surface velocities can be found by solving the momentum and conservation of mass equations (Navier Stokes)

The governing equation for fluid flow and free surface deformation are derived from the full Navier-Stokes equation and further simplified based on order of magnitude analysis and other considerations (small aspect ratio ~1/30). The equations are numerically solved for geometrical and physical parameters of the experiments carried out in this study. The outcomes of the theoretical analysis that follows is used to explain the motion of droplets on the free surface of liquid films.

The full set of non dimensional Navier Stokes equations (continuity, momentum in x and y directions and the energy equation) and the corresponding boundary conditions are summarized below (for complete derivation and non-dimensionalization process see APPENDIX):

$$\partial u/\partial x + \partial v/\partial y = 0$$

$$\left(d^2/\upsilon\tilde{\tau}\right)\frac{\partial u}{\partial t} + \mathrm{Re}.A^2\left(u\frac{\partial u}{\partial x} + v\frac{\partial u}{\partial y}\right) = -\frac{\partial p}{\partial x} - Bo.A^2.\frac{\partial h}{\partial x} + A\frac{\partial^2 u}{\partial x^2} + \frac{\partial^2 u}{\partial y^2}$$

$$\left(d^2A^2/\upsilon\tilde{\tau}\right)\frac{\partial v}{\partial t} + \mathrm{Re}.A^4\left(u\frac{\partial v}{\partial x} + v\frac{\partial v}{\partial y}\right) = -\frac{\partial p}{\partial y} + Bo.A^2\beta\left(T_H - T_C\right)\theta + A^4\frac{\partial^2 v}{\partial x^2} + A^2\frac{\partial^2 v}{\partial y^2}$$

$$\left(d^2\,\mathrm{Pr}/\upsilon\tilde{\tau}\right)\frac{\partial \theta}{\partial t} + A^2.Ma\left(u\frac{\partial \theta}{\partial x} + v\frac{\partial \theta}{\partial y}\right) = A^2\frac{\partial^2 \theta}{\partial x^2} + \frac{\partial^2 \theta}{\partial y^2}$$

(12)

Initial condition:

$$t = 0 : u = 0, v = 0, \theta = 0, h = 1$$

Boundary conditions:

$$y = 0 : u = 0, v = 0, \theta = 0$$

$$y = h :$$

$$\frac{\partial u}{\partial y} + \frac{\partial \theta}{\partial x} = 0$$

$$\theta_{surface} = fn(x,t)$$

$$p = -\sigma A^2\left[\left|\frac{\partial \sigma}{\partial T}\right|\left(T_H - T_C\right)\right]^{-1}.\left(\frac{\frac{\partial^2 h}{\partial x^2}}{\left(1 + A^2\left(\frac{\partial h}{\partial x}\right)^2\right)^{3/2}}\right)$$

Scaling is done in the following manner:

$$x=\frac{X}{L}, y=\frac{Y}{d}, A=\frac{d}{L}, u=\frac{U}{\bar{U}}, v=\frac{V}{\bar{U}.A}, t=\frac{\tau}{\tilde{\tau}}, p=\left[P-P_{atm}-\rho g\left(H-Y\right)\right].\left(\mu\bar{U}L/d^2\right)^{-1}, \theta=\frac{T-T_C}{T_H-T_C}$$

where the velocity scale $\bar{U}=\left|\partial\sigma/\partial T\right|\left(T_H-T_C\right)\mu^{-1}$ is defined considering the fact that flow is primarily affected by surface tension effects caused by temperature differentials across the liquid layer. θ(x) is the temperature profile prescribed on the free surface.

The auxiliary equation (see details in APPENDIX) that governs the free surface profile is given as:

$$\frac{\partial}{\partial x}\int_0^h u dy+\left(L/\bar{U}\tilde{\tau}\right)\frac{\partial h}{\partial t}=0 \qquad \textbf{(13)}$$

Using initial conditions:

$$t=0: h=1$$

And boundary conditions:

$$x=0: \frac{\partial h}{\partial x}=0$$
$$x\to\infty: h=1$$

Analysis

- The assumption that the liquid layer is "thin" implies that the aspect ratio $A=d/L << 1$ and accordingly it can be assumed that $A^2 \rightarrow 0$. [In our case d_{max}=2mm and L=55mm; hence $A^2 \approx 0.0013$]
- $\beta(T_H-T_C) \approx 0.01$, $\mathrm{Re}.A^2 \approx 0.18$. [In our case, $\beta=0.0012^{\circ}C^{-1}$, considering there is a temperature differential $\Delta T \sim 10^{\circ}C$ across the length then: $\vec{U} \sim 7\, mm/s$, $\mathrm{Re} \sim 130$, $Bo.A^2 = 75$]
- Pressure change normal to the free surface due to curvature is neglected [radius of curvature is 3m which is not comparable to the characteristic length scale of the problem].
- Considering that $O(y) = A \cdot O(x)$, performing an order of magnitude analysis on the continuity equation and assuming $O(x) = 1$, shows that vertical velocity component is on the order of the aspect ratio, much smaller than unity and hence negligible:

$$\frac{\partial u}{\partial x} + \frac{\partial v}{\partial y} = 0 \rightarrow \frac{O(1)}{O(1)} + \frac{O(v)}{A \cdot O(1)} = 0 \rightarrow O(v) = A << 1$$

Accordingly the *y*-momentum equation is not entered in to the solution. Furthermore, in the *x*-momentum equation, the convective term on the left hand side term can be neglected:

$$\mathrm{Re}.A^2 \left(u\frac{\partial u}{\partial x} + v\frac{\partial u}{\partial y} \right) \approx \mathrm{Re}.A^2 \cdot O(1) \approx (10^2)(10^{-3}) \approx 10^{-1}:$$

Since there is no external pressure gradient in the x-direction and the pressure difference resulting from the curvature has been neglected ($\frac{\partial p}{\partial x} = 0$). Finally, the viscous term ($A\frac{\partial^2 u}{\partial x^2}$) is neglected because it is multiplied by the small aspect ratio (A<<1). The *x*-momentum equation in the following form is considered:

$$\left(d^2/\tilde{\upsilon\tau}\right)\frac{\partial u}{\partial t} + \cancel{\mathrm{Re}.A^2\left(u\frac{\partial u}{\partial x} + v\frac{\partial u}{\partial y}\right)} = \cancel{-\frac{\partial p}{\partial x}} - Bo.A^2.\frac{\partial h}{\partial x} + \cancel{A\frac{\partial^2 u}{\partial x^2}} + \frac{\partial^2 u}{\partial y^2}$$

$$\rightarrow \left(d^2/\tilde{\upsilon\tau}\right)\frac{\partial u}{\partial t} = \frac{\partial^2 u}{\partial y^2} - Bo.A^2.\frac{\partial h}{\partial x}$$

It should be noted that $Bo \cdot A^2 \frac{\partial h}{\partial x}$, involves the surface slope $\frac{dh}{dx}$ and is retained. Elimination of this term would result in governing equations similar to the Couette flow, which is not compatible with the physics of the problem at hand, at least for steady state solutions.

In summary, two equations govern the behavior of the thin liquid layer subject to a thermal gradient: the simplified momentum equation and the conservation of mass equation involving the thickness of the liquid layer. Simultaneous solution of governing equations gives the velocity field and the free surface profile.

$$\left(d^2 \big/ \upsilon\tilde{\tau}\right)\frac{\partial u}{\partial t} = \frac{\partial^2 u}{\partial y^2} - Bo.A^2.\frac{\partial h}{\partial x}$$

$$\frac{\partial}{\partial x}\int_0^{h(x,t)} u dy + \left(L \big/ U\tilde{\tau}\right)\frac{\partial h(x,t)}{\partial t} = 0$$

(14)

Solution Strategy

In order to solve the coupled equations, it is noted that the momentum is primarily dominated by viscous effects; hence the relevant time scale is on the order of $t_1 = \frac{d^2}{\upsilon}$. The equation governing the thickness involves the longitudinal domain and the relevant time scale would be on the order of $t_2 = \frac{L}{U}$. In other words, variations in thickness occur on the time scale of t_2 which is greater than t_1 ($\frac{t_1}{t_2} = \mathrm{Re}\left(\frac{d}{L}\right)^2 = \mathrm{Re}\cdot A^2 << 1$) [52].

The transient term in the momentum equations can be neglected when solutions are acquired on the larger time scale. The parametric solution to the momentum equation follows by integration:

$$u = Bo.A^2\frac{\partial h}{\partial x}\frac{y^2}{2} + C_1 y + C_2$$

Integration constants C_1 and C_2 are found by using the boundary conditions ($\theta_x \equiv \frac{\partial \theta}{\partial x}$):

$$y = 0 \rightarrow u = 0 \Rightarrow C_2 = 0;$$
$$y = h \rightarrow \frac{\partial u}{\partial y} = -\frac{\partial \theta}{\partial x} \Rightarrow C_1 = -\left(\theta_x + Bo.A^2 h\frac{\partial h}{\partial x}\right)$$

$$u = Bo.A^2 \frac{\partial h}{\partial x}\frac{y^2}{2} - Bo.A^2 \frac{\partial h}{\partial x} yh - y\theta_x$$

(15)

By replacing u in the conservation equation the following relationship is found for $\tau \sim t_2$:

$$\frac{\partial h}{\partial t} = \frac{\partial}{\partial x}\left[\theta_x\left(\frac{h^2}{2}\right) + \frac{Bo.A^2}{12}\frac{\partial}{\partial x}\left(h^4\right)\right]$$
$$t = 0 \rightarrow h = 1$$
$$x_{\rightarrow\infty} \rightarrow h = 1$$
$$x = 0 \rightarrow \frac{\partial h}{\partial x} = H_{x\_0}$$

(16)

This equation is solved numerically using the partial differential equation solver in MATLAB.

Validation of Solutions

The physical properties of the fluids used in experiments are given in Table 1.Water droplets are dispensed on the free surface of fluorocarbon liquid, Perfluorotributylamine (FC 43). The major outcomes predicted by the current model –*deformation of the free surface and an outward moving flow at the free surface* – are used to explain the dual direction of motion of droplets at the surface of thin liquid layers subject to lateral thermal gradients.

Table 1 Physical properties of aqueous droplet and the fluorocarbon carrier liquid

	ρ	N	k	β	σ	dσ/dT
	[g/cm^3]	[centiStoke]	[W/mºC]	[1/ºC]	[10^{-3}·N/m]	[(10^{-3}·N/m)/ºC]
FC-43	1.88	2.8	0.066	$1.2 \cdot 10^{-3}$	16	-0.099
Water	1	1	0.58	$0.21 \cdot 10^{-3}$	71	-0.20
FC-43 /Water					52	-0.14

Using aspect ratio ($A = d/L \approx 1/30$) and the range of temperature difference across the surface ($\Delta T = T_h - T_c$) from 5 – 25˚C, the non dimensional parameters are given in Table 2

Table 2 Range of Scaling parameters in experiments

$U\left(mm/s\right)$	Re	Pr	$Bo \times 10^4$	$Ma \times 10^4$	$Ca \times 10^{-3}$	τ_1(s)	$\tau_2(s)$
$\left\|\frac{d\sigma}{dT}\right\| A(T_h - T_c)\frac{1}{\mu}$	UL/υ	υ/α	$\frac{\rho g L^2}{\left\|\frac{d\sigma}{dT}\right\|(T_h - T_c)}$	$\left\|\frac{d\sigma}{dT}\right\|\frac{1}{\mu\alpha}L(T_h - T_c)$	$\frac{\mu U}{\sigma}$	d^2/υ	U/L
7.5 - 20	150 - 390	84	1.9 – 5.1	1.2 − 3.3	2.5 − 6.5	1.43	2.8 − 7.3

The normalized temperature field imposed at the interface has the form of a exponentially decaying function: $\theta = a\exp(bx)$; typical values for coefficients are $a = 1$ and $b = -1.7$ .The model provided here is based on the assumption that the thin layer of liquid extends to infinity; however, mathematically speaking a finite number must be chosen to achieve the numerical solution. One way to assign a numerical value for infinity is to extend the steady-state solution

far enough such that the resulting profile flattens out completely (i.e. $h = 1 \,\&\, \partial h/\partial x = 0$). Figure 20 shows the value of the far field slope of the free surface for extended solutions x_∞ of 3 and higher result in a far field slope reasonably close to zero ($\partial h/\partial x < 10^{-3}$).

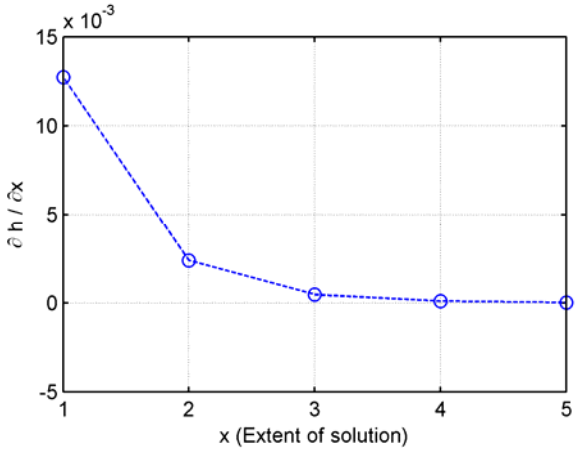

Figure 20 Solution (steady state) is extended to find appropriate value for x_∞

Results and Discussion

Figure 21 shows the free surface profile at steady state (large time). The original thickness of the layer is *(h=1)*. The deformed surface shows a deficit in the total volume (integral under the curve); in other words the conservation of mass seems to be violated. However, taking into consideration the assumption that the liquid layer is infinite allows for the excess volume to be disbursed in the far field. To better explain this, the transient evolution of the free surface is considered.

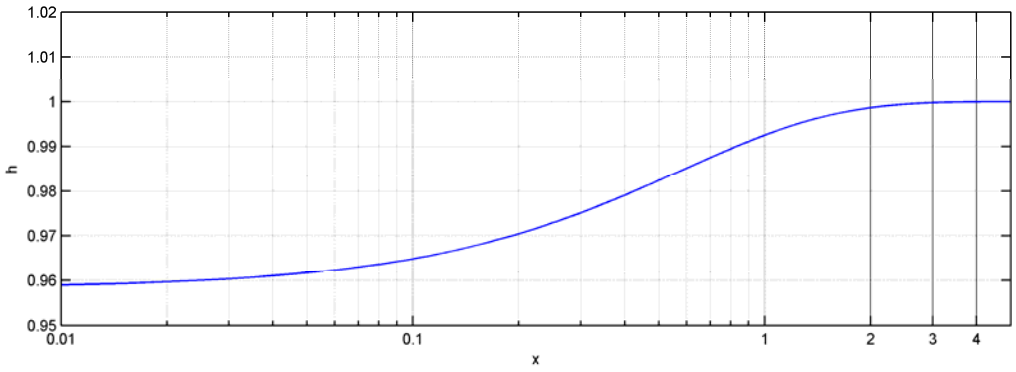

Figure 21 Free surface profile at large times for A=1/30, ΔT=22˚C (Bo = 2.8x10^4, Ma = 2.5x10^4)

Figure 22 shows the transient response of the thin liquid layer subject to the imposed thermal gradient. It is seen that the hump generated on the right side of the depressed region, moves towards the far field as time progresses, carrying away the excess liquid to form the permanent depression. This hump dies out for large times (steady state solution).

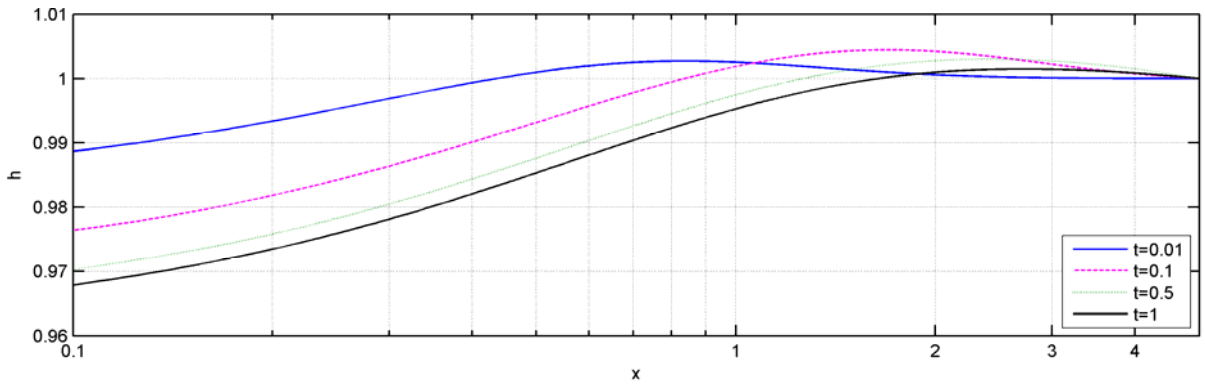

Figure 22 Transient behavior of the liquid layer; A=0.03, ΔT=22˚C (Bo = 2.8x10^4, Ma = 2.5x10^4); τ=3.5s (time scale used for non-dimensionalization

In the experiments, the liquid layer was formed in a shallow rectangular pocket and temperature gradient was provided by a coiled Ni-chrome wire heater. From the sequence of images taken at short times following the development of the thermal gradient, it is seen that the free surface deforms with a downhill slope towards the maximum temperature where the maximum depression occurs. A slight overshoot above the dotted line (original flat surface) is observed which is compatible with the predictions of the theoretical model. The depression can also be noticed on the close up images taken of the heating coils (Figure 23, Free Surface Deformation Video) when the heater is OFF and when it is turned ON.

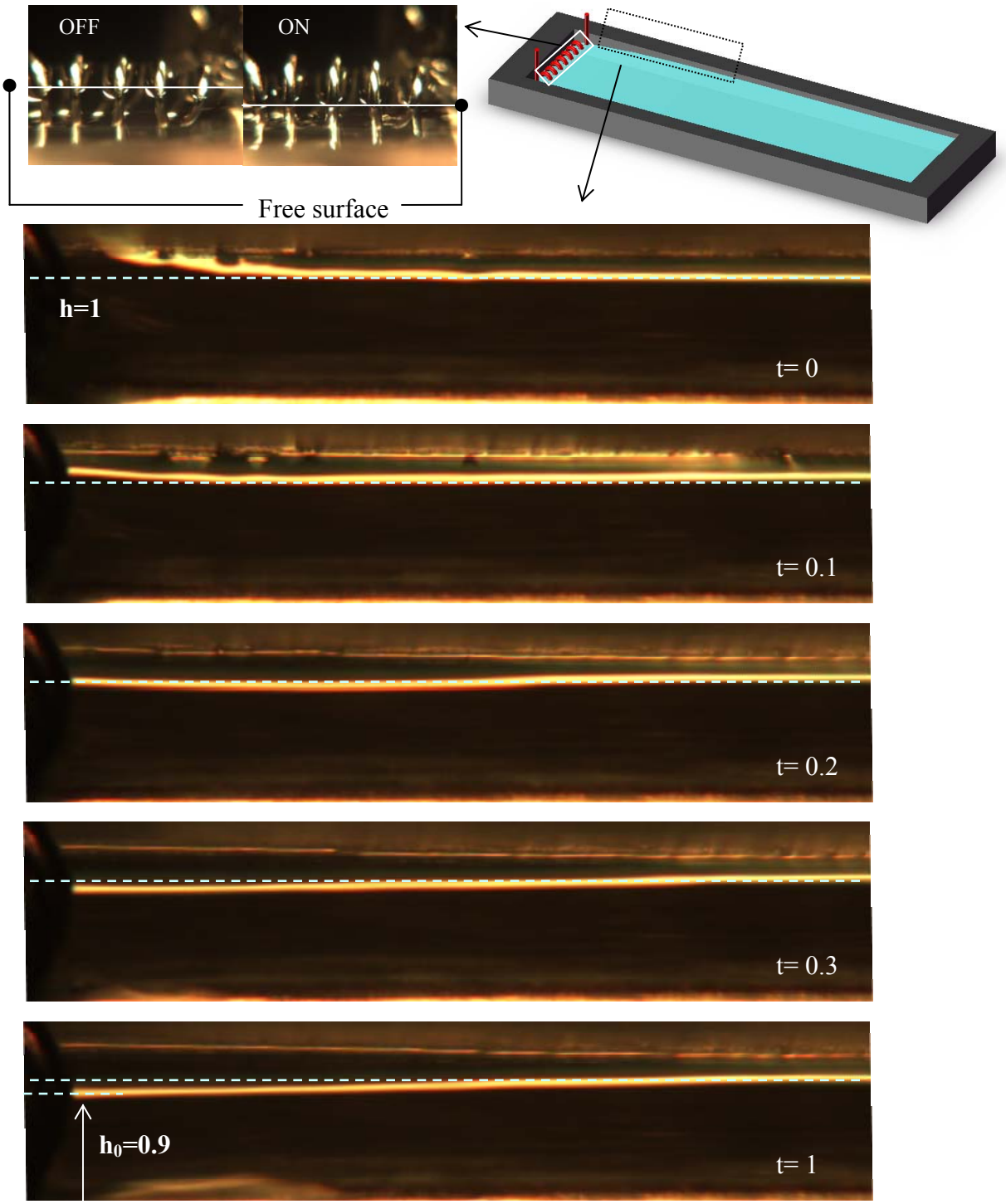

Figure 23 Depression of the thin FC 43 layer (d=1.75mm); ΔT=22°C, τ=3.5s, A=0.03, (Bo=2.8x10^4, Ma=2.5x10^4)

Comparison of maximum depression from theory (h_0=0.965) and experiment (h_0=0.9) are in good agreement (~7% difference) at steady state. The numerical model is solved for various temperature differentials (steady state) to investigate the effect of temperature gradient magnitude on surface deformation.

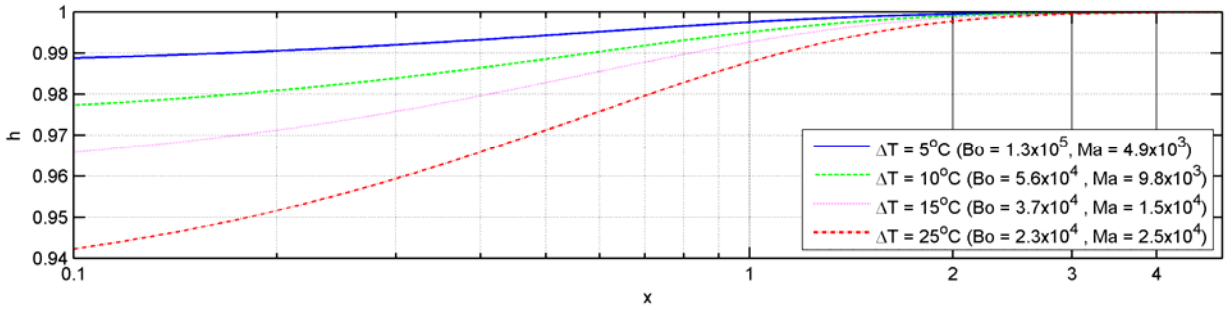

Figure 24 Effect of $\Delta T = T_h - T_c$ on the deformation of the free surface (normalized temperature field at the free surface has the form $\theta = ae^{-bx}$, a=1, b= -1.7)

In addition to surface deformation, an outward moving flow develops on the surface. The viscous stress due to flow, balances the shear stress generated due to surface tension gradient on the surface. Figure 25 shows the velocity profile across the depth of the liquid layer at various locations along the length for short (t=0.01) and large times (t=1). Noting velocity profiles it is seen that the flow develops from a Couette-like nature to a circulatory flow as time progresses.

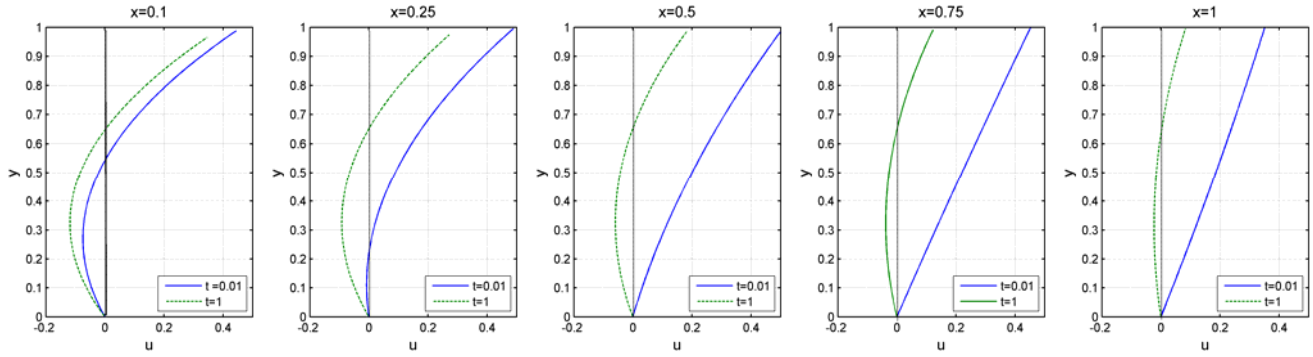

Figure 25 Velocity profiles across the layer at t=0.01 and t=1 (A=0.03, ΔT=22˚C, Bo = 2.8×10^4, Ma = 2.5×10^4). The outward moving Couette flow(solid blue line at x=1, t=0.01) develops into a recirculation flow as time proceeds. Recirculation forms in regions close to maximum temperature (x=0) first and progresses far field as steady state is achieved.

The motion of the lens shaped droplet is explained based on the outward moving flow on the free surface (y~1). As seen in Figure 26, for time scales larger than t=0.1 (~ 0.3s), the surface velocity does not vary significantly with time. This is a key result, since the velocity of the lens-shaped droplets which are driven from hot to cold end of the platform is compared to the steady state surface velocity (t>1). Experimental results suggest the monotonic decrease in drop velocity which is similar to the behavior of the surface flow found by the theoretical model.

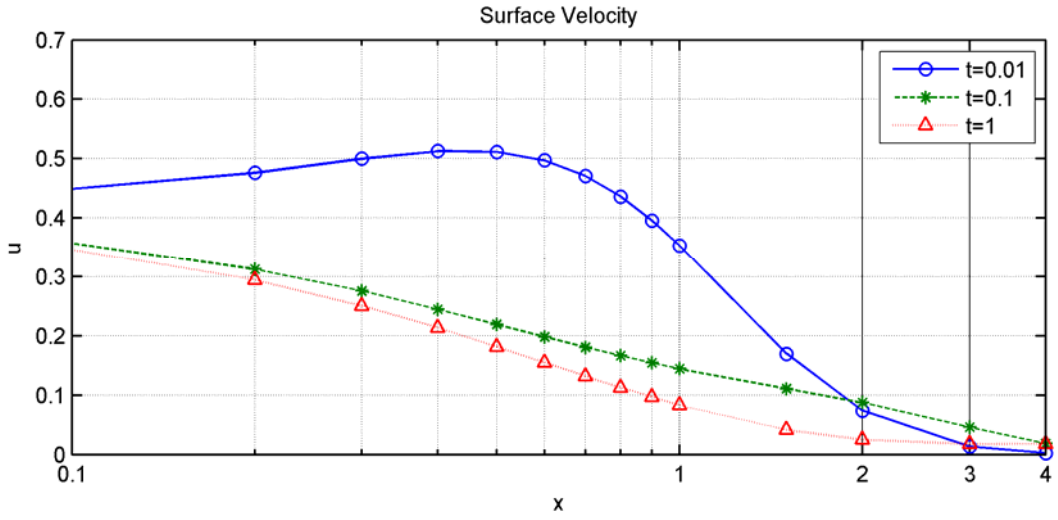

Figure 26 Velocity at the free surface at instances t=0.01, t=0.1 and t=1 (ΔT=22°C, τ=3.5s, A=0.03, $\bar{U}$ =15mm/s, Bo=2.8x10^4, Ma=2.5x10^4, Re=290).

A number of simplifying assumptions have been made in the theoretical model. First, the experimental setup is a bounded domain where as the fluid domain in the theoretical model is assumed to be unbounded for making the analyses simple. The vertical component of the flow and the end effects, where flow completely reverses, has been neglected. Sen and Davis [53] provided an analytical solution for steady thermocapillary flow in two dimensional slots where the entire flow field is divided into two distinct regions: 1) near wall boundary region where flow reverses direction and turns around to conserve mass forming a recirculation loop and 2) the core flow where only longitudinal velocity is significant. In their analysis, flow in the two domains were solved separately and later joined by the use of an asymptotic matching procedure. Furthermore, the laminar flows caused by surface-tension variation can be unstable and in such conditions the longitudinal variation of velocity cannot be ignored [54] which is not taken into account in this study.

In summary the behavior of droplets resting at the free surface of a thin liquid layer subject to thermal gradients can be explained based on the outcomes of the theoretical model. The surface events – deformation of free surface and development of a flow moving from the hot side towards the cold side – cause droplets with different interfacial configurations to drift in different directions; lens droplets that are partially submerged in the underlying liquid move along with the fluid at the surface being carried away towards colder regions. Numerical simulations of thermocapillary motion of interfacial droplets by Greco and Grigoriev [14] suggest that the dominant contribution to the migration speed is given by the advection of the surrounding flow. We explain motion of the spherical droplets, supported at the interface like a solid object on an elastic membrane, considering the free surface slope generated by the lateral thermal gradient. Droplets move towards the shallowest regions of the liquid layer which happen to be the hottest locations across the liquid film. In other words the motion is a result of the gravitational pull and the opposing drag exerted by the free surface flow moving in the opposite direction. Details of the physical model developed to describe the motion of spherical droplets are provided in Chapter 5

Levitation of Droplets on Liquid Surfaces

Non-coalescence of droplets on liquid pools has been attributed to the existence of an air gap [33, 55]. Electrical or magnetic fields, high viscosity ratio between the droplet and the liquid pool, or presence of thermocapillary flows can sustain the air (gas) film that separates adjacent bodies of fluid, preventing coalescence in the case of similar drop and film liquids or collapse of the droplets into partially submerged lens configurations. Considering thermocapillary effects, it has been experimentally and numerically shown that a droplet can be kept floating on the surface of

a liquid pool by maintaining a temperature difference between the droplet and the liquid pool [46]. Similarly, coalescence of a droplet into a liquid pool can be prevented by setting the pool into a vertical vibration [35]. The fact that an active external source of stimulation is required to prevent the droplet from coalescing (collapsing) into the underlying pool suggests that that the thin air gap is continuously drained and replenished. Non-coalescent droplets of water formed on a fluorocarbon liquid (FC-43) film in isothermal conditions and without external stimulation were observed to be relatively short-lived [56]. This is due to the complete drainage of the air film leading to the collapse of the droplet into the underlying liquid pool.

The entrainment and drainage of air in the thin gap between liquids is related to the relative motion of the fluid interfaces, which in turn is generated due to surface tension gradients across interfaces. Two possibilities exist: i) air is trapped in a gap with closed boundaries between fluid interfaces ii) air drains in and out of the gap with open boundaries. The first is ruled out because trapped air implies that non-coalescent droplets can exist at the surface permanently, while this is not true. The assumption that drainage of air within the thin gap is able to sustain the droplet weight requires that there be a pressure build up due to the motion of air within the gap [57]. The build up of pressure due to motion in the narrow gap between fluidic interfaces can be understood and modeled with reference to the theory of *Low Reynolds number Flows* and *Lubrication* where significant parameters involve pressure, viscosity and moving walls forming inclined narrow gaps (Figure 27) [58].

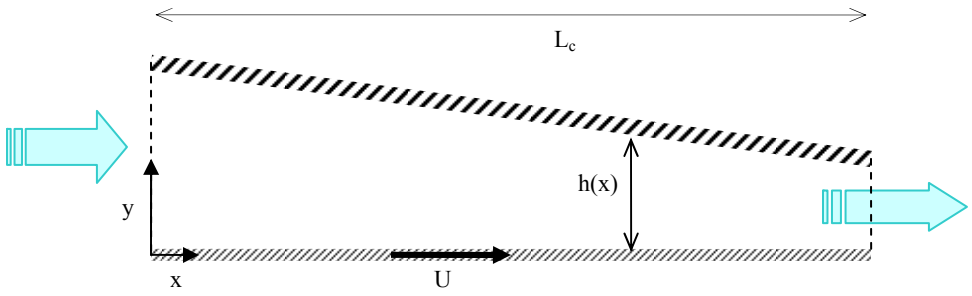

Figure 27 Schematic of flow in a narrow gap (h/L→0) with inclined (small slope) moving wall which is a combination of Couette and Poiseuille flow.

A moving wall sweeps fluid into the narrowing passage resulting in a flow which is a combination of Couette flow and Poiseuille flow. The scaling factors are: $x \sim L_c$, $y \sim h$ and considering continuity, $v \sim {Uh_{in}}/{L_c}$. The pressure in inertia-less flows in usually scaled by $p \sim \frac{\mu U L_c}{h_{in}^2}$. The momentum equation is simplified based on the assumption of low Reynolds number and $h/L_c \rightarrow 0$ (z component of the flow is neglected by assuming a two dimensional configuration; in other words infinite length in z as compared to the gap thickness). The simplified momentum equation in the direction of flow is as follows:

$$0 = -{\partial p}/{\partial x} + \mu \frac{\partial^2 u}{\partial y^2}$$
$$u_{y=0} = U, u_{y=h} = 0$$

(17)

Integration of equation 17 provides the velocity profile which is the sum of a Couette and Poiseuille component:

$$u = \frac{1}{2\mu}\left(\frac{\partial p}{\partial x}\right)\left(y^2 - yh\right) + \left(1 - {y}/{h}\right)$$

(18)

Considering the original problem of non-coalescing droplets, it is assumed that the pressure buildup in the air gap is due to the moving interfaces, which prevents fluid surfaces to come in direct contact and cause coalescence for similar liquids or collapse of droplets into partially submerged lens configurations in the case of immiscible liquids. It is essential to find the pressure distribution within the air gap based on the relative wall velocities.

Integrating the continuity equation over y from 0 to h, and using the Leibnitz theorem gives:

$$\int_0^h \left(\frac{\partial u}{\partial x} + \frac{\partial v}{\partial y}\right) = \frac{\partial}{\partial x}\int_0^h u dy$$

(19)

since $\int_0^h {\partial v}/{\partial y}\, dy = v_{y=h} - v_{y=0} = 0$; substituting u from equation 18, and carrying out the integration in equation 19 leads to:

$$\frac{1}{\mu}\frac{d}{dx}\left(\frac{\partial p}{\partial x}h(x)^3\right) = 6U\frac{dh(x)}{dx}$$

(20)

From equation 20 and knowing the geometry of the air gap *h(x)*, wall velocity U_s and viscosity of fluids, the pressure field can be found by integration over *x* and using appropriate boundary conditions for pressure at inlet and outlet (ambient pressure is chosen at the boundaries). The

integration constant h_C, corresponds to a gap height were pressure is maximum ($\partial p / \partial x = 0$). Using the scaling factors introduced above, the non dimensional equation that relates the pressure field to the height in the narrow gap is:

$$\frac{dp^*}{dx^*} = 6\left(h^{*-2} - h_C^* h^{*-3}\right)$$

(21)

An order of magnitude analysis can be used to approximate the gap size required to build the necessary pressure to sustain the weight of the droplet ($\Delta PA_{projected} \approx m_{drop} g$). From the thermocapillary analysis and experimental data, the fluid interfaces were found to move with a typical velocity scale of U_s~ *20 mm/s*; considering the pressure scale ($\Delta P \sim \frac{U_s L_c \mu_{air}}{\left(\bar{h}\right)^2}$), it is concluded that for a drop of water with a diameter of *3mm*, the gap thickness should be $\bar{h} \sim 7 \mu m$ using the following relationships and (Figure 28):

$$\Delta PA_{projected} = \Delta P \pi \left(\underset{=R\sin\phi}{R_c} \right)^2 \approx m_{drop} g = \left(\frac{4}{3} \pi R^3 \right) \rho g$$

$$\Delta P \sim \frac{U_s L_c \mu_{air}}{\left(\bar{h}\right)^2}$$

$$\bar{h} \sim \left[\frac{3}{2} \frac{U_s \varphi \left(\sin\varphi\right)^2 \mu_{air}}{\rho g} \right]^{1/2}$$

(22)

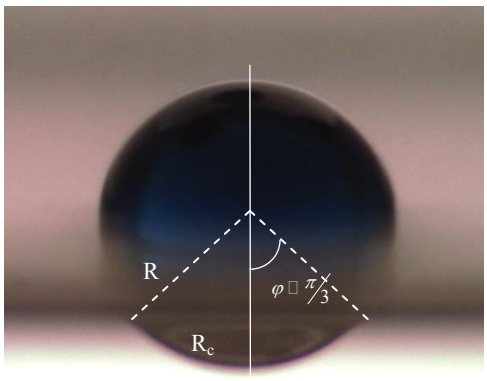

Figure 28 A spherical drop of water resting above the surface of a pool of FC 43 liquid.

The air gap thickness is on the order of micrometers, which is three orders of magnitude smaller that the drop diameter. This allows us to treat the gap at the interface between the droplet and the underlying liquid to be a narrow gap formed between infinite flat surfaces with a slight incline (relative wall motion will not cause any pressure build up within parallel plates). The gap thickness is assumed to vary with a small linear slope with respect to the length of the gap as shown in (Figure 27).

The numerical solutions to equation 21 has been carried out below for various linear slopes ($s = \frac{h_{in} - h_{out}}{h_{in}}$) and it is found that pressure build up increases with the increase of the incline. It is also noted that the dimensional pressure buildup (P-P_{ref}) scales with the relative interfacial velocity.

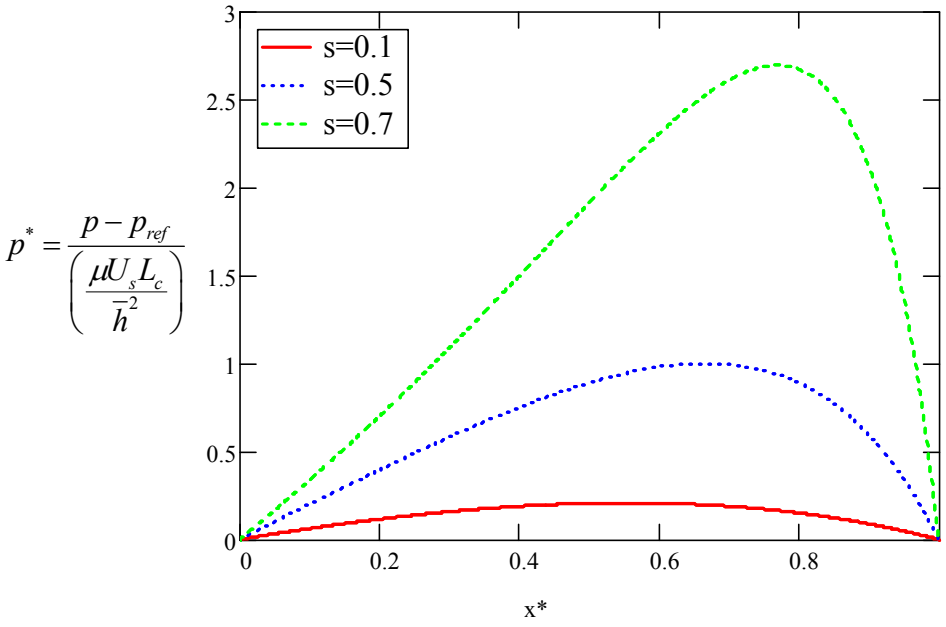

Figure 29 Pressure build up in the air gap. The gap geometry has been simplified as a narrowing gap with a small constant slope as shown in Figure 27

As noted earlier, due to extremely small $\bar{h}/L_c$ ratios, the gap between the drop and the underlying liquid can be modeled as flat surfaces. The flat surfaces are considered here as circular disks. The characteristic length scale L_c, as the average cord length (gap length) over the projected area A_p, of the drop on the liquid pool is:

$$L_c . A_p = \int L_{cord} dA_p \tag{23}$$

where $L_{cord} = R_c \cos\theta$ and $A_p = \pi R_c^{\,2}$

Integration of the normalized pressure difference p^*, over the projected area and multiplication by the scaling factor provides a vertical force, which is found to be comparable to the weight of the droplet; for example for a droplet with a radius of *R=1.5mm, R_c=Rsin(π/3):*

$$\left[\left(\frac{\mu U_s L_c}{\bar{h}^2}\right)\int_0^1 p^* dx^*\right]\left(\pi R_c^{\,2}\right) \approx 0.25mN$$
$$\frac{4}{3}\pi R^3 \rho g \sim 0.14mN \qquad \textbf{(24)}$$

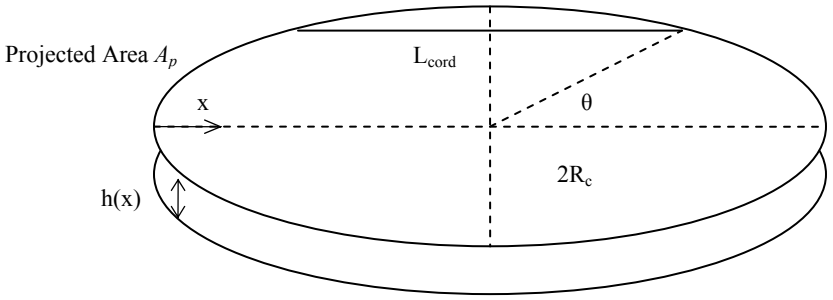

Figure 30 Surface between the drop and underlying liquid is modeled as a flat circular surface.

In the range of thermally-induced interface velocities, the air gap thickness is found to be a few micrometers. Similar values have been reported for droplets levitated on liquid surfaces having a radial flow (14μm) [57] and drops floating on liquid pools due to temperature difference (1-10μm) [55]. Here, not only the drop is levitated above the liquid pool without coalescing (collapsing) but also propelled by the imposed thermal gradients in the desired path. Pressure build up due to entrainment of flow due to the relative motion of fluidic interfaces explains long-lived levitated droplets above the surface.

CHAPTER 4: EXPERIMENT RESULTS OF DROPLET MOTION ON A LIQUID LAYER DUE TO THERMAL GRADIENTS

Experiment

A thin liquid layer is formed in a shallow pocket, cut in rectangular slabs made of acrylic (thermal conductivity $k=0.2\ W.m^{-1}K^{-1}$) and copper ($k=400\ W.m^{-1}K^{-1}$). When placed on heat sinks (large metal block), different thermal conductivity containers, transient and steady thermal gradients of various slopes can be created. The thermal gradient was created by using a Ni-chrome wire heater (Gauge 28, 4.15 Ω/ft, Pelican) as a heating element by passing current through it. The transient thermal field in the liquid layer was measured initially by placing fine wire thermocouples (K Type, beaded wire exposed G27, Omega) along the length. Such thermocouples have a response time on the order of 0.4 seconds (measurement time needs to be at least 5 times the response time) and accuracy of ±1.5˚C within a range of -40 to 375˚C. From Figure 31 it can be seen that in a transient mode, steeper gradients are achieved using the copper base as compared to acrylic. In addition, temperature recovery is achieved within a shorter period of time in copper containers compared to acrylic containers, which is expected due to the significantly larger thermal conductivity or in general lower thermal resistance of copper for heat dissipation.

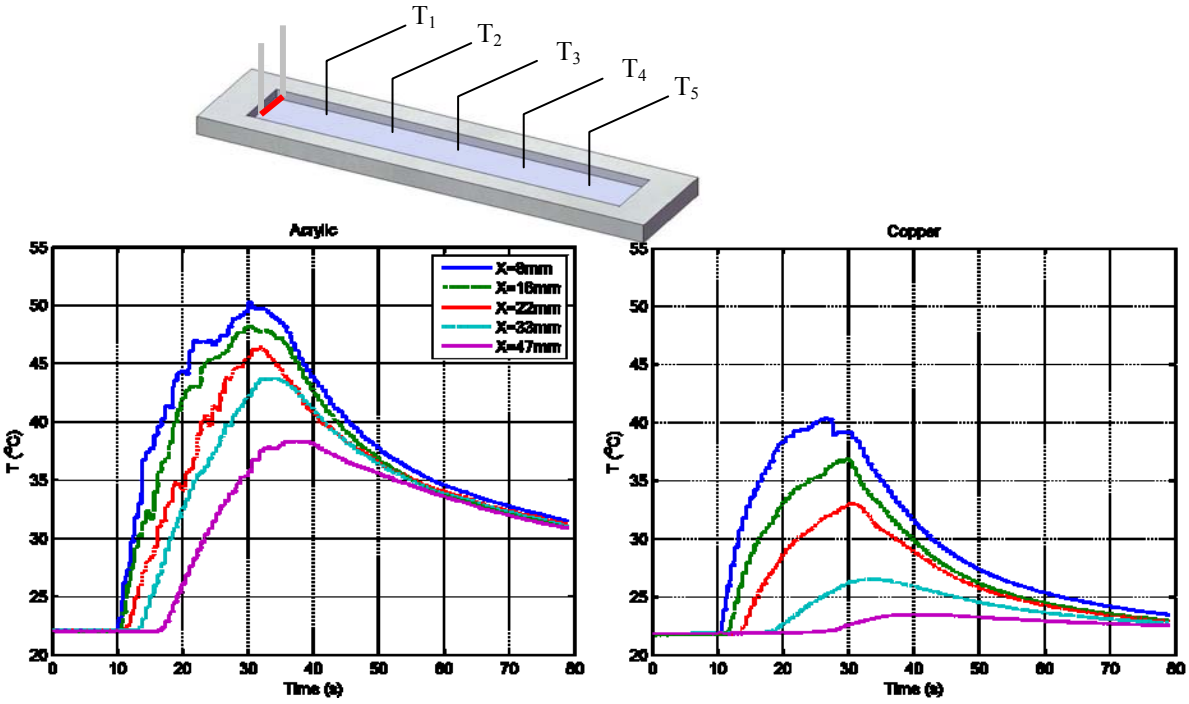

Figure 31 Measurement of temperature field using fine wire thermocouples (T_{ON}=10s, T_{OFF}=30s); q_{in}=6.2W

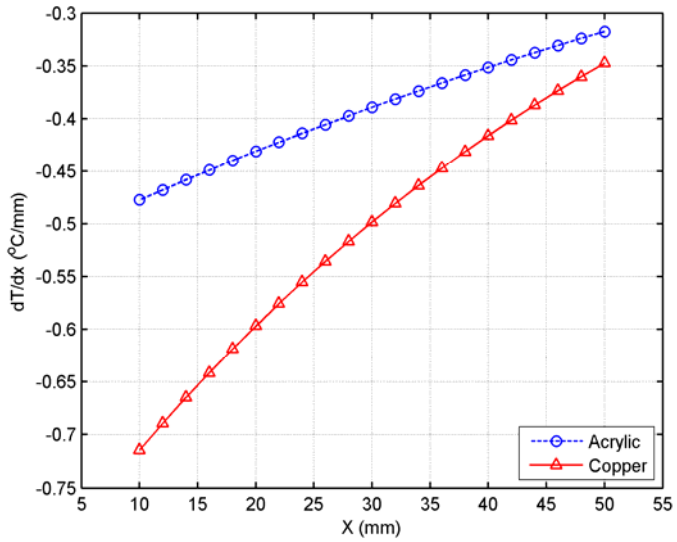

Figure 32 Thermal gradient formed in the liquid layer using acrylic and copper container (t=15 sec, q=6.2W)

Figure 32 shows the one dimensional thermal gradient across the platform measured in the thin liquid layer using an acrylic and copper containers. The simplified model for the temperature distribution across the liquid layer is heat transfer in a semi infinite body subject to a constant flux.

Lens and spherical droplets are dispensed on the liquid layer and the effect of thermal gradient magnitude and droplet size is investigated on the instantaneous and average thermally-induced velocity. Internal droplet temperature fluctuation along the migration path is measured, which is important for applications where droplets should be transported with least thermal loading.

Results

The central focus of this work is on the following observation: droplets of equal volume when placed on a liquid platform migrate in opposite direction depending on their shape (configuration) at the air-liquid interface. Equal volume droplets in the spherical and lens configuration are shown in Figure 33. Lens-shaped droplets drift away from high temperature regions (Lens Droplet Motion Video) while spherical droplets get attracted to the higher temperature end of the thermal gradient formed on the platform (Spherical Droplet Motion Video).

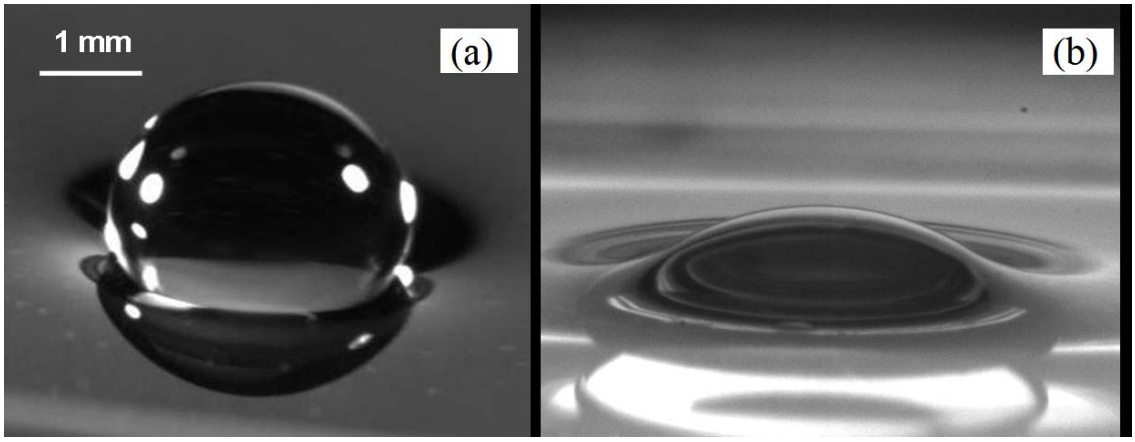

Figure 33 Drops of equal volume resting an the air liquid interface in spherical configuration (a) and lens configuration (b).

Lens Droplets

A set of experiments is carried out to investigate the effect of the thermal field (temperature gradient) on the instantaneous and average drift velocity of lens shaped droplets of various sizes.

Droplet volumes ranging from 1μL to 15 μL were used for two cases of constant heat flux $q_{in,1}$=11.9 W and $q_{in,2}$=4.3W that provided thermal gradients with different slopes. When using thermocouples, internal temperature of the droplet was found by interpolation from measurements made by the array of thermocouples at known locations. Interpolation requires the assumption that the droplets are isothermal with the surroundings (it is shown in later sections that this is assumption is not accurate using infrared real-time temperature measurements). Temperature and velocity measurements were done in two separate runs when thermocouples were used. Ample time was provided between each experiment to ensure initial conditions for all cases would be similar (room temperature). Lens droplets were dispensed by a precision micro pipette. Experiments were repeated two times for each droplet volume and thermal field (gradient).

Average velocity for smaller lens droplets was larger for similar thermal gradients. The steeper thermal gradient resulted in larger average velocity for any given droplet size (Figure 34). Since temperature on the liquid layer is available from thermocouple readings, at each instance, droplet temperature was interpolated using the location of the drop relative to the location of fixed thermocouples. An important parameter in many bio-chemical applications is that temperature fluctuations should be limited to a narrow range due to the presence of temperature sensitive bio-chemical substances in the droplets. It is found that smaller droplets migrate at higher speeds; in other words the contact time of the droplets with high temperature regions is lower as compared to larger droplets, which move with a lower drift velocity. Favorable working conditions (low temperature fluctuation) are achieved for smaller droplets showing favorable scalability for miniaturized applications.

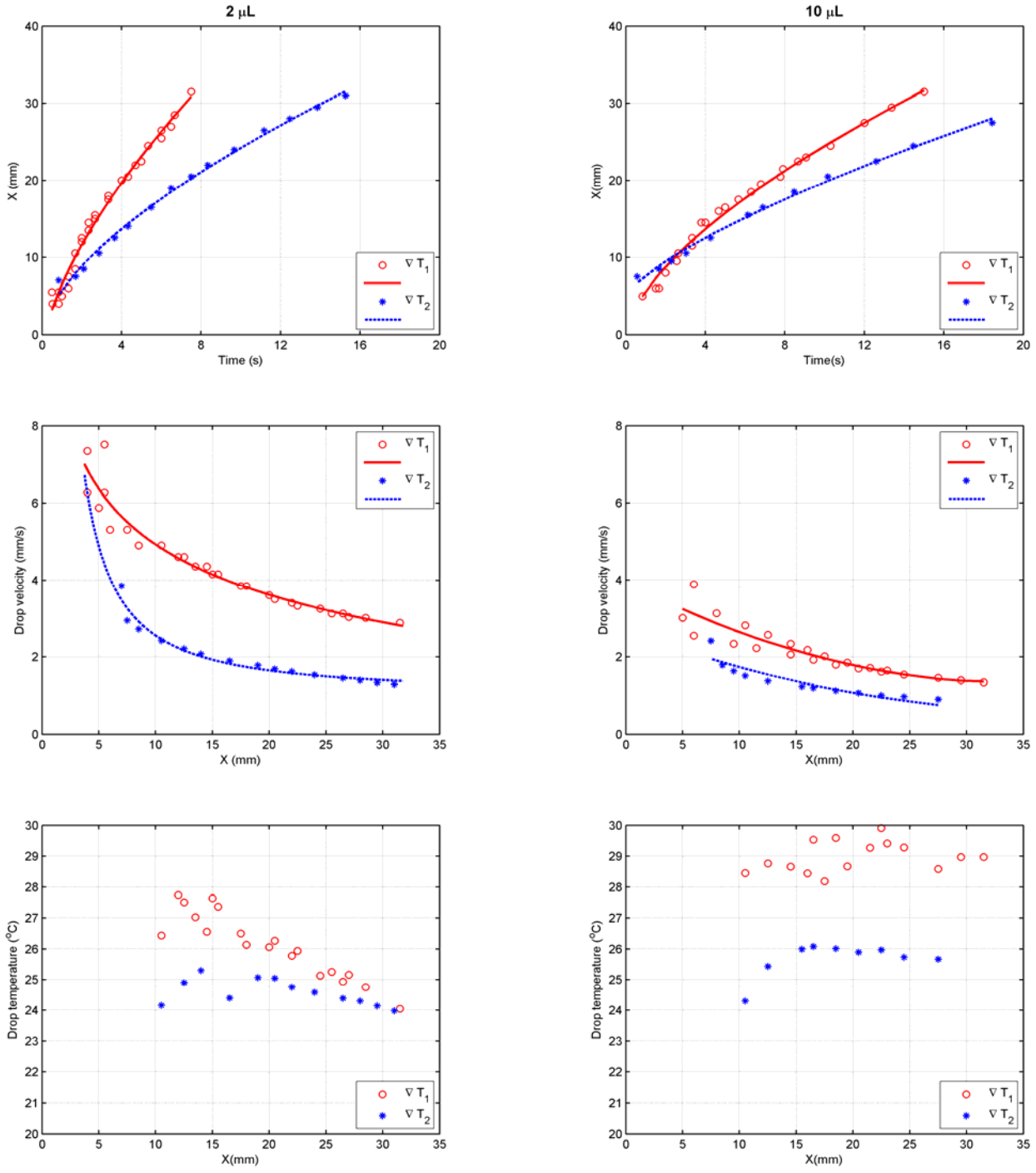

Figure 34 Effect of thermal gradient and size (volume) on motion of lens drops; q_{in_1}=11.9W, q_{in_2}=4.3W). Internal temperature of the drop is found by spatio-temporal interpolation of thermocouple readings. Left column graphs are for drop size: 2μL and right column graphs are for drop size: 10μm.

Although, steeper thermal gradients allow for larger drift velocity, it is observed that for a given droplet size, large thermal gradients cause larger increase in the internal droplet temperature (Figure 35).

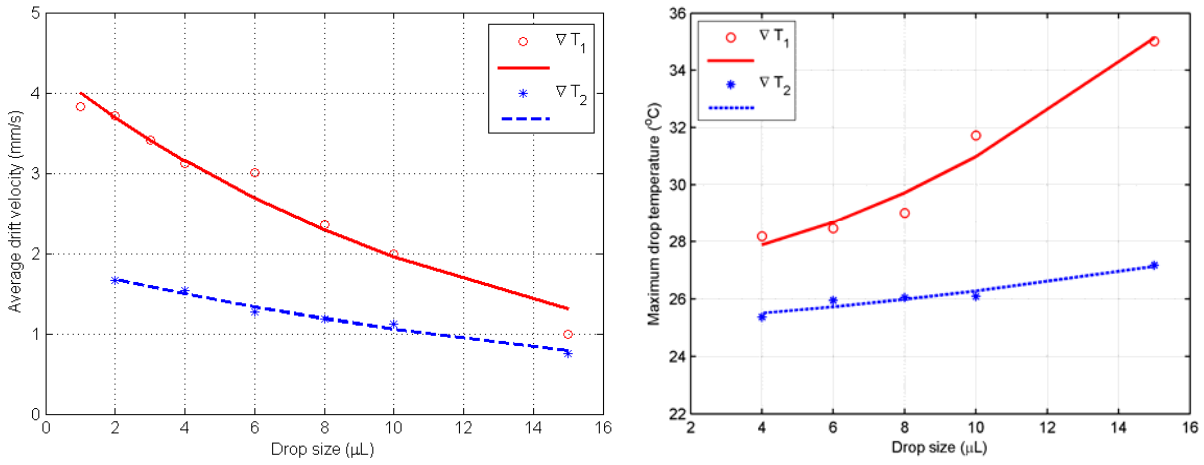

Figure 35 Average drift velocity for lens drops decreases with increasing drop size while internal temperature of drops increases. Larger thermal gradients result in higher average drift velocity for give drop size.

Temperature measurements made by thermocouples for studying thermocapillary motion of droplets in this work showed the following shortcomings:

- The temperature field across the liquid platform was approximated by curve fitting and interpolation of measurements of a limited number of thermocouples at fixed locations.
- Since the thermocouple probes would block the passage of droplets, all experiments had to be run twice. The first time to record the spatio-temporal temperature field across the platform, and the second time motion of the droplets was recorded using a video camera. As such, the temperature fields from the first and second run might not necessarily match and significant variability enters the data.

- In order to estimate the internal temperature of moving droplets a simplifying assumption was made where the droplet and the surrounding liquid were considered to be isothermal, i.e. have the same temperature. In this way, the droplet temperature could be interpolated from the readings of nearby thermocouples. This assumption is not accurate (as shown by real time infrared thermography method adopted in following subsections). In other words, due to thermal capacitance, the time scale for the droplets to acquire the temperature of the surrounding fluid is larger than the time scale over which droplets move along the length of the platform; hence they are essentially not at the same temperature as the surrounding liquid.
- Thermocouples always sense the temperature at the bimetallic junction and the accuracy of readings depends on the material within which it is embedded and the nearby surfaces. Thermocouple size, location, wire lead arrangement and materials affected the reading.

Considering the limitations mentioned above, a high-resolution, high-speed infrared thermal imaging system was used for measurement and characterization. The data presented in the following sections are real time infra red measurements.

Surface Temperature Measurement using Infrared Imaging

Infrared thermal imaging is an attractive measurement technique because it provides non-invasive spatially and temporally resolved readings of temperature on surfaces. In relevance to the current study, this technique is especially useful because surface temperature (temperature gradients) is of interest. Similar to any other measurement tool, calibration is an important issue where surface temperatures can be correlated to different shades, gray scale or a spectrum of colors. There are two forms of calibration: external and internal; external calibration is based on

analytical calculations, where a variety of thermo-physical characteristics, such as emissivity, transmittance of the ambient and the surroundings should be known. Incident radiation to the sensors is made up radiation from the surface of interest – attenuated by the transmittance of the ambient – radiation from the surrounding surfaces and the radiation that is reflected from the surface of interest.

$$I_{incident} = \tau\left(\varepsilon I_{obj} + \rho I_{surrounding}\right) + \left(1-\tau\right) I_{medium} \quad \textbf{(25)}$$

τ is the transmittance of the medium (air, vapor or gas between the sensor and measured surfaces, Figure 36) and ε and ρ are the emissivity and reflectivity of the measured surface.

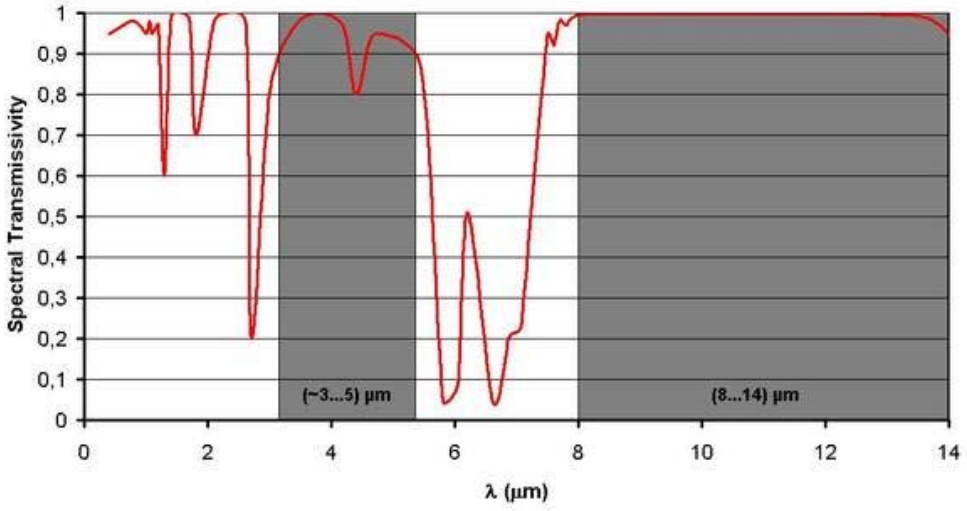

Figure 36 Spectral transmittance of air (10 m, 25 °C, 1013 mbar, 85% relative humidity)[3]

[3] http://www.infratec.de

This method of calibration is usually not practiced because exact values of the physical properties are not readily available and the irradiation from surrounding surfaces cannot be calculated or measured reliably. The emissivity of distilled water is reported to be 0.98 and this value has not been reported for FC-43 and considered similar to that of water.

On the other hand, internal calibrations are more convenient where infrared readings from the detectors are calibrated against known temperatures in every specific test setup in order to achieve a calibration function (for example in form of a polynomial function).

Two major categories of infrared cameras are available: *scanning* and *staring* devices. In the former, surface radiation is measured in a point by point manner where mirrors and prisms that oscillate or rotate transfer the signal to a single detector. The latter take advantage of an array of detectors that are arranged on the focal plane of the receiving optics. Conventionally, the infrared spectrum is divided into there three sub regions:

Far infrared (wavelength of 8 – 12 μm), mid infrared band (wavelength 2 - 5μm) and the near infra red band (wavelength 0.4 – 2 μm). For thermal applications, the mid and far infra red bands are used. Depending on the wavelength and spectral emissivity various combination of photo detector sensors (solid state devices) are used that may require cooling of the detector array for making measurements.

The infrared camera (SC 5000 FLIR) used in this study is based on InSb (Indium Antimonide – narrow bandgap semiconductor sensor) with a spectral response range of 2.5 – 5.1μm in wavelength (mid infrared). The detector array provides a 640x512 pixel digital image where each pixel is 15μm x 15μm. Using mid infrared range provides better quality temperature readings;

however it requires the sensing elements to be cooled. This camera is cooled by an internal Stirling cooler. The maximum framerate is 100 Hz and the nominal temperature measurement range is 5 – 300˚C.

Figure 37 (Lens Droplet Motion – Infrared Video) shows the platform temperature $T(X,t)$ as a function of the length coordinate *(mm)* and time *(s)*. Solid circles show the location of the droplet as time progresses. The overall slope of displacement vs. time is higher for the larger heat input (steeper gradient).

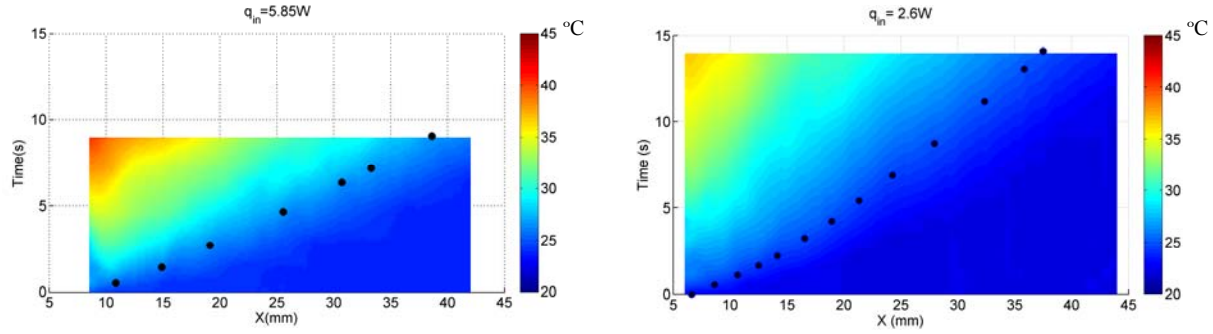

Figure 37 Spatio-temporal thermal map for q_{in_1}=5.85W (∇T_1) and q_{in_2}=2.6W (∇T_2). Solid circles show the droplet displacement as a function of time.

Based on the infrared temperature measurements, the thermal gradient experienced by the droplet as it moves across the platform was found by evaluating the temperature distribution function gradient $\partial T(x,t)/\partial x$ at X_{drop} and t_{drop}. Velocity and temperature of a 4μL droplet is shown in Figure 38 as it migrates away from the source of heat to cooler regions of the platform.

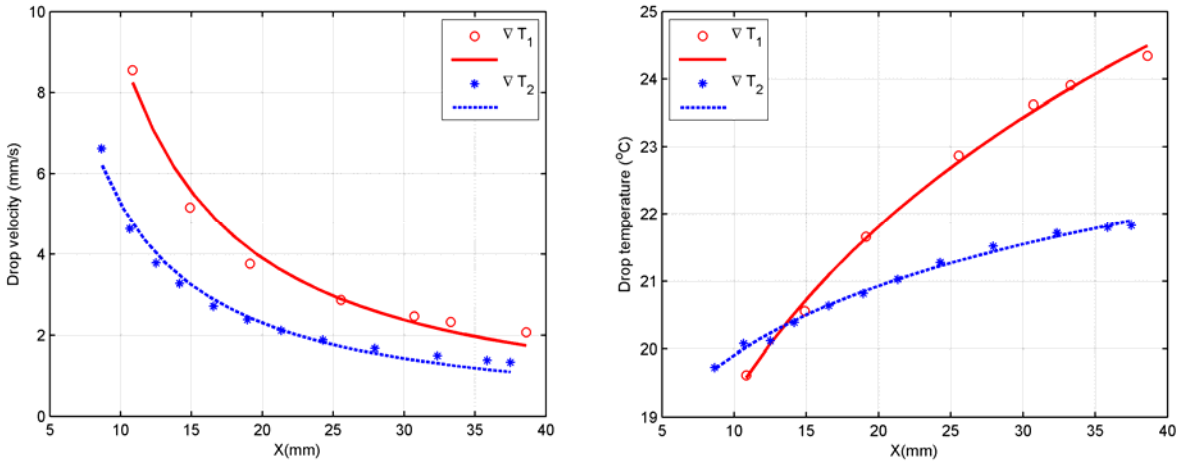

Figure 38 Lens droplet (4µL) velocity (left) and temperature increase (right) for two thermal slopes.

Droplet internal temperature increase found by direct infrared measurements shows a different trend compared to measurements made by thermocouples and confirms the shortcomings of using thermocouples as compared to real time temperature measurements on the surface droplets.

Spherical Drops

In similar experiments, droplets were dispensed on the surface of the liquid platform such that they were levitated in a spherical shape above the surface (Spherical Drop Motion – Infrared Video). Experiments were carried out in transient and steady thermal gradient conditions. In the transient condition, the platform was initially at room temperature and the heater was turned on and the thermal gradient experienced by the droplet as every location and time was recorded by evaluating $\partial T(x,t)/\partial x$ of the curve fitted to temperature measurements along the motion path. From the infrared insets, it is seen that the droplet does not move until it senses the thermal gradient. This shows that the process is dependent on gradients of temperature, rather than temperature itself; therefore droplet motion can be tuned to any temperature range as long as the required gradients are maintained. The droplet accelerated as it approached steeper gradients of

temperature, while moving towards the maximum temperature on the platform (Figure 39). The internal droplet temperature rose as it approached the high temperature regions of the thermal gradient, as expected. For example, the internal temperature of a 14μL droplet migrating due to a temperature differential of $\Delta T = T_h - T_c \sim 20^o C$ across a 45mm path rose about 8˚C.

In order to develop a better understanding of the effect of thermal gradient magnitude and droplet size on the thermally-induced motion of spherical droplets, the problem was studied using steady thermal gradients. Equal-sized spherical droplets were dispensed at the cold end of the temperature gradient. Droplets accelerated towards high temperature regions of the platform in the direction of increasing temperatures. It was seen that droplets subjected to steeper thermal gradients gained higher drift velocity; however, the internal droplet temperature raised almost 15˚C when steep gradients were implemented. In separate experiments, it was confirmed that in order for droplets to move, they should be dispensed within a critical distance from the high temperature sources where the effect of the thermal gradient could be sensed, otherwise no motion occurred. In effect, the main cause of motion was found to be the presence of a thermal gradient and steeper thermal gradients resulted in higher drift velocities.

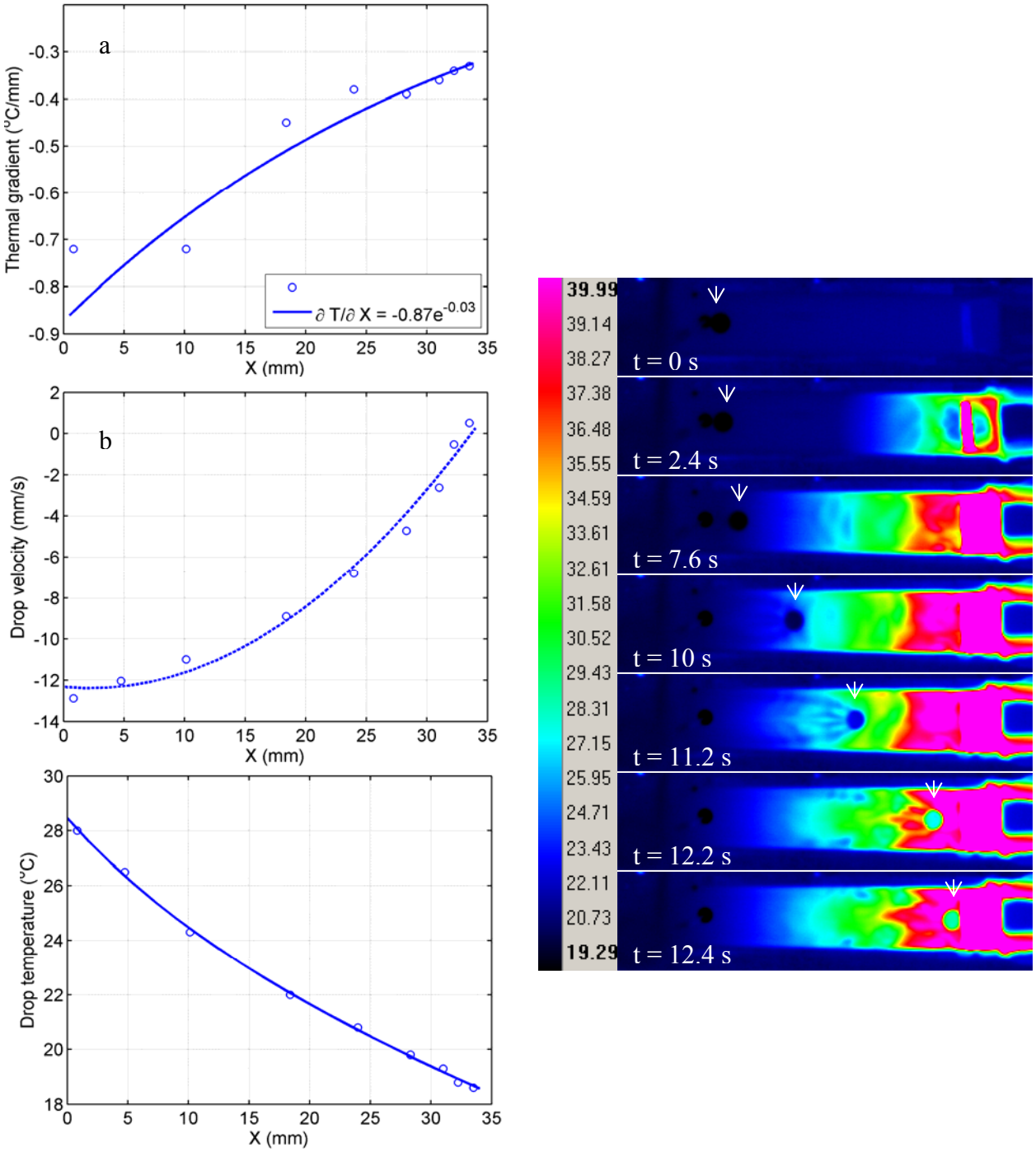

Figure 39 Motion of a spherical drop (14 µL) due to a transient thermal field. Left a) thermal gradient felt by the drop along the path b)instantaneous drop velocity c) change of drop temperature. Right column shows the infrared images at select times.

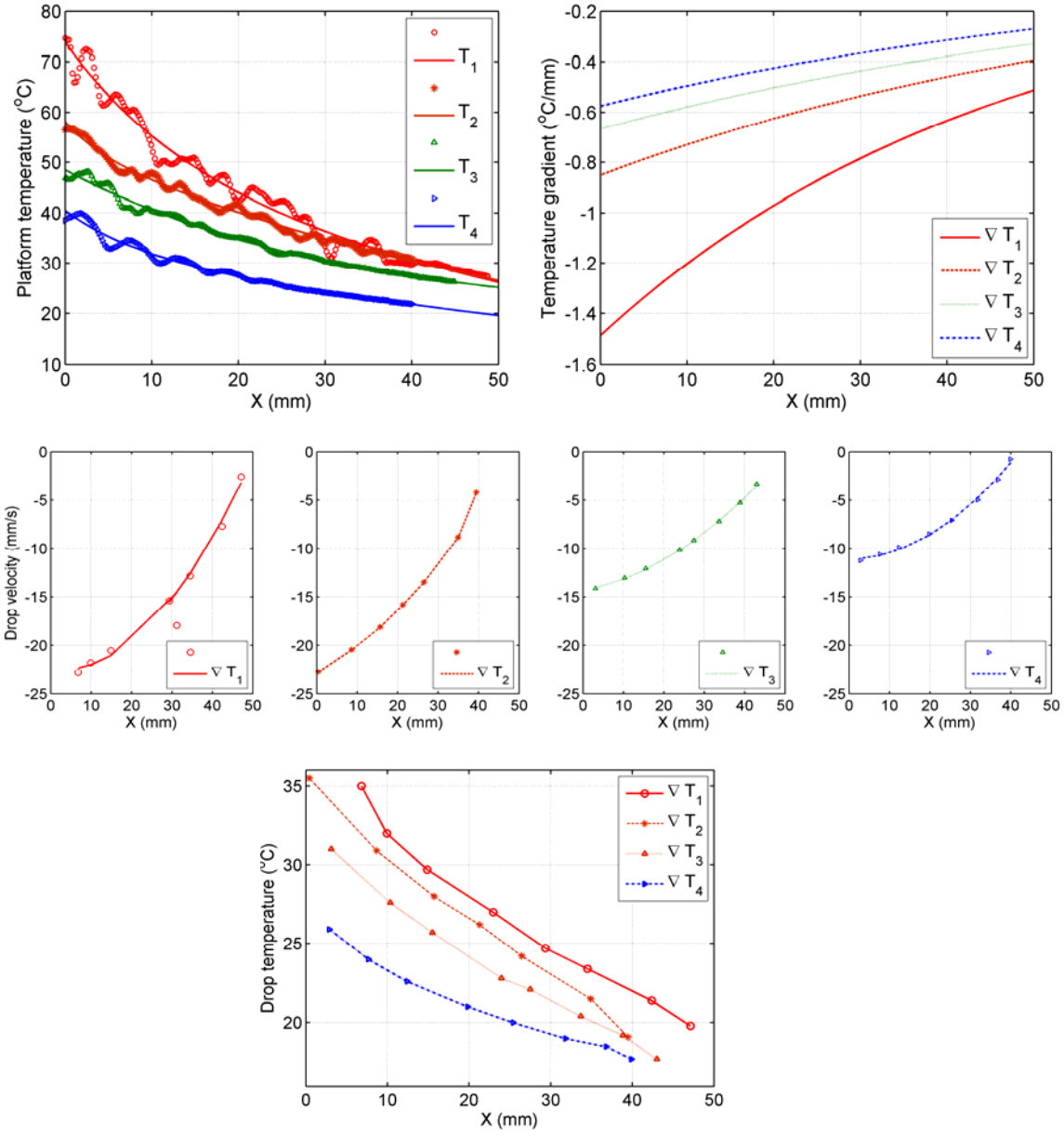

Figure 40 Steady temperature fields and the resulting thermal gradients cause spherical drops to get attracted to high temperature regions. Steeper gradient leads to higher instantaneous velocity (drop volume 14μL).

In order to investigate the effect of droplet size on thermally-induced motion of spherical droplets, various size (gauge) needles were used. It is noted that for creating spherical droplets at the air liquid interface, it is required that droplets be dispensed as free falling droplets released on to the liquid surface from a critical height. It was found by experiment that a cubic relation exists between the nozzle size of the dispensing tip and the resulting droplets, pinched off due to their own weight from the needle tip (Figure 41).

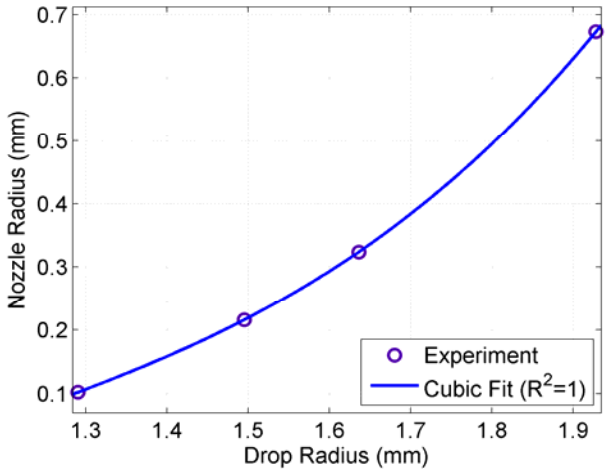

Figure 41 Relationship between the nozzle radius and the falling pendant drop radius.

Figure 42 shows the effect of droplet size on the average drift speed and the overall internal temperature increase for a given thermal gradient. Unlike in lens droplets, the average velocity and droplet size do not follow a monotonic trend. This is attributed to an apparent drag coefficient which is a function of droplet size and the relative velocity between the droplet and the underlying free surface flow.

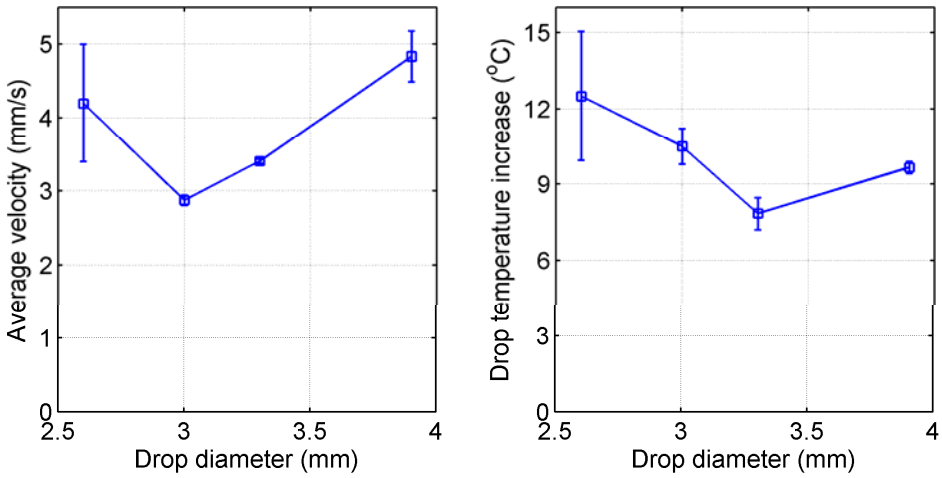

Figure 42 Effect of drop size on average drift speed and overall increase in drop temperature as it moves across the platform.

Average droplet velocity plotted against droplet size shows a minimum. Spherical droplets were dispensed on the surface using needles G27 to G16. Droplets follow the downhill surface slope towards the hottest extreme of a thermal gradient formed on the liquid platform where the free surface is most depressed. Results show a dependency between the velocity of spherical droplets and droplet size, which implies that there exists a force (drag) that is a function of droplet size in addition to gravity that pulls droplets downhill the surface slope. If the velocity were only a function of the gravitation acceleration, then variation in droplet size should not have had any effect on the thermal motion of spherical droplets.

Droplet temperature increase along the path is a function of contact time (larger average velocity corresponds to shorter contact time), effective contact area between the droplet and the surrounding liquid and droplet thermal capacity, all of which are functions of the droplet size. The overall contribution of these effects should be investigated to predict the temperature

variation within the droplet as its size changes. More details of the proposed drag mechanism is provided in the following sections where empirical results are compared to the predictions of theoretical models developed for thermally induced motion of spherical droplets.

CHAPTER 5: DISCUSSION – COMPARISON TO THEORETICAL MODELS

In chapter 2 and 3, the theoretical framework that could explain the thermal motion of lens and levitated spherical droplets at an air-liquid interface was provided. The dynamics of the thin liquid layer essentially governs the motion of the droplets [14]. It was established that due to the influence of the lateral thermal gradient, a thin liquid film undergoes two major changes: 1) a flow develops on the free surface which carries fluid in the direction of decreasing temperatures 2) the free surface deforms and forms a downhill slope towards the hottest region of the gradient, where the maximum depression of the free surface occurs. In the following subsection we explain why spherical and lens droplets move in opposite directions based on the theoretical framework. Experimental observations are characterized and compared to the predictions made by the developed models.

Model for the Motion of Lens Drops

The direction of thermocapillary motion for the lens-shaped droplets residing at the air-liquid interface of a thin film subject to a thermal gradient is in the direction of decreasing temperatures, as confirmed in earlier works [11, 13, 14, 16], i.e., droplets moved from warm towards colder regions of the platform. If the droplets were placed on solid surfaces (without a carrier liquid), the thermocapillary motion would be determined by the balance of the internal flows within the droplet (Marangoni flow) together with the change in the spreading coefficient ($S=\sigma_{carrier} - \sigma_{carrier\_drop} - \sigma_{drop}$) at the extremities of the droplet[10]. However, for droplets resting on liquid films, the overall motion is dictated by the underlying surface/interfacial driven motion of the liquid layer and the events occurring at the droplet-liquid-air triple contact line are overshadowed by the bulk flow developed in the liquid film. In other words, the lateral thermal gradient across

the length of the liquid platform is insignificant over the length scale of the droplet diameter ($d_{drop} / L_{platform} \sim 0.02$). It has been shown by order-of-magnitude analysis that although surface (interfacial) tension gradients would exist at the boundaries of droplets or bubbles suspended in a liquid subject to thermal gradients, they are too small to affect the overall translation motion appreciably. The bulk movement of fluid in the underlying layer is expected to dominate the motion of droplets compared to possible motion caused by any interfacial imbalances of forces due to dissimilar contact angle, wetting or spreading coefficient across the droplet [59]. The order of magnitude for droplet motion due to contact angle change in typical thermal gradients used in current experiments is calculated to be on the order of μm/s [60], while average translation velocities in the range of mm/s are observed for lens droplets moving on liquid layers. The observed motion of the lens droplets from hot to cold regions of the platform is explained based on the free surface velocity developed due to the thermal gradients confirmed by the physical model developed for thin liquid films. Free surface flow occurs as a result of thermal gradients that give rise to surface tension gradients across the free surface. As the fluid temperature rises, the surface (interfacial) decreases. Fluid from the hotter portions gets pulled by the fluid towards the colder regions due to stronger cohesive forces. In effect, the surface tension gradient at the surface causes an effective shear stress that eventually causes bulk motion of the fluid.

Following the thermal gradient formation, a Couette-type flow is initially formed in the quiescent liquid layer (Figure 43) and further develops into a recirculation flow due to continuity restrictions over time.

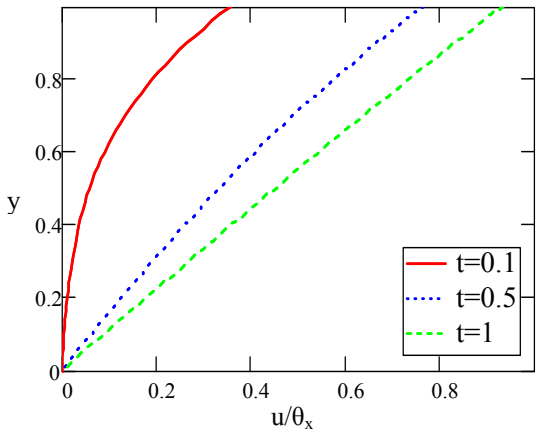

Figure 43 Initial Couette flow developed in the liquid layer following formation of the thermal gradient (y, t and u are normalized depth, time and velocity of the liquid and θ_x is the temperature gradient distribution on the free surface).

Based on the parameters (exponentially decaying temperature gradient, physical properties of water and FC 43) used in experiments, the transient evolution of the free surface velocity is shown for a typical case in (Figure 44). It is noted that time scales for Couette flow and the following recirculation flow are on the order of 1.5 and 2.8 – 7.3 seconds respectively. From the theory, it is seen that within t=0.1 (normalized time), the free surface acquires a relatively non-varying velocity that monotonically decreases away from the source of heat as a result of the exponential temperature gradient imposed on the surface.

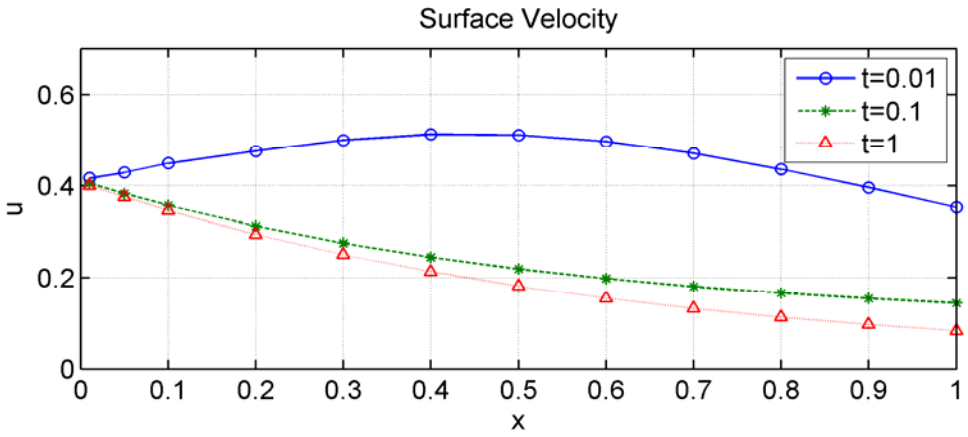

Figure 44 Velocity at the free surface at instances t=0.01, t=0.1 and t=1 (ΔT=22°C, τ=3.5s, A=0.03, $\bar{U}$ =15mm/s, Bo=2.8x10^4, Ma=2.5x10^4, Re=290

Experimental results suggest that lens droplets that are set in motion in the direction of decreasing temperatures essentially get dragged along by the surrounding fluid at the free surface. In other words, such droplets act as tracer particles that obey the free surface flow.

The numerical model is solved for the normalized temperature function measured in experiments, which follow a form of $\theta(x) = a\exp(bx)$. Lens droplets follow the trend of the surface velocity (steady state solution). It should be noted that the free surface velocity develops through a transient phase; however, considering Figure 44, the time scale elapsed for a non-varying free surface velocity is on the order of a tenth of the overall time scale (~0.2 seconds), which is significantly smaller than the time scale of the motion of the droplets across the platform. Therefore, it is valid to compare the normalized velocity of the droplets with the steady state free surface velocity. As seen in Figure 45, there exists an offset between the velocity of the free surface and the velocity of the droplet, which is larger for larger droplets (for example 2μL droplets acquire a velocity closer to the surface velocity compared to 10μL drops). The free surface velocity and the velocity of lens droplets across the platform follow forms of

exponentially decaying functions. This is expected based on the prescribed temperature distribution across the platform. Droplet velocities found through experiment were normalized by the velocity scale $\bar{U} = \left| d\sigma / dT \right| \frac{A\Delta T}{\mu}$, found by using the physical properties of fluids and temperature differentials measured in experiments.

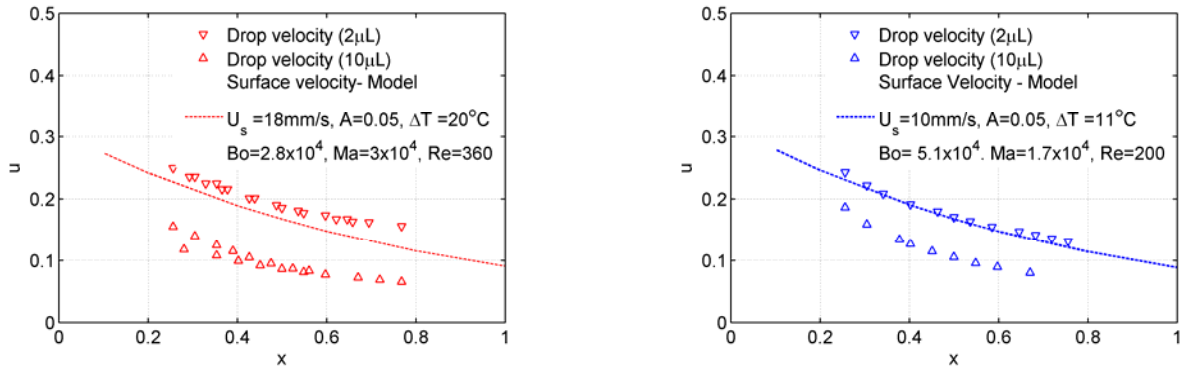

Figure 45 Droplet velocity from experiments (normalized by $\bar{U} = \left| d\sigma / dT \right| \frac{A\Delta T}{\mu}$) compared to free surface velocity calculated using the model for $d\theta / dx = e^{-1.3}$.

Model for the Motion of Spherical Droplets

In addition to the commonly observed partially submerged lens droplets, it was found that it is also possible to dispense droplets in form of levitated spheres. Interestingly, such spherical droplets migrate in the opposite direction of lens droplets, when placed on a liquid layer across which a thermal gradient is maintained; i.e. direction of increasing temperatures. The attraction of the droplets in the direction of increasing temperature is explained based on the surface slope and the effect of gravity. Thermal gradients cause surface tension gradients at the free surface, causing deformation of the free surface with a downhill slope towards the maximum temperature, where maximum depression occurs. In this sense, spherical droplets that are resting above the

interface move down the surface slope due to the pull of gravity. In addition, since the carrier liquid has lower thermal conductivity than the droplet, the droplet is essentially isothermal, ruling out the possibility that the surface tension forces at the triple contact line are responsible for droplet migration.

For spherical droplets, although the motion is against the direction of the surface flow, counter-intuitive at the outset, a simple analysis shows that spherical droplets should indeed migrate down the free surface slope due to gravity. The droplet acceleration can be attributed to the free surface slope, $H_x(x)=dH/dX = \tan(\zeta) \sim \zeta \sim \sin\zeta$ due to small slopes (ζ is the angle the free surface makes with the horizon). Droplet motion is affected by gravity and the opposing viscous drag exerted by the underlying medium: using balance of forces as $ma = -mg\sin\xi + C_D(\frac{1}{2}\rho A)V_{rel}^{\ 2}$ where a is the acceleration of droplets and considering $a.dX=V.dV,$ the differential equation governing the droplet velocity is given as follows:

$$\frac{dV}{dX} = -g.H_x\frac{1}{V} + C_0\frac{(V+V_{surf})^2}{V} \qquad \textbf{(26)}$$

where $C_0 \equiv \frac{C_D}{m}(\frac{1}{2}\rho A)$ and g is the gravitational acceleration and C_D is the drag coefficient. Equation $\frac{dV}{dX} = -g.H_x\frac{1}{V} + C_0\frac{(V+V_{surf})^2}{V}$ is normalized using length and velocity scales established in earlier sections ($v = \frac{V}{U}, x = \frac{X}{L}, h = \frac{H}{d}$):

$$\frac{dv}{dx} = -C_1 \frac{dh}{dx}\frac{1}{v} + C_2 \frac{(v + v_{surf})^2}{v}$$

(27)

The dimensionless constants are $C_1 \equiv \frac{gAL}{U^2}$ and $C_2 \equiv \frac{C_D}{m_{drop}}\left(\frac{1}{2}\rho A_{frontal}\right)L = \frac{3}{8}\frac{C_D f L}{r_{drop}}$, where f is used to define the fraction of total area of the sphere ($4\pi r^2$) exposed to the oncoming flow (*f=0 – 1)*. The effective drag coefficient $C_{D\_effective} = C_D f$ captures the effects of both the nominal drag coefficient and the frontal area exposed to the oncoming flow. Equation 27 is solved as an initial value problem using the normalized thermal fields from experiment (Figure 46) as prescribed conditions. Temperature is normalized using the following relationship:

$$\theta(x) = \frac{T(X) - T_{cold}}{T_{hot} - T_{cold}}$$
$$\frac{d\theta}{dx} = \left(\frac{L}{\Delta T}\right)\frac{dT}{dX}$$

(28)

The solution involves knowledge of the free surface slope ($\frac{dh}{dx}$) and the free surface velocity (u_{surf}), which are derived from the solution to the governing equations of thin liquid films subject to thermal gradients. Equation 27 is nondimensional and depends on constants C_1 and C_2 which represent the overall strength of the driving and opposing terms.

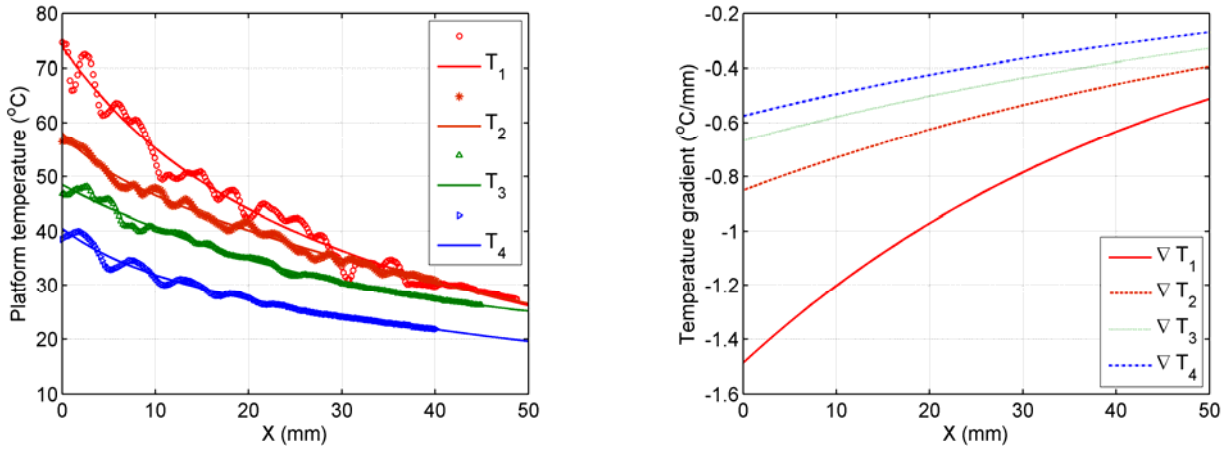

Figure 46 Experimental temperature field and corresponding thermal gradient on the liquid platform

In Figure 47, experimental results are plotted together with the solution of equation 27 using appropriate values for C_1 and C_2 as fitting parameters. Droplets experiencing steeper thermal gradients (∇T_1) gained a higher drift velocity. Larger thermal differentials cause steeper slopes on the free surface (increased gravitational pull) as well as smaller drag resistance considering the fact that the lubrication pressure buildup is directly proportional to the relative velocity between fluidic interfaces.

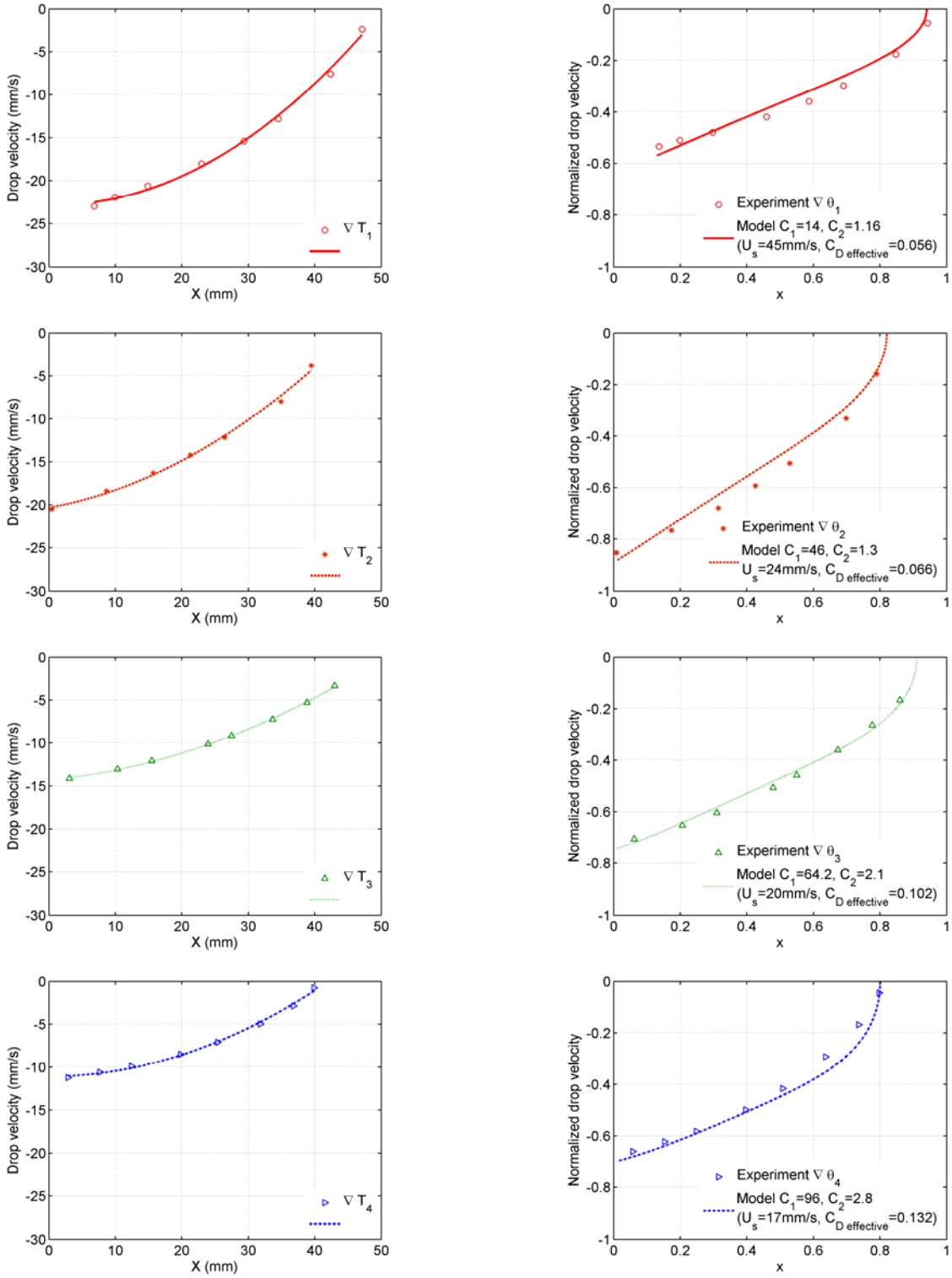

Figure 47 Drop (spherical) velocity from experiment is compared by drop velocity calculated from the proposed model (effective drag $C_{D\ effective}$ varies from 0.0566 to 0.132 for various cases)

The capability of the model in predicting details of the thermally-induced motion of spherical droplets is satisfactory. Experimental measurements of velocity for spherical droplets normalized by the thermal velocity scale collapse onto a single curve representing a family of similar curves (Figure 48).

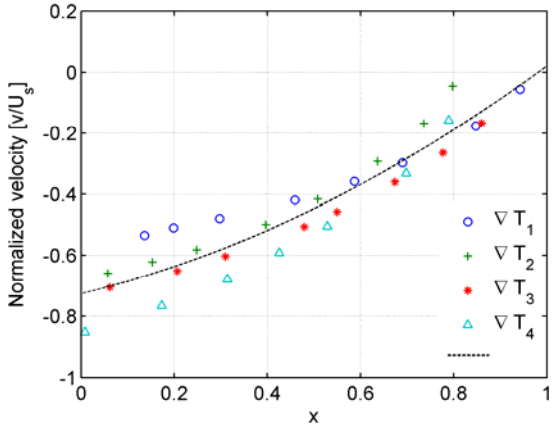

Figure 48 Thermally-induced normalized velocity of spherical droplets across various thermal gradients collapse onto a single representative curve.

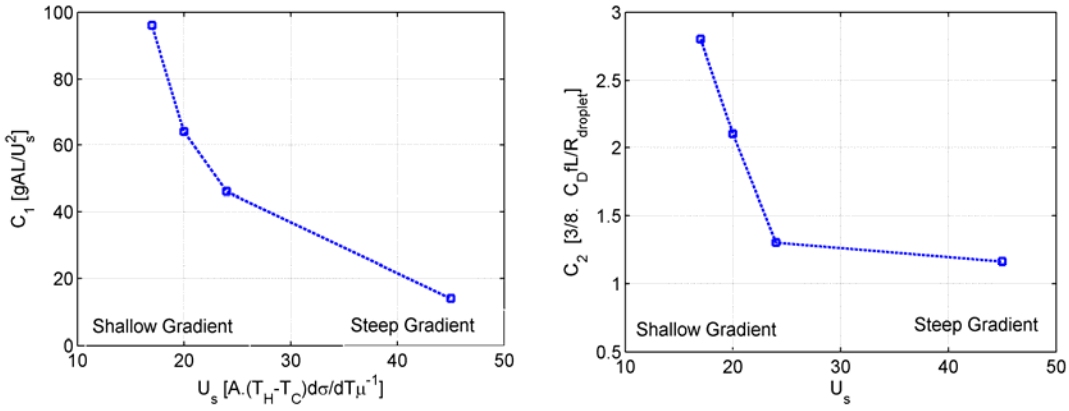

Figure 49 Variation of $C_1 = \frac{gAL}{U_s^2}$ and $C_2 = \frac{3}{8}\frac{C_D fL}{r_{drop}}$ with thermocapillary velocity scale which is proportional to the temperature differential

Figure 49 shows empirical values of the fitting parameters C_1 and C_2 as a function of the temperature differential (thermal velocity scale). A declining trend is observed for C_1 as the thermal gradient gets steeper which is expected from the definition given for $C_1 \equiv \frac{gAL}{\bar{U}^2}$ (large gradient implies larger thermal velocity). C_2 also shows a decreasing trend with increasing thermal slopes. All parameters kept constant, from the definition of $C_2 \equiv \frac{C_D}{m_{drop}}\left(\frac{1}{2}\rho A_{frontal}\right)L = \frac{3}{8}\frac{C_D f L}{r_{drop}}$, it is concluded that the drag coefficient is indeed variable and decreases with increasing temperature differentials across the platform. This is explained by using the outcomes of the levitation pressure model developed in the chapter 3. Larger thermal gradients result in larger interfacial velocities which in turn result in larger lubrication pressure buildup ($\Delta p \propto \frac{\mu U_s L_c}{\bar{h}^2}$) that reduces the overall interaction among the fluidic surfaces; hence the lower apparent drag coefficient.

The physical model for thermally-induced motion of spherical droplets suggests that the gravitational term C_1 is not affected by the size of the droplet; only the second term in equation 27 is a function of droplet size, and is used to explain the dependency of the thermal velocity of spherical droplets on droplet size. C_2 represents the resistance (drag) caused by the underlying liquid flowing in the opposite direction to the droplet and involves the parameter f which enters the definition of C_2 in the following form: $C_2 \equiv \frac{C_D}{m_{drop}}\left(\frac{1}{2}\rho A_{frontal}\right)L = \frac{3}{8}\frac{C_D f L}{r_{drop}}$. As the droplet size increases, gravity pulls it down deeper into the free surface; however, the buoyancy and surface tension forces also increase. It was found earlier that the spherical static

configuration of droplets at the air-liquid interface does not satisfy the balance of equilibrium forces due to the existence of the lubricating air film, which itself is not well characterized. Therefore, f cannot be determined, since the spherical droplet configuration is not described as an equilibrium configuration; however the empirical values from experiments provided in Figure 50, suggest that the overall drag coefficient ($C_D.f$) exhibits a peak when plotted as a function of droplet size.

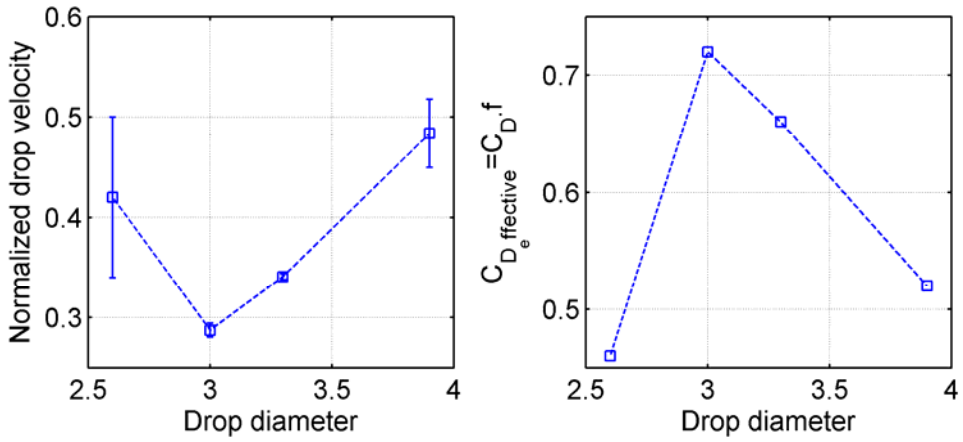

Figure 50 Normalized drop velocity from experiment (left) and corresponding effective drag coefficient used in solving the theoretical drop velocity.

In summary, it was found that the thermal motion of spherical droplets at an air-liquid interface is dependent on the magnitude of the thermal gradient as well as the droplet size. Larger thermal gradients cause larger drift velocity but at the same time cause the internal droplet temperature to increase. As such, a compromise has to be made between achieving larger drift speeds and the maximum allowable temperature fluctuation within the transported droplets. Smaller droplets experience smaller drag and in addition formation of smaller spherical droplets is possible with more flexibility as compared to larger droplets which shows the system will benefit from down scaling (miniaturization).

CHAPTER 6: DROPLET MANIPULATION PLATFORM

Based on the theory and experiments developed in this study for thermally-induced motion of droplets at the air liquid interface of a thin immiscible liquid layer, a droplet manipulation platform was proposed. There is a growing interest in droplet based systems especially for bio-chemical applications because droplets offer a self contained micro reactor environment and serve as a vehicle for material transport as well [47, 61]. A major challenge is the reliable and controllable transport of droplets. Various concepts have been proposed to address this problem. Majority of them rely on causing differentials of parameters that affect the surface (interfacial) tension of fluids resulting in bulk motion. For example, differentials of temperature [11, 13, 15, 16], chemical species (surfactant concentration) [62], electric charge [63] and magnetism have been used to manipulate droplets. Introducing chemicals and magnetic particles would contaminate the content of droplets. Similarly, electrowetting schemes are only applicable to electrically conducting liquids which limits their applications. Among thermally-actuated platforms, which mostly involve solid surfaces, there are a number of shortcomings that have not been addressed; for example: droplet evaporation, droplet pinning, contact angle hysteresis and surface contamination. In this study we replaced the solid substrate with a thin layer of a chemically inert and thermally stable liquid, Perfluorotributylamine –FC43 (3M) which serves as carrier layer for droplet transport. Perfluorocarbon emulsions, including FC-43, have been used for biomedical applications such as artificial blood and tissue preservation media. Chemical stability and biocompatibility of FC43 has been proven in earlier studies [64-66]. The liquid is clear and non-flammable with melting and boiling points of -50^{o}C and 174^{o}C, respectively. Thermal conductivity is 0.065Wm^{-1o}C^{-1}, dielectric constant is 1.9 and resistivity is 3.4 x 10^{15} ohm-cm. It is also known not to leave any residue on surfaces upon drying. In this stud, FC-43

serves as the buffer liquid on the proposed platform on which droplets are dispensed. Embedded microheaters were used to generate the necessary thermal maps (gradients). Spherical droplets can be controlled conveniently because they always get attracted to the nearest hot spot, while lens droplets would be repelled away from the source of heat in arbitrary directions on the surface, which cannot be predicted accurately. In addition, spherical droplets can be trapped and released on demand. Methods for creating stable spherical droplets have been described in chapter 2.

Fabrication of Microheaters

A 500nm thick layer of SiO_2 was thermally grown on a 3-inch silicon wafer as an insulator layer. A layer of Titanium (1000nm) was then deposited using electron-beam evaporation to serve as the heating element material. Heater elements were formed by photolithography by completing the following procedure: HMDS (hexamethyldisilizane) was spin-coated (4000rpm for 60 seconds) for improved adhesion of photoresist on the wafer. Positive photoresist (Shipley S1813) was then spin-coated (3000 rpm for 30 seconds). The wafer was soft-baked for 3 minutes on 105˚C hotplate. Photolithography was continued by exposing the wafer to form the heater patterns (G-line, energy dose=13mW/cm^2 for 8.8 seconds using EVG-620 Aligner system). The patterns were developed using CD-26 (Microposit MF). Features were developed in a little more than 1 minute. Post development bake was carried out for 12 minutes at 125˚C. The unprotected Titanium was etched away using an etchant solution (20 H_2O : 1 H_2O_2 : 1 HF - 49%) at room temperature. Etching was completed (visible inspection) in a minute and 40 seconds. After checking the features under the microscope for sharp edges and other feature qualities, the

protective photoresist was stripped off using acetone. The wafer was rinsed and blow dried using an air gun.

Device Packaging

The microfabricated heaters were interfaced with external wiring using thin platinum conducting strips. An O ring (n-Buna square cross section, McMaster Carr) was press-glued to fix the contact pads and create a sealed area for the carrier liquid pool to be formed. Electrical connections were made between the platinum strips and external wiring using terminals (Figure 51). The resistance measured across contact pads and heater elements were on the order of 12Ω and 90Ω, respectively.

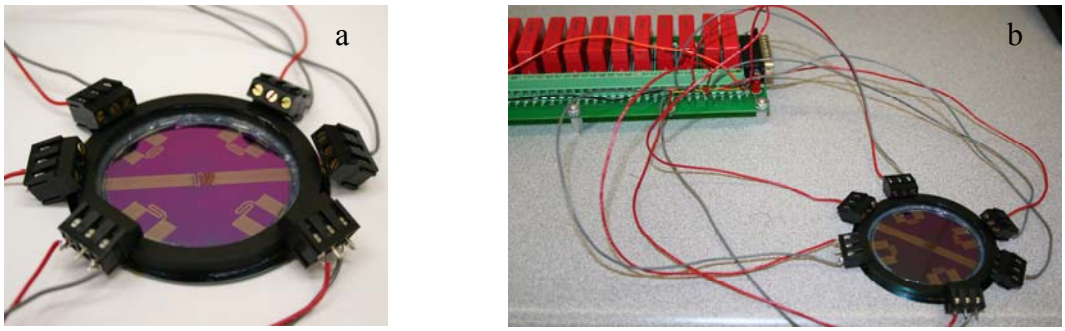

Figure 51 Device at various fabrication stages

Device Control Unit

The control unit consists of hardware and software. The hardware consists of a data acquisition device (U12, LabJack Corp. CO), a relay board (RB16, LabJack Corp. CO) to handle high current/voltage and 5 output modules (70M-ODC5, Grayhill Inc. IL) that are interfaced with the microheaters (Figure 52a). The graphical user interface is designed such that the location of the

droplet can be controlled by scrolling the mouse pointer on the computer screen over the designated heaters (circular icons Figure 52b). Based on the live infrared thermal imaging window, the user can move the droplet on a desired path on the platform or trap it in one location.

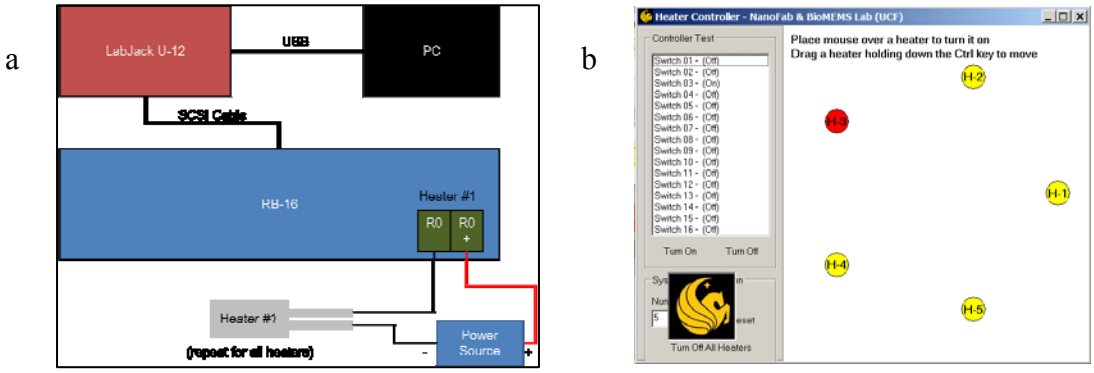

Figure 52 Schematic of the control unit hardware (a) and software interface (b) [1]

Droplet Manipulation Platform Operation

In order to demonstrate the performance of the droplet manipulation platform, spherical droplets were dispensed on the liquid platform (Droplet Manipulation Platform Video). Droplets get attracted to the nearest hot spot (heater element turned ON by user). The platform is in contact with a metal block serving as a heat sink, which causes the heat generated from the microheaters to be dissipated quickly. Upon the formation of another hotspot, the drop can be moved to another location on a path that corresponds to the maximum thermal gradient (Figure 53). Each heater on the platform requires about 8W power input in continuous mode operation. This power requirement is relatively large compared to the range of typical power consumption rates in

1 The technical support of Dr. Sungmin Kim (Department of Polymer and Fiber System Engineering Chonnam National University, Korea) is acknowledged and greatly appreciated

MEMS devices. The power requirements can be reduced by optimizing the design parameters, such as the spacing and the design of heaters. Average thermal gradient on the order of 0.6°C/mm caused spherical droplets to acquire an average velocity on the order of 10mm/s.

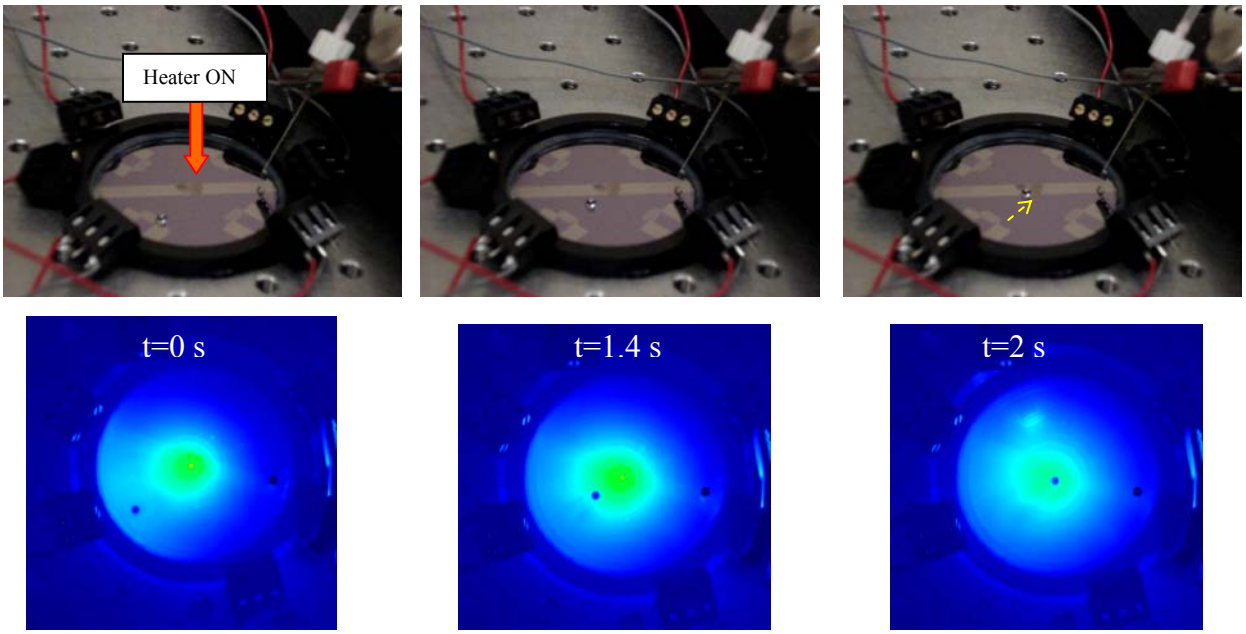

Figure 53 Snapshots of infrared imaging showing a spherical drop move from towards the hot spot at the center of the platform;

Close to a hundred fold increase in average speed is observed for droplet transport on the proposed liquid platform as compared to previous studies that used solid substrates [11, 13]. In addition, we found that although lens droplets can be set into motion using thermal gradients, but lens droplets could move in almost any arbitrary direction away from the source of heat, the motion and location of lens droplets cannot be predicted and controlled easily. We proposed spherical droplets, which always get attracted to hotspots and are held until another thermal map is generated on the surface. In this sense, the position and direction of motion for droplet transportation is very well-controlled. Reliable droplet transport with high degree of control is

demonstrated in this study for the first time[17]. Manipulating droplets on a liquid platform using thermal gradients offers many advantages. The following comparison provides some of the benefits of using the concept proposed in this study:

- In electrowetting-based actuation schemes, only droplets that are of some electrically conducting liquid can be transported. Pollack et al. demonstrated motion of 0.7 – 1μL droplets by applying voltage (40-80V) to electrodes on the platform, achieving an average velocity of 30 mm/s. In this study the same order of transport speed is achieved, whereas the requirement for having ions in the liquid drops is not necessary (100mM KCl solution was used in the mentioned study) [63, 67].
- Droplet pinning and sample loss due to evaporation and trailing streaks, chemical contamination, hysteresis effects and irreversibility of motion do not occur in the proposed scheme; while such drawbacks have been reported for platforms that are based on solid substrates [10, 11, 13].
- Furthermore, because the droplets are separated from the heating elements by an inert liquid layer, the inner contents of the droplets are not directly exposed to excessive thermal loading, as they might be on solid platforms. High thermal fluctuation is not favorable when temperature-sensitive bio-chemical species are transported by the droplets.

CHAPTER 7: CONCLUSION

In this work, droplet motion on the free surface of a thin liquid layer, caused by lateral thermal gradients, was investigated. A novel mechanism for thermally-induced motion of droplets on thin liquid films was discovered. While normally occurring lens-shaped droplets (e.g. water on oil), move in the direction of decreasing temperatures, as established by earlier studies, in this study, we showed that it is possible to form levitated spherical droplets on the free surface of liquids. For such spherical droplets, thermocapillary motion is in exactly the opposite direction compared to lens droplets i.e. direction of increasing temperatures. It was found that the motion of interfacial droplets is primarily governed by the dynamics of the underlying liquid film. When a thermal gradient is maintained across a thin liquid platform, two key phenomena occur: (1) the free surface gets deformed such that the high temperature regions become depressed and (2) a flow develops on the free surface that carries fluid from the hot end towards the cold side of the thermal gradient. These two findings were used to explain the dual behavior of droplets resting at the air-liquid interface of an immiscible liquid, subject to a thermal gradient. Partially submerged lens droplets get dragged along with the underlying liquid, following the free surface flow, which is from hot to cold; hence the motion of such droplets in the direction of decreasing temperatures. On the other hand, spherical droplets, which rest above the surface, get attracted to the hotter regions (maximum depression of the free surface) due to the effect of gravity and the downhill surface slope, despite the opposing drag from the free surface flow.

Based on the dynamics of thin liquid films subject to thermal gradients, theoretical models were developed to explain the thermally-induced motion of interfacial droplets. Results from experiments and those predicted by the models are in good agreement. It was found that the drift

velocity for both lens and spherical droplets increases with the increase in the magnitude of the thermal gradient. While larger lens droplets move at relatively lower velocities as compared to smaller ones when exposed to a given thermal gradient, a monotonic (increasing/decreasing) trend was not seen for the drift velocity of spherical droplets as a function of droplet size. This is attributed to the overall drag coefficient, which is dependent on the relative interfacial velocity between the droplets and the underlying liquid and also the effective exposed area of the droplet to the oncoming flow.

As mentioned earlier, the configuration (shape) droplets assume at the air-liquid interface determines the direction of thermocapillary motion for the droplets. In order to study the formation of lens and spherical droplets at the air-liquid interface, impact of water droplets on the surface of Perfluorotributylamine (FC43) liquid was studied experimentally and theoretically. The requirement for free-falling droplets on immiscible liquid surfaces for sustaining the impact and eventually forming a spherical configuration was described in terms of droplet size and the critical release heights. Balance of forces (buoyancy, gravity and surface tension) predicts the lens configuration as the only equilibrium static condition. Existence of the spherical state is explained based on the concept of *mechanically enforced static configurations,* which can occur in the presence of an external non-equilibrium agent in the system that compensates for the imbalance of equilibrium forces.

Based on the physical principles explored in this study, a droplet manipulation platform was designed and fabricated using conventional microfabrication techniques. Typical thermal gradients in the range of 0.3 – 0.7˚C/mm resulted in average velocities in the range of 5 –

12mm/s for spherical droplets with a maximum speed of 30mm/s. For gradients of 0.15 – 0.3˚C/mm, lens droplets moved at an average speed of 2 – 4mm/s. For normal operating conditions, maximum temperature rise in droplets was limited to a few degrees Celsius, which is a critical requirement in most bio-chemical applications where materials and processes are highly sensitive to temperature fluctuations. Perfluorotributylamine (FC43) has been proven to be chemically inert and thermally stable and is used as the carrier liquid in the proposed platform considering its known safety and biocompatibility. The experiments of droplet manipulation on liquid platforms show favorable scaling characteristics; in other words better performance is observed for smaller droplets (higher speed and lower thermal fluctuation), which shows that the proposed droplet transportation mechanism is compatible for miniaturized droplet-based platforms. While the proposed platform provides a reliable means for droplet transport for lab-on-chips and other applied applications, it could also be used to study the dynamics of interfacial fluidic systems from a fundamental science perspective.

Directions for Future Work

A comprehensive approach was taken in this study to address both, the theoretical and applied aspects of thermally-induced motion of droplets on liquid films; however, the following is proposed for further investigation in future works:

- The dependency of thermocapillary drift of spherical droplets on size needs to be studied in more detail. The underlying free surface flow opposes the motion of spherical droplets towards the higher-temperature end of the thermal gradient, giving rise to an effective drag. Levitated spherical droplets have attributed to a thin air cushion between the droplet

and the carrier liquid. The thin air layer was studied in the context of lubrication theory. It is necessary to investigate the nature of this drag mechanism given the existence of such an air gap which leads to non-equilibrium conditions. For example the dependency of the drag coefficient on the relative velocity between fluid interfaces and droplet size can provide more details on the dynamics of thermal motion.

- In this study one pair of droplet – carrier liquid was studied (water – FC43). The choice of various combinations of liquids for the droplet and the carrier film, the effect of physical properties (surface tension, viscosity, density and thermal conductivity) on thermocapillary motion of interfacial droplets could be investigated.
- Spherical droplets get attracted to hot spots on the liquid platform while lens droplets get repelled away from the source of heat, often in a direction that cannot be predicted. As such, spherical droplets offer better controllability compared to lens droplets; however they are usually unstable on the liquid surface and have a tendency to collapse into the lens configuration. A stability analysis is needed to identify the parameters that can prevent collapse and prolong the life time of spherical droplets.
- The performance of the first generation of the droplet manipulation platform was demonstrated successfully with a high level of reliability and control; however there is room for achieving faster response times, better thermal management and less power usage. For example, in the first generation prototype, there are only five heaters (one at the center and 4 at the periphery) on the platform that are far spaced (>3cm). Since droplets move only if they sense the thermal gradient, it is expected that when heaters are spaced far apart, it takes a longer time for the transient thermal gradients to propagate along the platform and reach the droplets and cause motion. By creating an array of

closely spaced heaters and implement a closed-loop feedback control mechanism, the response time of the system can be improved significantly.

- In this study, manipulation of a single droplet was shown using the proposed concept. However, for most applications (e.g. lab on chip), standard operations such as mixing, titration, droplet trapping etc, are needed which require control and manipulation of multiple droplets. For example two or more droplets containing different reagents should merge for a reaction to follow and the resulting combined droplet containing the products of the reaction should be transported to another location on the platform for further processing (optical diagnostics). Figure 54 and Figure 55 demonstrate transport and merger of multiple droplets.

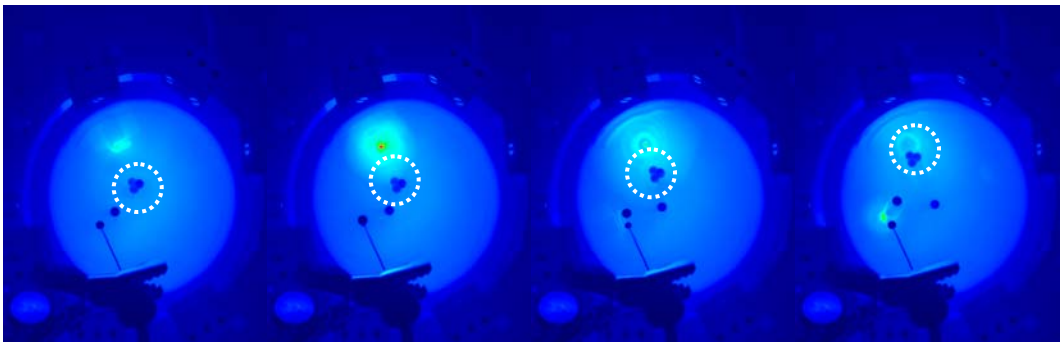

Figure 54 Conglomerate of three drops is being transported to a hot spot.

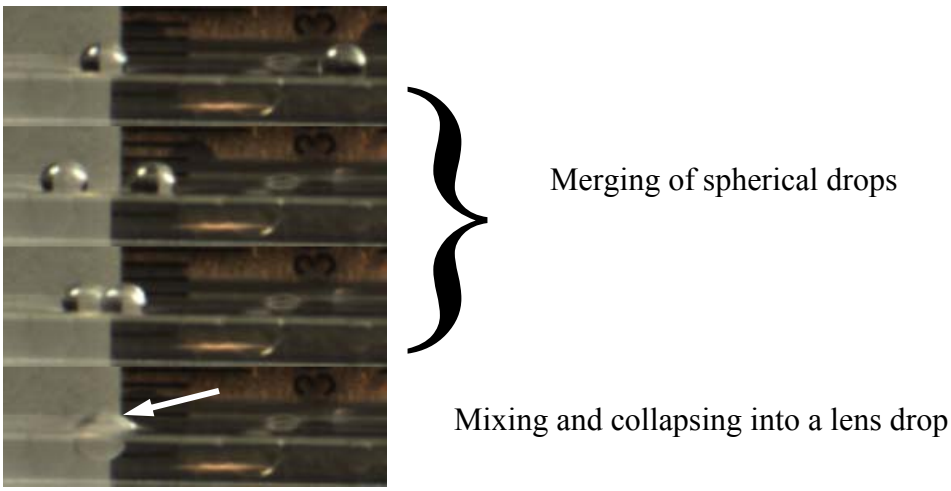

Figure 55 Merger of two spherical droplets and formation of a lens drop

Detailed theoretical models are needed to increase speed of transport on the platform, optimize control mechanisms and add extra functionality to the current droplet manipulation platform.

The droplet manipulation platform proposed in this study is robust and can be used without special requirements or restrictions unlike other transport mechanism such as electrowetting that requires transported liquids to be electrically conductive. Droplet pinning and evaporation, chemical contamination and extremely slow speeds associated with using solid substrates have been avoided by replacing the solid surface with a chemically inert film of liquid.

APPENDIX : DERIVATION OF THE NORMALIZED NAVIER STOKES EQUATIONS FOR THIN LIQUID FILMS

Continuity:

$$\partial U/\partial X + \partial V/\partial Y = 0$$

$$scaling: x = \frac{X}{L}, y = \frac{Y}{d}, A = \frac{d}{L}, u = \frac{U}{\bar{U}}, v = \frac{V}{\bar{U}.A}, t = \frac{\tau}{\tilde{\tau}}$$

Where $\bar{U}$ is the velocity scale, A is the aspect ratio and $\tilde{\tau}$ is the appropriate time scale.

Dividing by the velocity scale and substitution:

$$\frac{\partial\left(U/\bar{U}\right)\bar{U}}{\partial\left(X/L\right)L} + \frac{\partial\left(V/\bar{U}.A\right).(\bar{U}.A)}{\partial\left(Y/d\right)d} = 0$$

$$\boxed{\partial u/\partial x + \partial v/\partial y = 0}$$

X Momentum:

$$\frac{\partial U}{\partial \tau} + U\frac{\partial U}{\partial X} + V\frac{\partial V}{\partial Y} = -\left(\frac{1}{\rho}\right)\frac{\partial P}{\partial X} + \upsilon\frac{\partial^2 U}{\partial X^2} + \upsilon\frac{\partial^2 U}{\partial Y^2}$$

Each term can be made dimension less as follows:

$$\frac{\partial U}{\partial \tau}=\frac{\partial\left(U/\breve{U}\right)\breve{U}}{\partial\left(\tau/\tilde{\tau}\right)\tilde{\tau}}\xrightarrow{substitute}\frac{\partial u}{\partial t}\left(\breve{U}/\tilde{\tau}\right)$$

$$U\frac{\partial U}{\partial X}=\breve{U}\left(U/\breve{U}\right)\frac{\partial\left(U/\breve{U}\right)\breve{U}}{\partial\left(X/L\right)L}\xrightarrow{substitute}u\frac{\partial u}{\partial x}\left(\breve{U}^2/L\right)$$

$$V\frac{\partial U}{\partial Y}=\left(\breve{U}.A\right)\left(V/\breve{U}.A\right)\frac{\partial\left(U/\breve{U}\right)\breve{U}}{\partial\left(Y/d\right)d}\xrightarrow[simplify]{substitute}v\frac{\partial u}{\partial y}\left(\breve{U}^2/L\right)$$

Pressure is scale by *p* as follows:

$p=\left[P-P_{atm}-\rho g\left(H-Y\right)\right].\left(\mu\breve{U}L/d^2\right)^{-1}$, then the pressure gradient term is:

$$-\frac{1}{\rho}\frac{\partial P}{\partial X}=-\frac{1}{\rho}\left(\mu\breve{U}L/d^2\right)\frac{\partial p}{\partial\left(X/L\right)L}-\frac{1}{\rho}\left(\rho g\frac{\partial\left(H/d\right)d}{\partial\left(X/L\right)L}\right)\xrightarrow{\partial P_{atm}/\partial x=0}$$

$$=-\upsilon\frac{\partial p}{\partial x}\left(\breve{U}/d^2\right)-gA\frac{\partial h}{\partial x}$$

H is the free surface height and is normalized by d ($h=\frac{H}{d}$);

$$\upsilon\frac{\partial^2 U}{\partial X^2}=\upsilon\frac{\partial}{\partial\left(X/L\right)L}\left(\frac{\partial\left(U/\breve{U}\right)\breve{U}}{\partial\left(X/L\right)L}\right)\xrightarrow{substitute}\upsilon\frac{\partial^2 u}{\partial x^2}\left(\breve{U}/L^2\right)$$

$$\upsilon\frac{\partial^2 U}{\partial Y^2}=\upsilon\frac{\partial}{\partial\left(Y/d\right)d}\left(\frac{\partial\left(U/\breve{U}\right)\breve{U}}{\partial\left(Y/d\right)d}\right)\xrightarrow{substitute}\upsilon\frac{\partial^2 u}{\partial y^2}\left(\breve{U}/d^2\right)$$

Adding all terms leads to the following expression for the X momentum equation:

$$\left(\breve{U}/\tilde{\tau}\right)\frac{\partial u}{\partial t}+\left(\breve{U}^2/L\right)\left(u\frac{\partial u}{\partial x}+v\frac{\partial u}{\partial y}\right)=-\upsilon\left(\breve{U}/d^2\right)\frac{\partial p}{\partial x}-gA\frac{\partial h}{\partial x}+\upsilon\left(\breve{U}/L^2\right)\frac{\partial^2 u}{\partial x^2}+\upsilon\left(\breve{U}/d^2\right)\frac{\partial^2 u}{\partial y^2}$$

By dividing by $\breve{U}$ and multiplying by d^2/υ and considering the following

$$\mathrm{Re}=\frac{\breve{U}L}{\upsilon}$$

$$Bo=\rho gL^2\left\{\left|\frac{\partial\sigma}{\partial T}\right|.(T_H-T_C)\right\}^{-1}\xrightarrow{\breve{U}=\frac{\partial\sigma}{\partial T}A.(T_H-T_C)\mu^{-1}}Bo=\frac{\rho gL^2}{\breve{U}\mu}A$$

The momentum equation is given in the following form:

$$\left(d^2/\upsilon\tilde{\tau}\right)\frac{\partial u}{\partial t}+\mathrm{Re}.A^2\left(u\frac{\partial u}{\partial x}+v\frac{\partial u}{\partial y}\right)=-\frac{\partial p}{\partial x}-Bo.A^2.\frac{\partial h}{\partial x}+A\frac{\partial^2 u}{\partial x^2}+\frac{\partial^2 u}{\partial y^2}$$

Y Momentum:

$$\frac{\partial V}{\partial \tau}+U\frac{\partial V}{\partial X}+V\frac{\partial V}{\partial Y}=-\frac{1}{\rho}\frac{\partial P}{\partial Y}+\upsilon\frac{\partial^2 V}{\partial X^2}+\upsilon\frac{\partial^2 V}{\partial Y^2}-g$$

Non dimensionalization of each term is as follows:

$$\frac{\partial V}{\partial \tau}=\frac{\partial\left(V/\cancel{U}A\right)\cancel{U}A}{\partial\left(\tau/\tilde{\tau}\right)}=\left(\cancel{U}A/\tilde{\tau}\right)\frac{\partial v}{\partial t}$$

$$U\frac{\partial V}{\partial X}=\left(U/\cancel{U}\right)\cancel{U}\frac{\partial\left(V/\cancel{U}A\right)\cancel{U}A}{\partial\left(X/L\right)L}=\left(\cancel{U}^2A/L\right)u\frac{\partial v}{\partial x}$$

$$V\frac{\partial V}{\partial Y}=\left(V/\cancel{U}A\right)\cancel{U}A\frac{\partial\left(V/\cancel{U}A\right)\cancel{U}A}{\partial\left(Y/d\right)d}=\left(\cancel{U}^2A^2/d\right)v\frac{\partial v}{\partial y}$$

$$p=[P-P_{atm}-\rho g(H-Y)]\left(\frac{\mu\cancel{U}L}{d^2}\right)^{-1}$$

$$\longrightarrow P=p\left(\frac{\mu\cancel{U}L}{d^2}\right)+P_{atm}+\rho g(H-Y)$$

$$-\frac{1}{\rho}\frac{\partial P}{\partial Y}=-\frac{1}{\rho}\left(\frac{\mu\cancel{U}L}{d^2}\right)\frac{\partial p}{\partial\left(Y/d\right)d}+\frac{\partial P_{atm}/}{\cancel{\partial Y}}+(-\frac{1}{\rho})\rho g\frac{\partial\left(H/d\right)d}{\partial\left(Y/d\right)d}-(-\frac{1}{\rho})\rho g\frac{\partial(Y)}{\partial Y}$$

$$=-\frac{1}{\rho d}\left(\frac{\mu\cancel{U}L}{d^2}\right)\frac{\partial p}{\partial y}-g\frac{\partial h}{\partial y}+g$$

$$\upsilon\frac{\partial^2 V}{\partial X^2}=\upsilon\frac{\partial}{\partial\left(X/L\right)L}\left(\frac{\partial\left(V/\bar{U}A\right)\bar{U}A}{\partial\left(X/L\right)L}\right)=\upsilon\left(\bar{U}A/L^2\right)\frac{\partial^2 v}{\partial x^2}$$

$$\upsilon\frac{\partial^2 V}{\partial Y^2}=\upsilon\frac{\partial}{\partial\left(Y/d\right)d}\left(\frac{\partial\left(V/\bar{U}A\right)\bar{U}A}{\partial\left(Y/d\right)d}\right)=\upsilon\left(\bar{U}A/d^2\right)\frac{\partial^2 v}{\partial y^2}$$

$$-g=-g$$

Adding the terms gives:

$$\left(\bar{U}A/\tilde{\tau}\right)\frac{\partial v}{\partial t}+\left(\bar{U}^2A/L\right)u\frac{\partial v}{\partial x}+\left(\bar{U}^2A^2/d\right)u\frac{\partial v}{\partial x}=$$

$$-\frac{1}{\rho d}\left(\frac{\mu\bar{U}L}{Ad^2}\right)\frac{\partial p}{\partial y}-g\frac{\partial h}{\partial y}+\cancel{g}+\upsilon\left(\bar{U}^2A/L^2\right)\frac{\partial^2 v}{\partial x^2}+\upsilon\left(\bar{U}^2A/d^2\right)\frac{\partial^2 v}{\partial y^2}-\cancel{g}$$

By multiplying all the terms by $\left(d^2A/\upsilon U\right)$ the following expression is found:

$$\left(d^2A^2/\upsilon\tilde{\tau}\right)\frac{\partial v}{\partial t}+\mathrm{Re}.A^4\left(u\frac{\partial v}{\partial x}+v\frac{\partial v}{\partial y}\right)=-\frac{\partial p}{\partial y}-g\frac{\partial h}{\partial y}+A^4\frac{\partial^2 v}{\partial x^2}+A^2\frac{\partial^2 v}{\partial y^2}$$

The term $g\dfrac{\partial h}{\partial y}$ can be treated with regards to expansion; the liquid layer may not expand in the lengthwise direction and change in volume is only due to change in height:

$$d(vol)=\frac{\partial H}{\partial Y}+\cancel{\frac{\partial L}{\partial X}}=\frac{\partial h}{\partial y}$$

β is the volumetric coefficient of thermal expansion:

$$d(vol) = \beta(T - T_C) \xrightarrow[\theta = \frac{T - T_C}{T_H - T_C}]{\times \frac{T_H - T_C}{T_H - T_C}} \beta\left(T_H - T_C\right)\theta$$

$g\dfrac{\partial h}{\partial y}$ is given as follows:

$$g\frac{\partial h}{\partial y}\left(d^2 A \big/ \upsilon U\right) \xrightarrow{Bo = \frac{gL^2 A}{U\upsilon}} Bo.A^2\beta\left(T_H - T_C\right)\theta$$

Y direction momentum is given in the following form:

$$\left(d^2 A^2 \big/ \upsilon\tau\right)\frac{\partial v}{\partial t} + \mathrm{Re}.A^4\left(u\frac{\partial v}{\partial x} + v\frac{\partial v}{\partial y}\right) = -\frac{\partial p}{\partial y} + Bo.A^2\beta\left(T_H - T_C\right)\theta + A^4\frac{\partial^2 v}{\partial x^2} + A^2\frac{\partial^2 v}{\partial y^2}$$

Energy Equation:

$$\frac{\partial T}{\partial \tau} + U\frac{\partial T}{\partial X} + V\frac{\partial T}{\partial Y} = \alpha\left(\frac{\partial^2 T}{\partial X^2} + \frac{\partial^2 T}{\partial Y^2}\right)$$

Change of variables:

$$\theta = \frac{T - T_C}{T_H - T_C} \longrightarrow dT = (T_H - T_C)d\theta$$

Note: since all terms contain first order "T", the coefficient T_H-T_C cancels out; dimensional analysis of each term is as follows:

$$\frac{\partial T}{\partial \tau} = \frac{\partial \theta}{\partial\left(\tau/\tilde{\tau}\right)\tilde{\tau}} = \left(1/\tilde{\tau}\right)\frac{\partial \theta}{\partial \tau}$$

$$U\frac{\partial T}{\partial X} = \left(U/\tilde{U}\right)\tilde{U}\frac{\partial \theta}{\partial\left(X/L\right)L} = \left(\tilde{U}/L\right)u\frac{\partial \theta}{\partial x}$$

$$V\frac{\partial T}{\partial Y} = \left(V/\tilde{U}A\right)\tilde{U}A\frac{\partial \theta}{\partial\left(Y/d\right)d} = \left(\tilde{U}/L\right)v\frac{\partial \theta}{\partial y}$$

$$\alpha\frac{\partial^2 T}{\partial X^2} = \alpha\frac{\partial}{\partial\left(X/L\right)L}\left(\frac{\partial \theta}{\partial\left(X/L\right)L}\right) = \left(\alpha/L^2\right)\frac{\partial^2 \theta}{\partial x^2}$$

$$\alpha\frac{\partial^2 T}{\partial Y^2} = \alpha\frac{\partial}{\partial\left(Y/d\right)d}\left(\frac{\partial \theta}{\partial\left(Y/d\right)d}\right) = \left(\alpha/d^2\right)\frac{\partial^2 \theta}{\partial y^2}$$

By multiplying by $\left(d^2\,\mathrm{Pr}/\upsilon\right)$ and substituting for appropriate considering Ma=Re.Pr, terms the dimension less equation is in the following form:

$$\boxed{\left(d^2\,\mathrm{Pr}/\upsilon\tilde{\tau}\right)\frac{\partial \theta}{\partial t} + A^2.Ma\left(u\frac{\partial \theta}{\partial x} + v\frac{\partial \theta}{\partial y}\right) = A^2\frac{\partial^2 \theta}{\partial x^2} + \frac{\partial^2 \theta}{\partial y^2}}$$

Initial and boundary conditions:

$$\tau = 0 : U = 0, V = 0, T = T_C, H = d;$$
$$\xrightarrow{non-\dim} t = 0 : u = 0, v = 0, \theta = 0, h = 1$$

Bottom wall:

$$Y = 0 : U = 0, V = 0, T = T_C$$
$$\xrightarrow{non-\dim} y = 0 : u = 0, v = 0, \theta = 0$$

On the free surface, i) viscous stress is balance by the surface tension gradient, ii) pressure is due to atmosphere, normal stress and the surface curvature, iii) temperature is as prescribed:

$$Y = 0:$$
$$\mu\left(\frac{\partial U}{\partial N} + \frac{\partial V}{\partial S}\right) = \frac{\partial \sigma}{\partial S},$$
$$P = P_{atm} + 2\mu\frac{\partial V}{\partial N} - \frac{\sigma}{R},$$
$$T = T_{surf}\left(X, \tau\right)$$

i) Shear stress:

$$\mu\left(\frac{\partial U}{\partial N} + \frac{\partial V}{\partial S}\right) \equiv \mu\left(\frac{\partial U}{\partial Y} + \frac{\partial V}{\partial X}\right) = \mu\left(\frac{\partial\left(U/\hat{U}\right)\hat{U}}{\partial\left(Y/d\right)d} + \frac{\partial\left(V/\hat{U}A\right)\hat{U}A}{\partial\left(X/L\right)L}\right) = \mu\left(\hat{U}/d\right)\left(\frac{\partial u}{\partial y} + \frac{\partial v}{\partial x}\right)$$
$$= \frac{\partial \sigma}{\partial S} \equiv \frac{\partial \sigma}{\partial X} = -\left|\frac{\partial \sigma}{\partial T}\right|\frac{\partial T}{\partial\left(X/L\right)L} = -\left|\frac{\partial \sigma}{\partial T}\right|\frac{(T_H - T_C)}{L}\frac{\partial \theta}{\partial x}$$
$$\rightarrow \mu\left(\hat{U}/d\right)\left(\frac{\partial u}{\partial y} + \frac{\partial v}{\partial x}\right) = -\left|\frac{\partial \sigma}{\partial T}\right|\frac{(T_H - T_C)}{L}\frac{\partial \theta}{\partial x} \xrightarrow{\hat{U} = \left|\partial\sigma/\partial T\right|(T_H - T_C)\mu^{-1}}$$

$$\boxed{\frac{\partial u}{\partial y} + \frac{\partial \theta}{\partial x} = 0}$$

ii) Pressure:

Since, there is no normal component of velocity at the free surface therefore;

$$P = P_{atm} + \cancel{2\mu\frac{\partial V}{\partial N}} - \frac{\sigma}{R}$$

p on the surface is given as:

$$p = \frac{[P - P_{atm} - \rho g \cancel{(H - Y)_{@\,surface:Y=H}}]}{\left(\mu \bar{U} L / d^2\right)}$$

$$\rightarrow P - P_{atm} = p\left(\mu \bar{U} L / d^2\right) = -\frac{\sigma}{R_{curvature}} = -\sigma\left(\frac{\frac{\partial^2 H}{\partial X^2}}{\left[1+\left(\frac{\partial H}{\partial X}\right)^2\right]^{3/2}}\right) = -\sigma\left(d/L^2\right)\left(\frac{\frac{\partial^2 h}{\partial x^2}}{\left[1+A^2\left(\frac{\partial h}{\partial x}\right)^2\right]^{3/2}}\right)$$

$$p = -\sigma\left(\frac{d^2}{\mu \bar{U} L}\right)\left(d/L^2\right)\left[\frac{\frac{\partial^2 h}{\partial x^2}}{\left(1+A^2\left(\frac{\partial h}{\partial x}\right)^2\right)^{3/2}}\right] \xrightarrow{\bar{U}=\left|\frac{\partial \sigma}{\partial T}\right| A (T_H - T_C)\mu^{-1}}$$

$$\boxed{p = -\sigma A^2\left[\left|\frac{\partial \sigma}{\partial T}\right|(T_H - T_C)\right]^{-1} \cdot \left(\frac{\frac{\partial^2 h}{\partial x^2}}{\left(1+A^2\left(\frac{\partial h}{\partial x}\right)^2\right)^{3/2}}\right)}$$

iii) Prescribed temperature:

$$\theta_{surface} = fn(x,t)$$

Kinematic Condition – Governing equation for the free surface profile:

In addition to three conditions mentioned above, it is required that there be no stretch of the fluid in the y direction; in other words the scalar $F = H(X,\tau) - Y$ should be conserved throughout the computational domain:

$$\frac{\partial F}{\partial \tau} + U\frac{\partial F}{\partial X} + V\frac{\partial F}{\partial Y} = 0$$

$$\frac{\partial\left(\frac{H(X,\tau)-Y}{d}\right)d}{\partial\left(\tau/\tilde{\tau}\right)\tilde{\tau}} + \left(U/\breve{U}\right)\breve{U}\frac{\partial\left(\frac{H(X,\tau)-Y}{d}\right)d}{\partial\left(X/L\right)L} + \left(V/\breve{U}A\right)\breve{U}A\frac{\partial\left(\frac{H(X,\tau)-Y}{d}\right)d}{\partial\left(Y/d\right)d} = 0$$

$$\left(d/\tilde{\tau}\right)\frac{\partial h}{\partial t} + \left(\breve{U}A\right)u\frac{\partial h}{\partial x} + \left(\breve{U}A\right)v\left(\frac{\partial h}{\partial y} - 1\right) = 0$$

On the free surface (y=h $\rightarrow \frac{\partial h}{\partial y} = 0$) this condition:

$$u\frac{\partial h}{\partial x} + \left(L/\breve{U}\tau\right)\frac{\partial h}{\partial t} = v_{@\,y=h}$$

This equation can be further simplified by considering the Liebnitz theorem and the continuity equation:

Liebnitz theorem: $\frac{\partial}{\partial x}\int_0^{h(x)} \Phi dy = \int_0^{h(x)} \frac{\partial}{\partial x}(\Phi)dy + \Phi\frac{\partial h}{\partial x}$

$$\xrightarrow{\Phi \to u} \frac{\partial}{\partial x}\int_0^{h(x)} u dy = \int_0^{h(x)} \frac{\partial}{\partial x}(u) dy + u\frac{\partial h}{\partial x} \xrightarrow[\frac{\partial u}{\partial x}=-\frac{\partial v}{\partial y}]{continuity}$$

$$= \int_0^{h(x)} -\frac{\partial v}{\partial y} dy + u\frac{\partial h}{\partial x} \xrightarrow{\int_0^{h(x)} -\frac{\partial v}{\partial y} dy = v_{@\,y=h} - \cancel{v_{@\,y=0}}}$$

$$= -v_{@\,y=h} + u\frac{\partial h}{\partial x}$$

By substituting $v_{@y=h}$ the kinematic condition on the free surface is:

$$\frac{\partial}{\partial x}\int_0^{h} u dy + \left(L/U\tilde{\tau}\right)\frac{\partial h}{\partial t} = 0$$

This equation serves as the governing equation for the free surface profile. Naturally, u and h become coupled.

REFERENCES

[1] Marangoni, C., 1871, "Ueber Die Ausbreitung Der Tropfen Einer Flussigkeit Auf Der Oberflache Einer Anderen," Annalen der Physik., 219(7), pp. 337.

[2] Churchill, J., 1969, "Surface Tension in Fluid Mechanics."

[3] Ostrach, S., 1982, "Low-Gravity Fluid Flows," Annual Review of Fluid Mechanics, 14(1), pp. 313-345.

[4] Colinet, P., Legros, J. C., Velarde, M. G., and Prigogine, I., 2001, Nonlinear Dynamics of Surface-Tension-Driven Instabilities, Wiley-VCH.

[5] Young, N. O., Goldstein, J. S., and Block, M. J., 1959, "The Motion of Bubbles in a Vertical Temperature Gradient," Journal of Fluid Mechanics Digital Archive, 6(3), pp. 350-356.

[6] Birikh, R. V., Briskman, V. A., and Velarde, M. G., 2003, Liquid Interfacial Systems: Oscillations and Instability, CRC Press.

[7] Hadland, P. H., Balasubramaniam, R., Wozniak, G., and Subramanian, R. S., 1999, "Thermocapillary Migration of Bubbles and Drops at Moderate to Large Marangoni Number and Moderate Reynolds Number in Reduced Gravity," Experiments in Fluids, 26(3), pp. 240-248.

[8] Bratukhin, Y. K., and Zuev, A. L., 1984, "Thermocapillary Drift of an Air Bubble in a Horizontal Hele-Shaw Cell," Fluid Dynamics, 19(3), pp. 393-398.

[9] Bratukhin, Y. K., 1975, "Thermocapillary Drift of a Droplet of Viscous Liquid," Fluid Dynamics, 10(5), pp. 833-837.

[10] Brochard, F., 1989, "Motions of Droplets on Solid Surfaces Induced by Chemical or Thermal Gradients," Langmuir, 5(2), pp. 432-438.

[11] Brzoska, J. B., Brochard-Wyart, F., and Rondelez, F., 1993, "Motions of Droplets on Hydrophobic Model Surfaces Induced by Thermal Gradients," Langmuir, 9(8), pp. 2220-2224.

[12] Sammarco, T. S., and Burns, M. A., 1999, "Thermocapillary Pumping of Discrete Drops in Microfabricated Analysis Devices," AIChE Journal, 45(2), pp. 350-366.

[13] Darhuber, A. A., Valentino, J. P., Troian, S. M., and Wagner, S., 2003, "Thermocapillary Actuation of Droplets on Chemically Patterned Surfaces by Programmable Microheater Arrays," Journal of Microelectromechanical Systems, 12(6), pp. 873-879.

[14] Greco, E. F., and Grigoriev, R. O., 2009, "Thermocapillary Migration of Interfacial Droplets," Physics of Fluids, 21(4), pp. 042105.

[15] Grigoriev, R. O., 2005, "Chaotic Mixing in Thermocapillary-Driven Microdroplets," Physics of Fluids, 17(3), pp. 033601.

[16] Basu, A., and Gianchandani, Y. B., 2008, "Virtual Microfluidic Traps, Filters, Channels, and Pumps Using Marangoni Flows," Journal of Micromechanics and Microengineering, 18(11), pp. 115031(11pp).

[17] Yakhshi-Tafti, E., Cho, H. J., and Kumar, R., 2010, "Droplet Actuation on a Liquid Layer Due to Thermocapillary Motion: Shape Effect," Applied Physics Letters, 96(26), pp. 264101.

[18] Kim, J., 2007, "Spray Cooling Heat Transfer: The State of the Art," International Journal of Heat and Fluid Flow, 28(4), pp. 753-767.

[19] Lembach, A. N., Tan, H.-B., Roisman, I. V., Gambaryan-Roisman, T., Zhang, Y., Tropea, C., and Yarin, A. L., 2010, "Drop Impact, Spreading, Splashing, and Penetration into Electrospun Nanofiber Mats," Langmuir, 26(12), pp. 9516-9523.

[20] Van Dam, D. B., and Le Clerc, C., 2004, "Experimental Study of the Impact of an Ink-Jet Printed Droplet on a Solid Substrate," Physics of Fluids, 16(9), pp. 3403-3414.

[21] Moss, A. J., and Green, P., 1983, "Movement of Solids in Air and Water by Raindrop Impact. Effects of Drop-Size and Water-Depth Variations," Australian Journal of Soil Research, 21(3), pp. 257-269.

[22] Harlow, F. H., and Shannon, J. P., 1967, "Distortion of a Splashing Liquid Drop," Science, 157(3788), pp. 547-550.

[23] Hobbs, P. V., and Kezweeny, A. J., 1967, "Splashing of a Water Drop," Science, 155(3766), pp. 1112-1114.

[24] Macklin, W. C., and Hobbs, P. V., 1969, "Subsurface Phenomena and the Splashing of Drops on Shallow Liquids," Science, 166(3901), pp. 107-108.

[25] Xu, L., Zhang, W. W., and Nagel, S. R., 2005, "Drop Splashing on a Dry Smooth Surface," Physical Review Letters, 94(18), pp. 184505.

[26] Xu, L., Barcos, L., and Nagel, S. R., 2007, "Splashing of Liquids: Interplay of Surface Roughness with Surrounding Gas," Physical Review E, 76(6), pp. 066311.

[27] Rein, M., 1993, "Phenomena of Liquid Drop Impact on Solid and Liquid Surfaces," Fluid Dynamics Research, 12(2), pp. 61-93.

[28] Yarin, A. L., 2006, "Drop Impact Dynamics: Splashing, Spreading, Receding, Bouncingâ€¦," Annual Review of Fluid Mechanics, 38(1), pp. 159-192.

[29] Hobbs, P. V., and Osheroff, T., 1967, "Splashing of Drops on Shallow Liquids," Science, 158(3805), pp. 1184-1186.

[30] Cossali, G., Coghe, A., and Marengo, M., 1997, "The Impact of a Single Drop on a Wetted Solid Surface," Experiments in Fluids, 22(6), pp. 463-472.

[31] Rioboo, R., Bauthier, C., Conti, J., Voué, M., and De Coninck, J., 2003, "Experimental Investigation of Splash and Crown Formation During Single Drop Impact on Wetted Surfaces," Experiments in Fluids, 35(6), pp. 648-652.

[32] Wang, A.-B., and Chen, C.-C., 2000, "Splashing Impact of a Single Drop onto Very Thin Liquid Films," Physics of Fluids, 12(9), pp. 2155-2158.

[33] Thoroddsen, S. T., Etoh, T. G., and Takehara, K., 2003, "Air Entrapment under an Impacting Drop," Journal of Fluid Mechanics, 478(pp. 125-134.

[34] Khan, M. S., Kannangara, D., Shen, W., and Garnier, G., 2008, "Isothermal Noncoalescence of Liquid Droplets at the Airâˆ’Liquid Interface," Langmuir, 24(7), pp. 3199-3204.

[35] Gilet, T., Vandewalle, N., and Dorbolo, S., 2007, "Controlling the Partial Coalescence of a Droplet on a Vertically Vibrated Bath," Physical Review E, 76(3), pp. 035302.

[36] Couder, Y., Fort, E., Gautier, C. H., and Boudaoud, A., 2005, "From Bouncing to Floating: Noncoalescence of Drops on a Fluid Bath," Physical Review Letters, 94(17), pp. 177801.

[37] Richard, D., and Quere, D., 2000, "Bouncing Water Drops," Europhysics Letters, 50(6), pp. 769-755.

[38] Rioboo, R., Voue, M., Adao, H., Conti, J., Vaillant, A., Seveno, D., and De Coninck, J., 2010, "Drop Impact on Soft Surfaces: Beyond the Static Contact Angles," Langmuir, 26(7), pp. 4873-4879.

[39] Aussillous, P., and Quere, D., 2006, "Properties of Liquid Marbles," Proceedings of the Royal Society A: Mathematical, Physical and Engineering Science, 462(2067), pp. 973-999.

[40] Rapacchietta, A. V., Neumann, A. W., and Omenyi, S. N., 1977, "Force and Free-Energy Analyses of Small Particles at Fluid Interfaces : I. Cylinders," Journal of Colloid and Interface Science, 59(3), pp. 541-554.

[41] Rapacchietta, A. V., and Neumann, A. W., 1977, "Force and Free-Energy Analyses of Small Particles at Fluid Interfaces : Ii. Spheres," Journal of Colloid and Interface Science, 59(3), pp. 555-567.

[42] Huh, C., and Scriven, L. E., 1969, "Shapes of Axisymmetric Fluid Interfaces of Unbounded Extent," Journal of Colloid and Interface Science, 30(3), pp. 323-337.

[43] Neumann, A. W., and Good, R. J., 1972, "Thermodynamics of Contact Angles. I. Heterogeneous Solid Surfaces," Journal of Colloid and Interface Science, 38(2), pp. 341-358.

[44] Tropea, C., Yarin, A. L., and Foss, J. F., 2007, Handbook of Experimental Fluid Mechanics, Springer.

[45] Bashforth, F., and Adams, J. C., 1883, An Attempt to Test the Theories of Capillary Action: By Comparing the Theoretical and Measured Forms of Drops of Fluid. , University Press.

[46] Savino, R., Paterna, D., and Lappa, M., 2003, "Marangoni Flotation of Liquid Droplets," Journal of Fluid Mechanics, 479(1), pp. 307-326.

[47] Srinivasan, V., Pamula, V. K., and Fair, R. B., 2004, "Droplet-Based Microfluidic Lab-on-a-Chip for Glucose Detection," Analytica Chimica Acta, 507(1), pp. 145-150.

[48] Levich, V. G., 1962, Physicochemical Hydrodynamics, Prentice-Hall Inc.

[49] Levich, V. G., and Krylov, V. S., 1969, "Surface-Tension-Driven Phenomena," Annual Review of Fluid Mechanics, 1(1), pp. 293-316.

[50] Probstein, R. F., 1994, Physicochemical Hydrodynamics, John Wiley.

[51] Yih, C.-S., 1968, "Fluid Motion Induced by Surface Tension Variation," Physics of Fluids, 11(3), pp. 477-480.

[52] Pimputkar, S. M., and Ostrach, S., 1980, "Transient Thermocapillary Flow in Thin Liquid Layers," Physics of Fluids, 23(7), pp. 1281-1285.

[53] Sen, A. K., and Davis, S. H., 1982, "Steady Thermocapillary Flows in Two-Dimensional Slots," Journal of Fluid Mechanics Digital Archive, 121(1), pp. 163-186.

[54] Yih, C.-S., 1967, "Instability of Laminar Flows Due to a Film of Adsorption," Journal of Fluid Mechanics, 28(3), pp. 493-500.

[55] Savino, R., and Monti, R., 1997, "Modelling of Non-Coalescing Liquid Drops in the Presence of Thermocapillary Convection," Meccanica, 32(2), pp. 115-133.

[56] Yakhshi-Tafti, E., Cho, H. J., and Kumar, R., 2010, "Impact of Drops on the Surface of Immiscible Liquids," Journal of Colloid and Interface Science, 350(1), pp. 373-376.

[57] Sreenivas, K. R., and De, P. K., 1999, "Levitation of a Drop over a Film Flow," Journal of Fluid Mechanics, 380(pp. 297-307.

[58] Panton, R. L., 1995, Incompressible Flow, John Wiley and Sons, Inc.

[59] Harper, J. F., Moore, D. W., and Pearson, J. R. A., 1967, "The Effect of the Variation of Surface Tension with Temperature on the Motion of Bubbles and Drops," Journal of Fluid Mechanics, 27(2), pp. 361-366.

[60] Chaudhury, M. K., and Whitesides, G. M., 1992, "How to Make Water Run Uphill," Science, 256(5063), pp. 1539(3pp).

[61] Lehmann, U., Vandevyver, C., Parashar, V. K., and Gijs, M. A. M., 2006, "Droplet-Based DNA Purification in a Magnetic Lab-on-a-Chip," Angewandte Chemie International Edition, 45(19), pp. 3062-3067.

[62] Diguet, A., Guillermic, R. M., Magome, N., Saint-Jalmes, A., Chen, Y., Yoshikawa, K., and Baigl, D., 2009, "Photomanipulation of a Droplet by the Chromocapillary Effect," Angewandte Chemie International Edition, 48(49), pp. 9281-9284.

[63] Pollack, M. G., Fair, R. B., and Shenderov, A. D., 2000, "Electrowetting-Based Actuation of Liquid Droplets for Microfluidic Applications," Applied Physics Letters, 77(11), pp. 1725-1726.

[64] Spiess, B. D., 2009, "Perfluorocarbon Emulsions as a Promising Technology: A Review of Tissue and Vascular Gas Dynamics," J Appl Physiol, 106(4), pp. 1444-1452.

[65] Spiess, B. D., Mccarthy, R., Piotrowski, D., and Ivankovich, A. D., 1986, "Protection from Venous Air Embolism with Fluorocarbon Emulsion Fc-43," Journal of Surgical Research, 41(4), pp. 439-444.

[66] Vorob'ev, S., 2009, "First- and Second-Generation Perfluorocarbon Emulsions," Pharmaceutical Chemistry Journal, 43(4), pp. 209-218.

[67] Pollack, M. G., Shenderov, A. D., and Fair, R. B., 2002, "Electrowetting-Based Actuation of Droplets for Integrated Microfluidics," Lab Chip, 2(96), pp. 101.